

La borsa di dottorato è stata cofinanziata con risorse del
Programma Operativo Nazionale Ricerca e Innovazione 2014-202 (CCI 2014IT16M2OP005)
Fondo Sociale Europeo, Azione I.1 “Dottorati Innovativi con caratterizzazione Industriale”



UNIONE EUROPEA
Fondo Sociale Europeo



UNIVERSITA' DELLA CALABRIA

Dipartimento di Fisica

Dottorato di Ricerca in Scienze e Tecnologie Fisiche, Chimiche e dei Materiali

Con il contributo di MIUR -PON 2014 2020

CICLO XXXIII

Materials and processes for the optical Additive Manufacturing of advanced organic/inorganic nanocomposites for the mask-less plating of insulator and semiconductor substrates, and microfluidic devices

Settore Scientifico Disciplinare FIS/03 FISICA DELLA MATERIA

Coordinatore: Ch.ma Prof. Gabriella Cipparrone


Firma oscurata in base alle linee
guida del Garante della privacy

Supervisore/Tutor: Ch.mo Prof. Michele Giocondo

Supervisore/Tutor: Ch.mo Prof. Antonio De Luca

Supervisore/Tutor: Ch.mo Prof. Alberto Sanz de León

Dottorando: Dott./ssa Wera Di Cianni

La borsa di dottorato è stata cofinanziata con risorse del
Programma Operativo Nazionale Ricerca e Innovazione 2014-202 (CCI 2014IT16M2OP005)
Fondo Sociale Europeo, Azione I.1 “Dottorati Innovativi con caratterizzazione Industriale”



UNIONE EUROPEA
Fondo Sociale Europeo



UNIVERSITA' DELLA CALABRIA

Dipartimento di Fisica

Dottorato di Ricerca in Scienze e Tecnologie Fisiche, Chimiche e dei Materiali

Con il contributo di MIUR -PON 2014 2020

CICLO XXXIII

Materials and processes for the optical Additive Manufacturing of advanced organic/inorganic nanocomposites for the mask-less plating of insulator and semiconductor substrates, and microfluidic devices

Settore Scientifico Disciplinare FIS/03 FISICA DELLA MATERIA

Coordinatore: Ch.ma Prof. Gabriella Cipparrone

Firma _____

Supervisore/Tutor: Ch.mo Prof. Michele Giocondo

Firma U Firma oscurata in base alle linee guida del Garante della privacy

Supervisore/Tutor: Ch.mo Prof. Antonio De Luca

Firma _____ Firma oscurata in base alle linee guida del Garante della privacy

Supervisore/Tutor: Ch.mo Prof. Alberto Sanz de León

Firma _____ Firma oscurata in base alle linee guida del Garante della privacy

Dottorando: Dott./ssa Wera Di Cianni

Firma _____ Firma oscurata in base alle linee guida del Garante della privacy

La borsa di dottorato è stata cofinanziata con risorse del
Programma Operativo Nazionale Ricerca e Innovazione 2014-202 (CCI 2014IT16M2OP005)
Fondo Sociale Europeo, Azione I.1 “Dottorati Innovativi con caratterizzazione Industriale”



UNIONE EUROPEA
Fondo Sociale Europeo



UNIVERSITA' DELLA CALABRIA

Dipartimento di Fisica

Dottorato di Ricerca in Scienze e Tecnologie Fisiche, Chimiche e dei Materiali

Con il contributo di MIUR -PON 2014 2020

CICLO XXXIII

Materials and processes for the optical Additive Manufacturing of advanced organic/inorganic nanocomposites for the mask-less plating of insulator and semiconductor substrates, and microfluidic devices

Settore Scientifico Disciplinare FIS/03 FISICA DELLA MATERIA

Coordinatore: Ch.ma Prof. Gabriella Cipparrone

Supervisore/Tutor: Ch.mo Prof. Michele Giocondo

Supervisore/Tutor: Ch.mo Prof. Antonio De Luca

Supervisore/Tutor: Ch.mo Prof. Alberto Sanz de León

Dottorando: Dott./ssa Wera Di Cianni

Acknowledgements

A special thanks to my professors who have been a scientific and moral guide in this journey, to my nearest and dearest family and friends to be a real support always and everywhere; to my university for this special experience

Index

Index.....	i
Acronym list.....	iii
1. Abstract.....	1
1. Abstract (Spanish)	3
1. Abstract (Italian)	5
2. Introduction	7
2.1. Nanotechnology and Nanofabrication (NF).....	8
2.2. Nanofabrication techniques.....	10
2.3. AM and nanotechnology.....	15
2.4. Laser-assisted AM techniques: SL and TP-DLW	22
2.4.1. Stereolithography (SL)	22
2.4.2. Direct Laser Writing and TPP.....	24
2.4.3. Theory behind SL and TP-DLW.....	26
2.4.4. Advantages and disadvantages of the techniques	30
2.5. New materials for NF with AM: nanocomposites and non-polymeric nanostructures...31	
3. Aim of the thesis.....	34
4. Materials and Methods.....	36
4.1. Materials.....	36
4.1.1. Materials for gold nanocomposites via SL.....	36
4.1.2. Materials for gold nanostructures via TP-DLW.....	36
4.1.3. Materials for fiber reinforced polymer nanocomposites (FRPN) via TP-DLW.....	37
4.2. Additive Manufacturing technologies.....	37
4.2.2. Fabrication via TP-DLW.....	41
4.2.3. Fabrication via TP-DLW on SiO ₂ NWs substrate.....	45
4.3. Characterization	48
5. Additive Manufacturing of AuNPs composites via SL	52
5.1. Preliminary tests.....	52
5.1.1. Study of the range of KAuCl ₄ concentrations valid for SL.....	53
5.1.2. Influence of UV and thermal treatments in the formation of AuNPs.....	58
5.2. SL Printing of 3D objects	67
5.2.1. Influence of the UV and thermal treatment in 3D printed monolayers.....	68
5.2.2. Influence of the concentration of gold precursor.....	71
5.2.3. Influence of the size of the printed object.....	74
5.2.4. Stability of the nanocomposites. Influence of time and aging	81
6. TP-DLW of metallic structures on opaque substrates.....	83
6.1. Preliminary tests: TP-DLW with commercial photoresists (TPP).....	83
6.2. TP-DLW with PVA and gold precursor on a transparent substrate	86
6.3. TP-DLW with PVA and gold precursor on an opaque substrate	87
6.4. TP-DLW with isinglass and gold precursor on an opaque substrate.....	91
6.4.1. Seeding and Growth	92
6.4.2. Analysis of the morphology of AuNPs.....	98
6.4.3. AuNPs growth kinetics: estimation of the amount of Au.....	102

6.4.4. Study of the range of HAuCl_4 concentrations valid for TP-DLW.....	104
6.4.5. Study of the range of times for the growth process.....	107
6.4.6. IP-S and HAuCl_4	110
7. Additive Manufacturing of SiO_2 NWs nanocomposites via TP- DLW	113
7.1. Fabrication of FRPN via TP-DLW on SiO_2 NWs substrate	114
7.1.1. HF etching of FRPN.....	117
7.1.2. Only-shell layer.....	119
7.2. Mechanical characterization of the FRPN.....	121
7.3. SiO_2 NWs and HAuCl_4	123
8. Conclusions and future work	125
9. Bibliography.....	128
9.1. Introduction.....	128
9.2. Additive Manufacturing of AuNPs composites via SL.....	134
9.3. TP-DLW of metallic structures on opaque substrates	135
9.4. Additive Manufacturing of SiO_2 NWs nanocomposites via TP-DLW.....	137
Figures.....	138
Tables	149

Acronym list

1D	One-Dimensional
2D	Bi-Dimensional
3D	Three-Dimensional
AFM	Atomic Force Microscope
BSEs	Back-Scattering Electrons
BU	Bottom-up
CAD	Computer-Aided design
DLW	Direct Laser Writing
AuNPs	Gold Nanoparticles
EDX	Energy Dispersive X-Ray
HAADF	High-angle annular dark-field imaging
IPA	Isopropyl Alcohol
LP	Laser Power
NIR	Near Infra-Red
NF	Nanofabrication
NPs	Nanoparticles
PVA	Polyvinyl Alcohol
SEM	Scanning Electron Microscopy
SPA	Single Photon Absorption
SS	Scan Speed
SL	Stereolithography
TD	Top Down
TEM	Transmission Electron Microscopy
TP-DLW	Two-Photon Direct Laser Writing
TPA	Two-Photon Absorption
TPP	Two-Photon Polymerization
UV	Ultra-Violet
voxel	Volume pixel

1. Abstract

The research presented in this doctoral thesis is carried out in the nanotechnology and soft matter frameworks, under the 4.0 Industry paradigm, inspired by the need to find new strategies for the Additive Manufacturing (AM) and to obtain new processable nanocomposites with enhanced properties.

The AM technologies allow to build 3D objects with complex geometries by adding layer-upon-layer of material without any mold and permits to fabricate structured objects and microfluidic systems with particular optical and mechanical properties which cannot be easily made with classical Subtractive Manufacturing (SM) techniques. This paves the way to large improvements in optoelectronics, biotechnology, diagnostic or medicine. Moreover, the combined employment of bottom-up and top-down fabrication approaches could lead to important advances in the field of nanotechnology, widening further the possible applications field, permitting high resolution repeatable nanofabrication of 3D complex objects with the possibility of immediate industrial applications.

The first AM technique used in this work is Stereolithography (SL), a vat photopolymerization technique that uses UV light to produce objects with resolution in the range 10-100 μm . Here, the novelty consists in adding a metallic precursor (KAuCl_4) to a typical photosensitive resin to produce nanocomposites with gold nanoparticles synthesized *in situ* via photo- and thermal reduction. Nanocomposites produced are rich in gold nanoparticles and have interesting optical and plasmonic properties. Moreover, a fine tuning of the concentration of the gold salt allows the resin polymerization without suffering any inhibition of the gold precursor.

A similar approach, taking advantage of the combination with photoreduction of a gold precursor (HAuCl_4), can be achieved using a different technique belonging to the vat photopolymerization category, namely the Two Photon Direct Laser Writing (TP-DLW). This technique exploits the optical, nonlinear multiphoton absorption process and allows for the fabrication of 3D objects

featuring details below the diffraction limit, down to 100 nm or even less. Here, this multiphoton absorption process is exploited to trigger the photo-reduction of the gold precursor. The use of a transparent hydrogel matrix allows for a fine control of the nanoparticles' growth on either transparent or opaque substrates, such as glass or silicon, without the need of using masks or molds. An in-depth study on the diffusive process underlying the nanoparticles growth and a control of the ionic concentration are done to prove the importance of having a polymeric network to hold the created nanoparticles at their place, which enhances the quality of the created nanostructures.

The nanofabrication of fiber reinforced polymer nanocomposites by TP-DLW was also demonstrated. For these experiments, the classical glass or silicon substrates were replaced with a silicon substrate on which silica nanowires (SiO_2 NWs) have been previously grown. This research allowed to achieve the best resolution offered by the TP-DLW technique, even with high loads of fillers of SiO_2 NWs, up to 70 wt%. This was achieved by matching the refractive indices of the SiO_2 NWs and of the photoresist used as polymeric matrix. These nanocomposite materials presented a noticeable improvement of nano-hardness and elastic modulus when compared to the pristine photoresist, indicating how the proposed technique is well-suited for nano-applications with higher structural requirements, as in advanced microfluidics.

A final comparison of the AM technologies used in the thesis is done to elucidate the advantages and disadvantages of each one of these techniques to choose the most efficient, easiest and fastest, depending on the materials to be used or the required resolution.

1. Abstract (Spanish)

La investigación presentada en esta tesis doctoral se lleva a cabo en el marco de la nanotecnología y los materiales poliméricos, bajo el paradigma de la Industria 4.0, inspirada por la necesidad de buscar nuevas estrategias para la fabricación aditiva (FA) y obtener nuevos materiales nanocompuestos con propiedades mejoradas.

Las tecnologías de FA permiten fabricar objetos en 3D con geometrías complejas añadiendo material capa a capa sin el uso de un molde y permite fabricar objetos estructurados y sistemas de microfluidos con propiedades ópticas y mecánicas que no pueden fabricarse fácilmente mediante técnicas clásicas de fabricación subtractiva. Esto allana el camino hacia grandes mejoras en optoelectrónica, biotecnología y técnicas de diagnóstico y medicina. Además, el uso combinado de las técnicas de fabricación *bottom-up* y *top-down* podrían llevar a importantes avances en el campo de la nanotecnología, ampliando los campos de aplicación, permitiendo la fabricación de complejos objetos 3D, reproducibles con alta resolución y con la posibilidad de aplicación industrial directa.

La primera técnica de FA usada en este trabajo es la estereolitografía (SL), una técnica de fotopolimerización en tanque que utiliza luz ultravioleta para producir objetos con una resolución de 10-100 μm . En este caso, la novedad consiste en añadir un precursor metálico (KAuCl_4) a una resina fotosensible estándar para producir materiales nanocompuestos con nanopartículas de oro sintetizadas *in situ* mediante foto- y reducción térmica. Los materiales producidos son ricos en nanopartículas de oro y tienen interesantes propiedades ópticas y plasmónicas. Además, un ajuste fino de la concentración de la sal de oro permite la polimerización de la resina sin sufrir ninguna inhibición por parte del precursor de oro.

Una aproximación similar, aprovechando la combinación de la fotorreducción de un precursor de oro (HAuCl_4), puede lograrse usando una técnica diferente que también pertenece a la categoría de fotopolimerización en tanque, en particular la escritura directa con láser mediante dos fotones (TP-DLW). Esta técnica se vale de procesos ópticos no lineales de absorción de fotones y permite la

fabricación de objetos 3D con detalles por debajo del límite de difracción, hasta 100 nm o incluso menos. En este caso, este proceso de absorción de multifotones se explota para activar la fotorreducción de un precursor de oro. El uso de un hidrogel transparente como matriz permite el control fino del crecimiento de las nanopartículas en sustratos tanto transparentes como opacos, como vidrio o silicio, sin necesidad de usar máscaras o moldes. Se ha hecho un estudio en profundidad de los procesos de difusión que subyacen detrás del crecimiento de las nanopartículas y un control de la concentración iónica para demostrar la importancia de tener una red polimérica que retenga las nanopartículas creadas, mejorando la calidad de las nanoestructuras creadas.

La nanofabricación de materiales nanocompuestos poliméricos reforzados con fibra mediante TP-DLW también se ha demostrado. Para estos experimentos, los sustratos clásicos de vidrio o silicio se reemplazaron con un sustrato de silicio con nanohilos de sílice (SiO_2 NWs). Esta investigación permitió alcanzar la máxima resolución posible en TP-DLW, incluso con altos contenidos de SiO_2 NWs, de hasta el 70 % en peso. Esto se logró utilizando unos nanohilos de sílice y una resina fotosensible con prácticamente el mismo índice de refracción. Estos materiales presentaron una mejora significativa en nano-dureza y módulo elástico cuando se compararon con la resina fotosensible sin modificar, indicando que esta técnica propuesta es válida para nano-aplicaciones con mayores requisitos mecánicos, como en microfluídica avanzada.

Finalmente, en esta tesis se hace una comparación de estas tecnologías de FA para elucidar las ventajas e inconvenientes de cada una de estas técnicas para elegir la más eficiente, simple y rápida en función de los materiales usados y la resolución requerida.

1. Abstract (Italian)

Il lavoro di ricerca presentato in questa tesi di dottorato è stato svolto nell'ambito delle nanotecnologie e della *Soft Matter*, in linea con le indicazioni fondamentali del Piano Nazionale di Industria 4.0, ispirato dall'esigenza di trovare nuove strategie per l'Additive Manufacturing (AM) e finalizzato ad ottenere nuovi nanocompositi processabili con proprietà potenziate rispetto alla controparte macroscopica.

Le tecnologie AM permettono di costruire oggetti 3D con geometrie complesse aggiungendo materiale strato su strato senza la necessità di utilizzare alcuno stampo o maschera e oggetti strutturati e sistemi microfluidici con particolari proprietà ottiche e meccaniche che non possono essere facilmente realizzate con le classiche tecniche di Subtractive Manufacturing (SM). Questo apre la strada a numerosi miglioramenti in optoelettronica, biotecnologie, diagnostica, medicina.

Inoltre, l'impiego combinato dei metodi di fabbricazione *bottom-up* e *top-down* potrebbe portare ad importanti progressi nell'ambito delle nanotecnologie ampliando di molto il campo di possibili applicazioni permettendo un'alta risoluzione e riproducibilità nella nano-fabbricazione di complessi oggetti 3D, con la possibilità di immediate applicazioni industriali.

La prima tecnica AM usata in questo studio è la Stereolitografia (SL), una tecnica di fotopolimerizzazione 'in vasca' che usa luce UV per produrre oggetti con una risoluzione nel range di 10-100 μm . In questo caso, la novità consiste nell'aggiungere un precursore metallico (KAuCl_4) ad una resina fotosensibile tradizionale per produrre nanocompositi con nanoparticelle d'oro sintetizzate *in situ* attraverso fotoriduzione e riduzione termica. I nanocompositi prodotti sono ricchi di nanoparticelle d'oro (AuNPs) e hanno interessanti proprietà ottiche e plasmoniche. Inoltre un'ottimizzazione nel controllo della concentrazione dei sali d'oro permette la polimerizzazione della resina senza che il precursore determini alcuna inibizione.

Un tale approccio sfrutta la combinazione della fotoriduzione di un precursore d'oro, e può essere realizzato usando una tecnica differente che appartiene alla categoria della fotopolimerizzazione

‘in vasca’, chiamata Direct Laser Writing (DLW). Questa tecnica sfruttando il processo ottico di assorbimento non lineare a più fotoni, permette la costruzione di oggetti 3D con dettagli al di sotto del limite di diffrazione fino a 100 nm o anche minore. I processi di assorbimento multifotone sono sfruttati per attivare la fotoriduzione del precursore d'oro. L'uso di una matrice idrogel trasparente permette un fine controllo della crescita delle NPs su substrati sia opachi che trasparenti, come vetro o silicio senza bisogno di usare maschere o stampi. È stato inoltre approfondito lo studio dei processi diffusivi alla base della crescita delle nanoparticelle d'oro create grazie al quale è stato possibile realizzare un migliore controllo della concentrazione degli ioni, dimostrando così l'importanza di un network polimerico che mantenga le nanoparticelle fisse nelle loro posizioni e che migliori in questo modo la qualità delle strutture create.

Si è dimostrato poi che è possibile realizzare nanocompositi polimerici rinforzati con fibre mediante Direct Laser Writing. Per questi esperimenti il classico vetro o i substrati di silicio sono stati sostituiti da un substrato di silicio su cui nanowires di silicio sono precedentemente cresciuti.

Questo studio permette di raggiungere la migliore risoluzione offerta dalla tecnica DLW anche nel caso dell'utilizzo di filler come per esempio i nanowires di silica (SiO_2 NWs) usati nel nostro caso fino al 70 wt%. Ciò è stato possibile mediante il matching tra gli indici di rifrazione dei SiO_2 NWs e della resina fotosensibile usata come matrice polimerica. Tali materiali nanocompositi presentano un notevole miglioramento delle proprietà di durezza e modulo elastico rispetto alla resina fotosensibile pura, dimostrando che il protocollo individuato risulta molto valido per nano-applicazioni complesse come in microfluidica avanzata.

Infine, un confronto tra le tecnologie AM usate in questa tesi ha illustrato i vantaggi e gli svantaggi di ognuna di esse, permettendo di scegliere ogni volta la più indicata ai fini della rapidità, della facilità di applicazione, dell'efficienza, in funzione dei materiali che si desidera impiegare e della risoluzione che si vuole raggiungere.

2. Introduction

The research falls into the domain of Soft Matter Science and was inspired by a real and general problem related to the chance to explore and find new strategies for Additive Manufacturing and then to implement these methods to an industry level too.

Among all the different technologies, optical lithography is one of the most used and investigated, thanks to the possibility of using light as a tool to micro-structure a photosensitive material^[1,2].

Due to their flexibility and the possibility to be employed in a wide range of applications, polymers are widely used in micro-fabrication processes^[3,4].

The combination of powerful elements like promising techniques as stereolithography or two-photon polymerization together with photosensitive resins and metal precursors could lead to an improving understanding of the physical and chemical processes behind the fabrication. This permits to figure out the best way to use them in conjunction and a progress in technical applications with the view to producing high-performance nanocomposite prototypes as smart platforms rich in gold nanoparticles (AuNPs) or 3D fiber reinforced objects suitable to different employments^[5].

During the fabrication process, especially while treating with polymeric materials, despite the advanced technology employed, can occur some issues that can be particularly damaging during the TP-DLW implementation of objects and devices with “large” size and “small” details, for example the swelling of the polymer in aggressive environment and the easy distortion of details. The larger the size/scale ratio of the object we want to realize, the more evident and harmful the problem. AM fabrication of objects that involve different scales of length in particular in the range 10^{-3} - 10^{-8} m does not allow an effective use of this technology in productivity contexts. The development of materials and processes to overcome limitations in production can make possible the extension of SL and TP-DLW technologies to industrial processes and applications today difficult to implement.

2.1. Nanotechnology and Nanofabrication (NF)

The research activity here presented is carried out in the nanotechnology and soft matter frameworks, inspired by the need to find new strategies for the AM processes and to obtain new nanocomposites with enhanced properties.

Nanotechnology caught the attention of the research investments already since the second half of the 90s of XXI century and the possible applications of nanostructured materials have become almost unlimited, because of the wide range of the sectors involved, including medicine, aerospace, electronics, textile industry and energy^[6-9].

The forerunner in this field was Richard Feynman who, in his conference in 1959 “*There is plenty of room at the bottom*” argued that manipulating matter at an atomic level could bring to control the properties of the materials.

In fact, already at the sub-micrometric scale, the size and the spatial configuration of produced single features start to influence the characteristics of the whole object, enabling for an array of new, exotic and otherwise unachievable properties and structures in the new composites^[10,11]. Nanostructured materials of this sort become strong candidates to employ in micro/nanofabrication, in order to fabricate sub-micrometric scale high complexity tridimensional objects. Modifying the nanostructure or adding nanocomponents it is possible to improve the mechanical, thermal, optical, electronic or magnetic properties of the objects. Design and development of potential prototypes employable in various devices pave the way to the utilization of these kind of techniques and strategies even to an industrial level.

Depending on the applications, metallic or semiconductor nanoparticles are employed. In the last decades, the attention is focused especially on the fabrication of metal-containing nanomaterials. In particular, Au-based nanomaterials are of great interest because of their numerous applications in photonics^[12-14], with a particular reference to innovative sensing platforms. Other applications are in the field of biomedicine, overcoming even the biocompatibility of the early years taking advantage

of biomimetic coatings^[15]; in electronics and optics^[16] and also in the industrial production where it is registering a significant demand for Au-containing nanomaterials ^[17,18] (**Figure 2.1**).

Fabrication of metallic nanostructures within a dielectric host material allows the optical response of the composite material to be tailored, potentially achieving responses not possible in a homogeneous material^[19,20]. This capability is most notably exploited in the rapidly advancing field of optical metamaterials, a new class of nanostructured materials that exhibit exotic electromagnetic properties, such as a negative refractive index, that are not observed in naturally occurring materials^[21–24].

Functionally to these aspects, attention is focused on the research of the most performing and efficient materials, on the study of the physical processes behind and on the techniques that can be used to produce the required objects^[11,25,26].

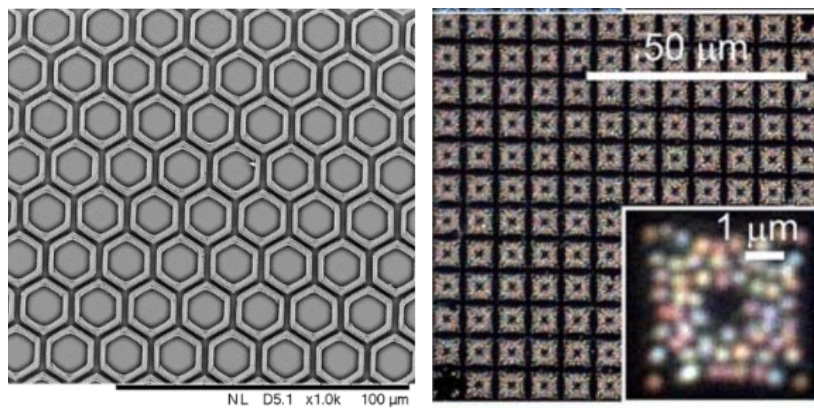


Figure 2.1 *Examples of applications of the fabrication of metal-containing nanomaterials: a TMPTA-Au nano-composite periodic structure for metamaterials^[27]; a flexible photonic device based on dielectric antennas made with SiGe islands embedded in a PDMS slice^[28].*

2.2. Nanofabrication techniques

Classical nanotechnology techniques applied to produce functional structures can follow two different approaches: on one hand, the top-down (TD) techniques use externally-controlled devices to direct the fabrication of the nanostructures. These techniques utilize traditional methods where different tools are used to shape the materials to obtain a particular geometry. Examples of these technologies include lithographic patterning and micro-contact printing.

On the other hand, the bottom-up (BU) approach relies on the self-assembly of molecules under certain external conditions to create micro/nanostructures that cannot be made otherwise.

An example from everyday life, we can say TD approaches would look like a sculptor who carves a marble block using his chisel, down to the desired size and shape. On the contrary, BU techniques deal with the assembling of single building-blocks, at a molecular or supramolecular assemblies level, which “spontaneously” create a nano-system, as a bricklayer would do to build a wall brick by brick (**Figure 2.2**).



Figure 2.2 *Top down (TD) and Bottom Up (BU) approaches for Additive Manufacturing.*

TD approaches are especially suitable for producing structures with long-range order and for making macroscopic connections, and are traditionally employed in microelectronics and integrated electric circuits at the microscale. TD methods are usually based on manifold lithographic techniques, as electron beam or soft lithography, using electromagnetic radiation ranging from UV to X-rays.

Among these techniques, photolithography is the most widespread, especially in the electronics sector. Different photosensitive resins can be found in positive and negative tone [29]. A hole in the mask creates a hole in a positive tone photoresist, whereas it will create a pit in a negative tone photoresist^[1,6,30–32]. This permits to create 1D, 2D and even 2.5D structures in the photo-sensitive resin, with a resolution down to few micrometers, limited by the optical diffraction. After the exposed resin is polymerized, the remaining non-exposed material is removed bathing the sample in a solvent. As a result, it is obtained a strongly adhering layer of controlled thickness, structured in islands reproducing the shape of the uncovered areas in the mask.

Micro-contact printing (not to be confused with 3D printing) is another one of the key lithographic techniques, in which an ink solution is transferred from an elastomeric mold, or stamp, to a substrate surface^[33] (**Figure 2.3**). The stamp is produced using soft lithography approaches and the ink solution is typically composed of proteins, protein mixtures or small molecules. After pouring the stamping solution onto the stamp, the transfer occurs at the interface of the stamp and the target substrate. The main limitation consists in the loss of pattern resolution due to ink spreading but the employment of new stamp materials and composite stamp designs with polar inks allow to overcome some problems.

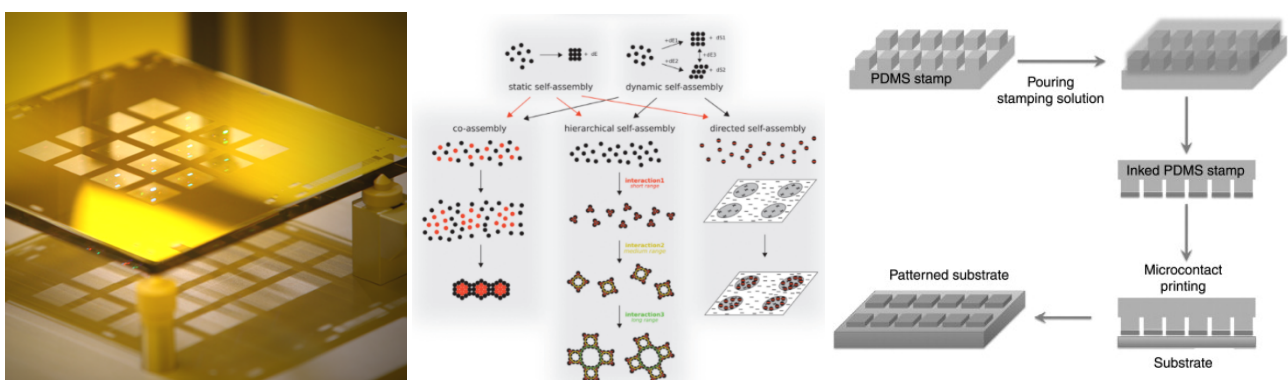


Figure 2.3 *Binary photomasks employed for photolithography: light passes through the mask and polymerizes with negative or positive tone; self-assembly technique for nanofabrication for static and dynamic cases and their connection with co-assembly, hierarchical and directed self-assembly (Ozin, 2009); microcontact printing with elastomeric (poly-dimethyl-siloxane, PDMS) stamps; after inking the stamp with the material solution, the deposition occurs by direct contact of the stamp with the surface of the substrate (Fernandes, 2013^[34]).*

Alternatively, BU approaches are recommended for establishing short-range assemblies at nanoscale dimensions. BU techniques are mainly investigated and used for creating arbitrarily complex objects according to the requirements which cannot be made by (most of) the TD techniques. BU fabrication techniques allow to carry out the synthesis of nanostructured-materials in the form of films, dust, crystals or super-molecules through chemical reactions, molecular assembly of nano-blocks such as copolymers or through processes of physical or chemical deposition of molecules and atoms. Alongside the traditional chemical synthesis methods, there are the techniques based on the physical/chemical vapor deposition (PVD, CVD) (**Figure 2.4**), on the atomic manipulation, using instruments as the atomic force microscope (AFM) or the scanning tunnel microscope (STM) with which perform the placement of even single atoms, with subatomic resolution (**Figure 2.5**); or on the sol-gel preparation, used for nano-catalysis, in the wet chemistry field^[29,35,36]. (**Figure 2.6**).

In detail, self-assembly processes imply a disordered system with preexisting components forms an organized structure or pattern as a consequence of specific, local interactions among its components without any external direction. Such a mechanism relies on weak, non-covalent bonds, such as hydrogen and ionic bonds, or Van der Waals forces and hydrophobic interactions, and it can be applied to fabricate various complex micro-and nanostructures, such as flowers, tubes, rods, micelles, films, membranes, meso-phases, particles, and hollow sphere structures^[30,37]. The main limitation is the less spatial control of the structures created and the need to have a flat substrate.

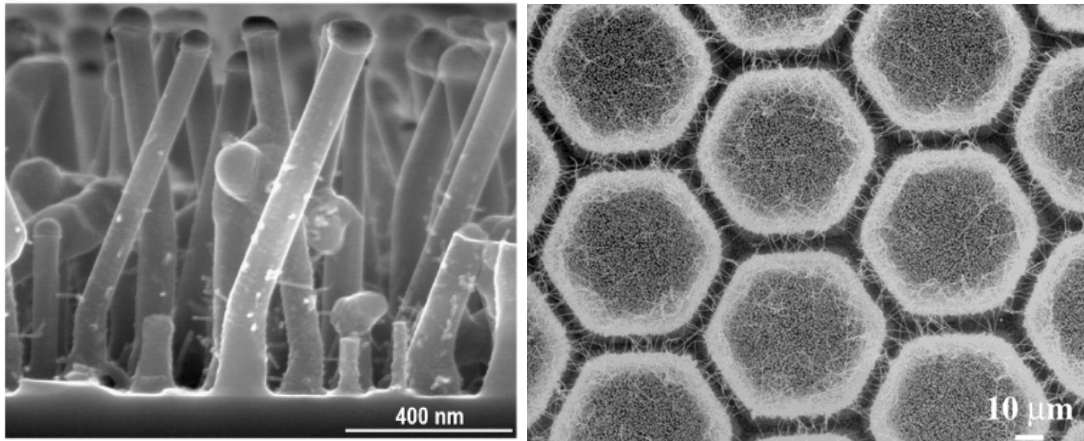


Figure 2.4 Silica nanowires grown on a Si(111) substrate, synthesized by UHV-CVD (ultra-high vacuum chemical vapor deposition) with a silane pressure of 6.67 Pa (Boukhicha, 2012); VLS growth of ZnO nanowire networks from the patterned Au islands (Huang, 2001)^[38,39]

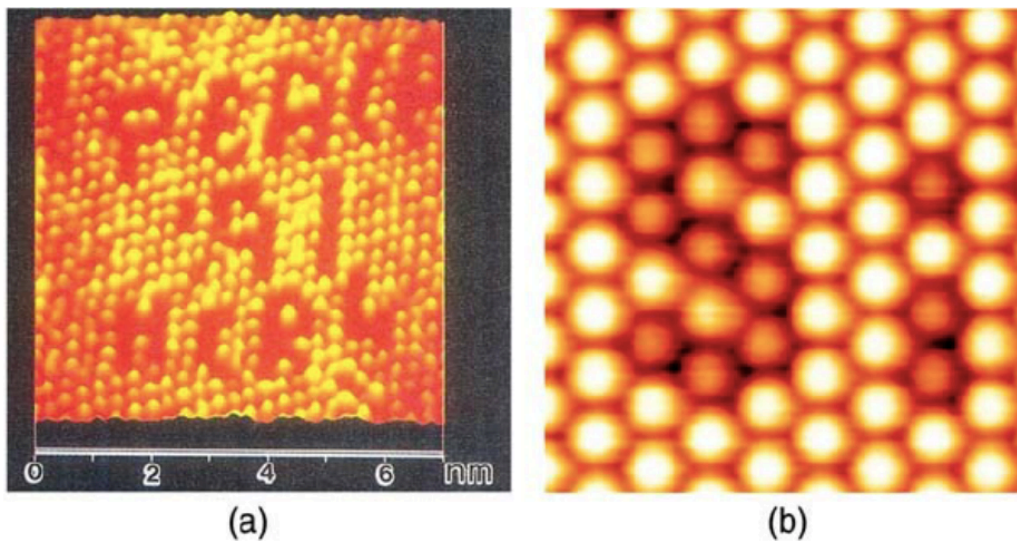


Figure 2.5 Atom-based letters created by vertical atom manipulation using STM and AFM. (a) Result of surface modification by STM, which reads 'PEACE 91 HCRL' (Hosoki S, Hosaka S, and Hasegawa T (1992) Surface modification of MoS₂ using an STM. *Appl. Surf. Sci.* 60-61: 643–647) and (b) complex atomic patterning by Si atoms embedded on an Sn/Si surface using AFM vertical atom-interchange manipulation (Sugimoto Y, Pou P, Custance O, Jelinek P, Abe M, Pérez R, and Morita S (2008) Complex patterning by vertical interchange atom manipulation using atomic force microscopy. *Science* 322:413–417) (Morita, 2011)^[40,41]

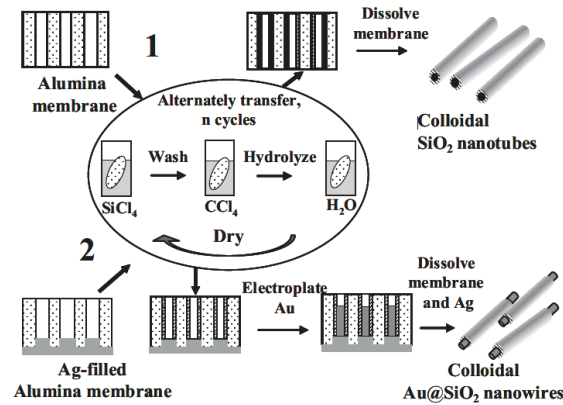


Figure 2.6 Scheme showing the surface sol-gel (SSG) synthesis of SiO_2 nanotubes (route 1) and SiO_2 coated nanowires (route 2) (Kovtyukhova, 2003)^[42]

Let us now compare the Subtractive Manufacturing (SM) and Additive Manufacturing (AM) processing technologies. In essence, all manufacturing techniques are labeled either as subtractive or additive. In SM, the material is removed from the initial slab or block, revealing the structure.

The advantage of such manufacturing strategy is that it can be relatively simple and well suited for mass production out of virtually any material.

The main limiting factor is its inability to create true 3D structures with an intricate internal geometry. Also, the material removed during fabrication is a technological waste that have to be somehow removed from the manufacturing setup and either disposed or recycled, contributing to the overall cost of the product. Currently, the most advanced kinds of subtractive fabrication are mechanical machining, laser cutting and selective laser etching^[11,26].

Alternatively, AM groups all the different techniques that allow the fabrication of objects in a layer-by-layer fashion without external molds or masks, obtaining structures with high reproducibility starting from a Computer Assisted Design (CAD). Contrarily to the SM technologies, all the AM techniques have in common that the desired object is created by adding the material to the structure until it is finished without elimination of unused material. The main advantages of the AM techniques include more freedom in the internal geometry of the structure/pattern and substantially less waste, direct translation of the design to the component, flexible lightweight of component manufacturing

with hollow or lattice structures and excellent scalability^[43]. Surely some limitations for complex internal 3D geometries of hierarchical patterns still remain, and it is precisely in this direction that the new techniques are going.

In the next section, the different types of AM technologies will be detailed and it will be explained which of those can be combined with nanotechnology in order to create unique structures with nanometric resolution that would not be possible with other methods.

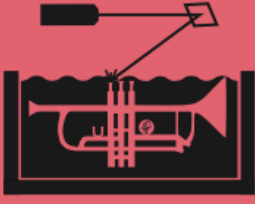
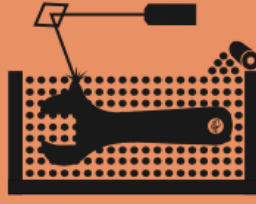


2.3. AM and nanotechnology

AM is a versatile, flexible and highly customizable approach which is suitable for many sectors of industrial production, ranging from large format additive manufacturing (with the production of volumes bigger than 1 m³) to the nanotechnology sector. According to the American Society for Testing and Materials all the AM techniques can be grouped in 7 categories:

- 1) Vat Photopolymerization: Stereolithography (SL), Digital Light Processing (DLP), Continuous Liquid Interface Production by Carbon (CLIP), 2-Photon Polymerization (TPP).
- 2) Powder Bed Fusion (PBF): Selective Laser Sintering (SLS), Electron Beam Melting (EBM).
- 3) Binder Jetting (BJ).
- 4) Material Jetting (MJ): Material injection (MI), Ink Jetting (IJ).
- 5) Sheet lamination: Laminated Object Manufacturing (LOM), Selective Deposition Lamination (SDL).
- 6) Material extrusion: Fused Deposition Modeling (FDM), Direct Ink Writing (DIW).
- 7) Direct Energy Deposition (DED): Direct Metal Deposition (DMD), Laser Metal Deposition (LMD).

These technologies can also be combined forming hybrid technologies which belong to 2 or more of these categories. More information about this is detailed in **Figure 2.7**. The combination of AM and SM can lead to a significant advance in the realizable structuration of the creating object.

In the nanotechnology field it allows to fabricate new materials and devices, as metamaterials, photonic crystals, multi-lens objectives, complex waveguide architectures and components for microfluidics systems^[7,8].

7 Families of Additive Manufacturing			
According to ASTM F2792 Standards			
			
VAT PHOTOPOLYMERIZATION	POWDER BED FUSION (PBF)	BINDER JETTING	MATERIAL JETTING
<p>Alternative Names: SLA™ - Stereolithography Apparatus DLP™ - Digital Light Processing 3SP™ - Scan, Spin, and Selectively Photocure CLIP™ - Continuous Liquid Interface Production</p>	<p>Alternative Names: SLS™ - Selective Laser Sintering; DMLS™ - Direct Metal Laser Sintering; SLM™ - Selective Laser Melting; EBM™ - Electron Beam Melting; SHS™ - Selective Heat Sintering; MJF™ - Multi-Jet Fusion</p>	<p>Alternative Names: 3DP™ - 3D Printing ExOne Voxeljet</p>	<p>Alternative Names: PolyJet™ SCP™ - Smooth Curvatures Printing MJM™ - Multi-Jet Modeling ProJet™</p>
<p>Description: A vat of liquid photopolymer resin is cured through selective exposure to light (via a laser or projector) which then initiates polymerization and converts the exposed areas to a solid part.</p>	<p>Description: Powdered materials are selectively consolidated by melting it together using a heat source such as a laser or electron beam. The powder surrounding the consolidated part acts as support material for overhanging features.</p>	<p>Description: Liquid bonding agents are selectively applied onto thin layers of powdered material to build up parts layer by layer. The binders include organic and inorganic materials. Metal or ceramic powdered parts are typically fired in a furnace after they are printed.</p>	<p>Description: Droplets of material are deposited layer by layer to make parts. Common varieties include jetting a photocurable resin and curing it with UV light, as well as jetting thermally molten materials that then solidify in ambient temperatures.</p>
<p>Strengths:</p> <ul style="list-style-type: none"> • High level of accuracy and complexity • Smooth surface finish • Accommodates large build areas 	<p>Strengths:</p> <ul style="list-style-type: none"> • High level of complexity • Powder acts as support material • Wide range of materials 	<p>Strengths:</p> <ul style="list-style-type: none"> • Allows for full color printing • High productivity • Uses a wide range of materials 	<p>Strengths:</p> <ul style="list-style-type: none"> • High level of accuracy • Allows for full color parts • Enables multiple materials in a single part
<p>Typical Materials UV-Curable Photopolymer Resins</p>	<p>Typical Materials Plastics, Metal and Ceramic Powders, and Sand</p>	<p>Typical Materials Powdered Plastic, Metal, Ceramics, Glass, and Sand.</p>	<p>Typical Materials Photopolymers, Polymers, Waxes</p>
Created and designed by Hybrid Manufacturing Technologies. For more information go to www.hybridmanuftech.com			

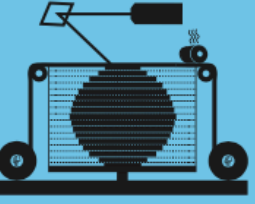
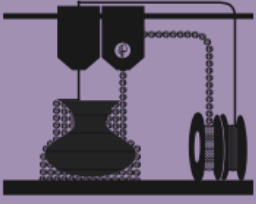


7 Families of Additive Manufacturing			
According to ASTM F2792 Standards			
			
SHEET LAMINATION	MATERIAL EXTRUSION	DIRECTED ENERGY DEPOSITION (DED)	HYBRID
<p>Alternative Names: LOM - Laminated Object Manufacture SDL - Selective Deposition Lamination UAM - Ultrasonic Additive Manufacturing</p>	<p>Alternative Names: FFF - Fused Filament Fabrication FDM™ - Fused Deposition Modeling</p>	<p>Alternative Names: LMD - Laser Metal Deposition LENS™ - Laser Engineered Net Shaping DMD™ - Direct Metal Deposition (DM3D) LENS™ - Laser Engineered Net Shaping DMD™ - Direct Metal Deposition DM3D,</p>	<p>Alternative Names: AMBIT™ - Created by Hybrid Manufacturing Technologies</p>
<p>Description: Sheets of material are stacked and laminated together to form an object. The lamination method can be adhesives or chemical (paper/plastics), ultrasonic welding, or brazing (metals). Unneeded regions are cut out layer by layer and removed after the object is built.</p>	<p>Description: Material is extruded through a nozzle or orifice in tracks or beads, which are then combined into multi-layer models. Common varieties include heated thermoplastic extrusion (similar to a hot glue gun) and syringe dispensing.</p>	<p>Description: Powder or wire is fed into a melt pool which has been generated on the surface of the part where it adheres to the underlying part or layers by using an energy source such as a laser or electron beam. This is essentially a form of automated build-up welding.</p>	<p>Description: Laser metal deposition (a form of DED) is combined with CNC machining, which allows additive manufacturing and 'subtractive' machining to be performed in a single machine so that parts can utilize the strengths of both processes.</p>
<p>Strengths:</p> <ul style="list-style-type: none"> • High volumetric build rates • Relatively low cost (non-metals) • Allows for combinations of metal foils, including embedding components. 	<p>Strengths:</p> <ul style="list-style-type: none"> • Inexpensive and economical • Allows for multiple colors • Can be used in an office environment • Parts have good structural properties 	<p>Strengths:</p> <ul style="list-style-type: none"> • Not limited by direction or axis • Effective for repairs and adding features • Multiple materials in a single part • Highest single-point deposition rates 	<p>Strengths:</p> <ul style="list-style-type: none"> • Smooth surface finish AND High Productivity • Geometrical and material freedoms of DED • Automated in-process support removal, finishing, and inspection
<p>Typical Materials Paper, Plastic Sheets, and Metal Foils/Tapes</p>	<p>Typical Materials Thermoplastic Filaments and Pellets (FFF); Liquids, and Slurries (Syringe Types)</p>	<p>Typical Materials Metal Wire and Powder, with Ceramics</p>	<p>Typical Materials Metal Powder and Wire, with Ceramics</p>
Created and designed by Hybrid Manufacturing Technologies. For more information go to www.hybridmanuftech.com			

Figure 2.7 A scheme of the seven families of Additive Manufacturing technologies according to the American Society for Testing and Materials^[44].

Regardless of the AM technology used, different software tools can be employed to import 3D structure-designs via *Standard Tessellation Language* (.stl) files. The CAD-related packages used in this thesis are DeScribe by NanoScribe and Rhinoceros with the plug-in Grasshopper by Rhino (Figure 2.8).

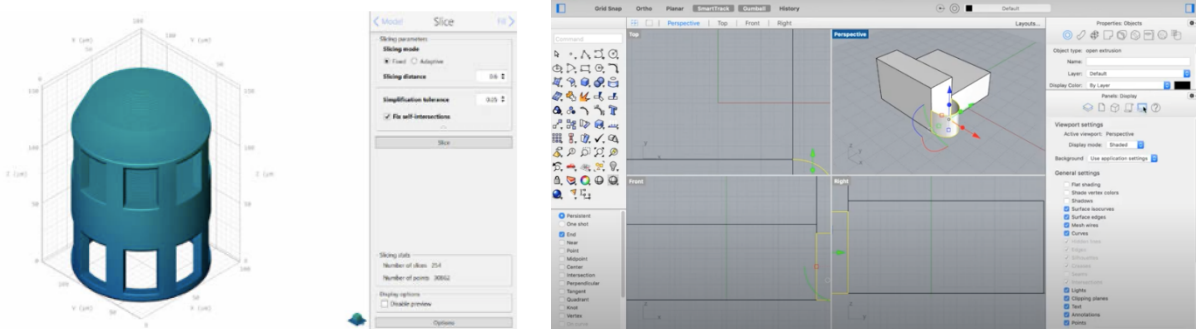


Figure 2.8 *DeScribe* user interface where an object is ready for printing. This is an example of a software to import 3D structure designs (left); *Rhinoceros* user interface to project a 3D object (right).

Regarding the materials that can be used as feedstock, nowadays practically any type of material can be used in most of the AM technologies. The most widely used materials, however are those of polymeric nature. Since AM technologies emerged in the 1980's, the amount of polymeric materials suitable has enormously increased. Currently, a broad spectrum of plastics (including acrylics, polyamides, ABS plastic, assorted polyurethanes, epoxy resins, nylon, etc.) offers an extensive field of possibilities for AM. Additionally, wax can be used for design verification, functional testing, and fine feature details. Currently, the most used plastics are thermoplastic materials in FDM or FFF, while the thermosets (also commonly known as resins) are widely used in vat photopolymerization technologies such as SL, DLP or TPP. These resins are usually of acrylic or epoxy nature.

Polymer matrix based composites using carbon-based additives ranging from carbon fiber to graphene are cutting-edge materials that offer a fast way of producing objects with enhanced mechanical characteristics, in some cases beyond the metallic counterparts. Carbon fiber reinforced composites manufactured by AM are already employed in the bicycle, automotive and aeronautics

industries. Graphene, on the other hand, presents promising applications in the sector of nanotechnology as sensors in microelectronic devices for wearables or biomedical devices. This is possible, thanks, in part, to its efficient heat and electrical conductivity as well as its near-transparent appearance and high flexibility.

AM of metals became available in the 1990's with the invention of laser melting and sintering techniques (3). SLS enables the manufacturing of a huge array of geometrically complex products using a heat source, mainly laser or electron beams, to sinter, or coalesce, powdered material layer-by-layer and so creating a solid structure. It is used for printing the injection molds used in classic manufacturing like casting, as well as for injection molding and carbon fiber lay-up.

Finally, some unusual materials including paper, concrete, food, yarn or even stem cells have also been used as feedstock in AM. Paper for example allows to produce prototypes as a realistic 3D model prior to advancing a product onto final engineering, concrete is currently used for portions of housing and stem cells can be directly printed into the final shape of an organ to be transplanted.

Hence, the possibilities with AM are boundless and encompass numerous industries from plastics and metals up to organic materials and food.

In the particular field of nanotechnology, the development or adaptation of new specific tools for fabrication and measurement is required and AM can easily reach out this demand by providing advanced technical resources. Although the adoption of AM as a means for fabricating end-use components has been historically rejected, there is indeed a strong potential to wholly create new types of materials employing a wide range of polymeric, metallic, ceramic and composite materials and strategies^[45] (**Figure 2.9**). However, not all of these materials and technologies can be directly employed in order to create nanomaterials or nanostructures via AM.

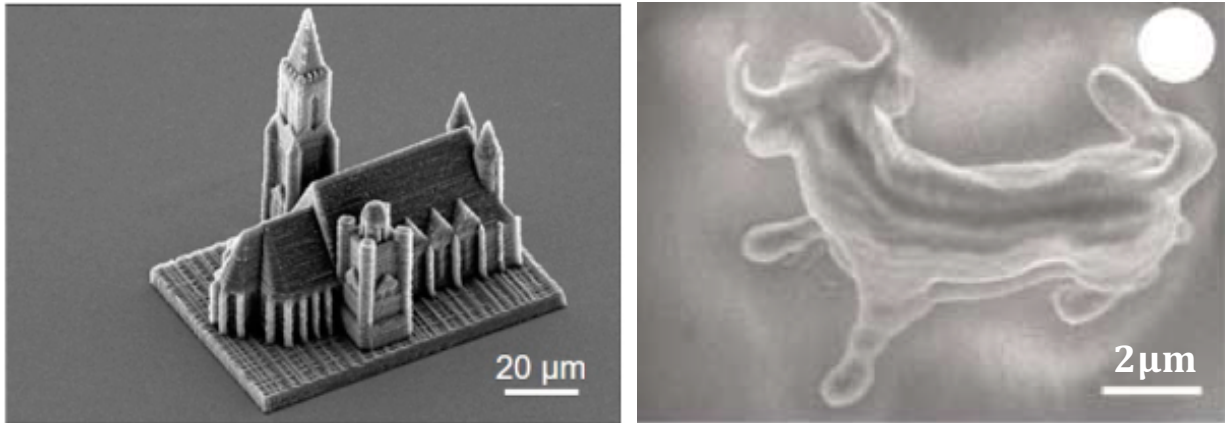


Figure 2.9 Examples of common objects realized exploiting the marriage between nanofabrication and additive manufacturing. (S.C. Ligon et al, 2017, *Chem Rev*; S. Kawata, 2001, *Nature*)^[46,47]

As it is shown in **Figure 2.10**, the AM can be classified according to their ranges of resolutions (X axis) and printing speed (Y axis)^[23]. Namely, in the top X axis it is detailed the range of voxels (abbreviation for volume-pixel) suitable for each AM technique. Hence, the voxel represents the minimum volume that each technique allows to print. In this graph, at the extreme left the smallest unit that can be printed is a 1mm side cube, at the extreme right around 100 nm side cube. The lower the voxel size, the higher the resolution. It can be observed that the current technologies that allow to print with sub-micrometric resolution are two-photon polymerization (TPP), electrochemical printing (ECP) and electron beam induced deposition (EBID) technologies^[48]. However, stereolithography (depicted in the graph as (Pμ)SL) and direct ink writing (DIW) also allow to print with resolutions of 1-10 μm. These techniques, combined with other technologies or the use of specific additives would easily allow to reach resolutions below 1 μm^[46,49]. The printing speed in the Y axis is not represented in typical terms of amount of volume or mass printed per time. Instead, to make all these technologies more comparable, it is depicted as an amount of voxels that can be printed per second (i.e. amount of information in bits that can be transformed into an actual, physical object per unit of time). This is the velocity necessary to transfer the digital information in to the amount of material printed since the starting point is always a digital file. The graph shows that, among the different AM technologies with sub-micrometric resolution, those based on TPP are the ones more promising in terms of higher

printing speed. Likewise, when compared DIW and SL techniques, it is observed that SL allow in general faster printing speeds than DIW.

This graph also illustrates with parallel oblique lines the printing speed in terms of deposited volume in mm^3/s . These lines allow to compare which AM technology would be faster to print a desired constant volume. For instance, when observing the line for $10^{-3} \text{ mm}^3/\text{s}$, it falls in both the region of SL (when the resolution is higher) and TPP (when the printing speed is higher). This means that both technologies are able to print at the same printing speed but with different resolution. In fact, for TPP the resolution achieved is higher. However, it must be noted that for some applications in micromechanics or electronics, a resolution of 1-10 μm can be enough and SL can be used with a larger variety of materials.

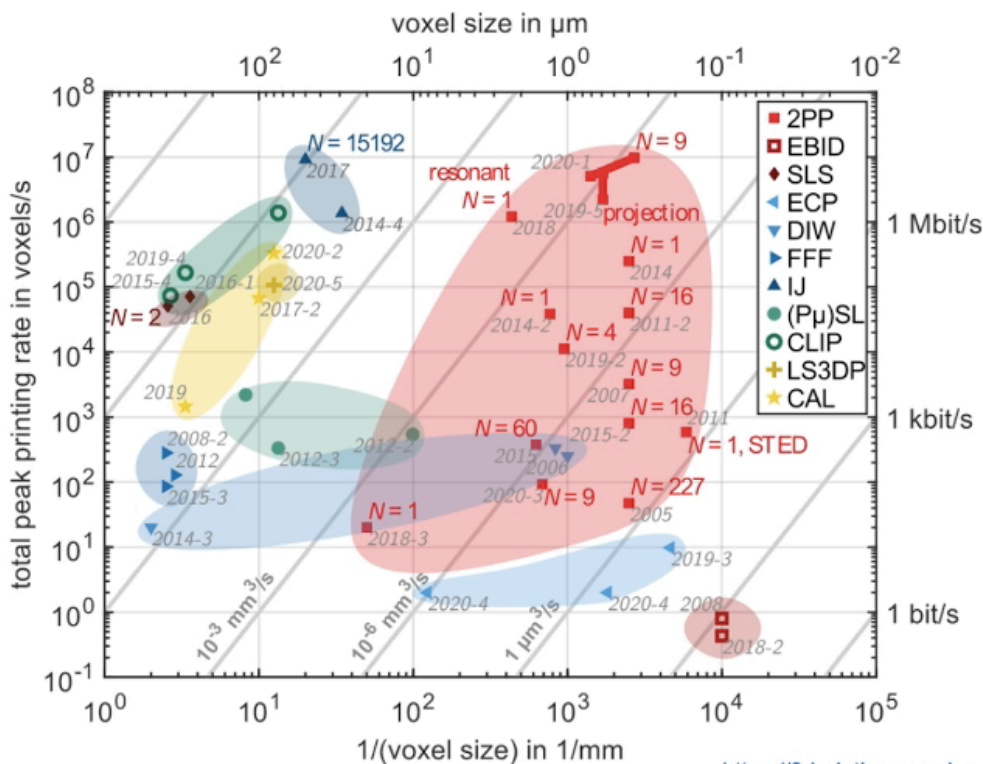


Figure 2.10 Comparison of the different AM techniques as a function of the voxel size and the production time. In detail speed (total peak printing rate) plotted on the vertical axis is given in units of voxels per second on the left scale while in bits per second on the right scale. The gray diagonals correspond to lines of constant volume printing rate. The inverse of the voxel size is associated with the resolution. Figure and caption are adapted from: Hahn, V., Kiefer, P., Frenzel, T., Qu, J., Blasco, E., Barner-Kowollik, C., Wegener, M., “Rapid Assembly of Small Materials Building Blocks (Voxels) into Large Functional 3D Metamaterials”. *Adv. Funct. Mater.* 2020, 1907795. doi.org/10.1002/adfm.201907795 [23].

In conclusion, SL and TPP effectively have a strategic position for the nanotechnology sector, as evidenced in the graphic shown in **Figure 2.10**: while techniques like SLS and FDM stay on the left, with a resolution around 100 μm (where SLS has a higher speed than FDM), SL and TPP are located in the central-right part of the graphic with higher resolution and adequate printing speed. Hence, it is proven that vat photopolymerization techniques are the most competitive in terms of printing objects with high resolution at an acceptable printing speed for mass production. In the particular case of SL and TPP, the physics behind these two technologies is quite similar, using a laser as the source of energy to print the 3D objects. In the next section these two techniques will be explained more in detail.

2.4. Laser-assisted AM techniques: SL and TP-DLW

2.4.1. Stereolithography (SL)

The very first time that an AM equipment is reported was in the 1984, when an SL apparatus was patented by Chuck Hull of 3D Systems Corporation^[50]. Hull defined the 3D printing process as a system for generating three-dimensional objects by creating a cross-sectional pattern of the object to be formed. His invention consists indeed of a SL fabrication system (2), that it is still one of the most popular 3D printing manufacturing techniques, involving a liquid photopolymer contained in a vat or tank, selectively cured by a heat or irradiation source, with different types of curing devices, typically using lasers ranging from ultraviolet (UV) to near infrared (NIR) light.

SL allows to process liquid-form material to selectively cure it from a liquid vat or to locally deposit and cure it^[51]. The laser, in general in the range of 300 - 400 nm (UV light), is the responsible of activating the photopolymerization. This process converts the resin from liquid to solid often via a chemical crosslinking process and to understand the crosslinking reaction between multifunctional pre-polymers in an SL resin is fundamental to modify existing resins or create new formulations

tailored for specific applications. Manifold are the components needed in the SL resin to achieve high printing quality as the monomer/oligomer, diluent, chain transfer agent and photo-initiator.

The monomers/oligomers are the reactive pre-polymers that can increase the extent of crosslinking, in general they are poly-acrylate derivatives where the C=C bonds in vinyl groups crosslink with different monomers, especially methacrylate-based monomers are used because of their low cytotoxicity and high heat resistance. The molecular weight of the monomer/oligomer influences the viscosity of the liquid resin, for this reason diluents are also employed to modify it changing wetting and impregnating properties during the printing. Chain transfer agents are necessary for regulating network formation to enhance the overall properties of printed parts. Lastly, the photo-initiators, which can be α -cleavage or H-abstraction like, depending on the free radical generation mechanism. The first type requires a specific range of UV irradiation and it has a structure that will break and form two separated parts both of which contain the free radical (e.g. DMPA). The second type needs a co-initiator which contains free radicals too (e.g. benzophenone).

One of the main drawbacks of this kind of technology is the increase of viscosity and the possible sedimentation phenomena that tend to strongly limit the use of filled photo-curable resins in both SL and DLP technologies^[11,26,35,36]. In this direction research moves to improve the condition of the filled resin acting on the homogenization of the composite and on the optimization of the curing parameters, the curing depth C_d and the curing width C_w ^[52] which determine the printing details^[5]. The theoretical respective expressions are derived from Beer–Lambert and they are:

$$C_d = D_p \ln \frac{E}{E_c} \quad (1)$$

$$C_w = F \sqrt{\ln \frac{E}{\varphi \cdot E_c}} \quad (2)$$

where D_p is the penetration depth and depends on the intrinsic properties of the resin used including loading and size of nanoparticles and the refractive indices; F and φ are determined by the laser beam profile and the nature of resin composite; E is the exposure while E_c is the critical exposure from

initiating the polymerization, that solely depends on the photo-initiator as well as liquid monomer.

To determine E we can use the equation:

$$E = \frac{2 \cdot lp_0}{\pi \cdot w_0 \cdot v_s} \quad (3)$$

where lp_0 is the power of the laser at the surface of the resin, w_0 is the beam radius at e^{-2} and v_s is the scan speed.

2.4.2. Direct Laser Writing and TPP

A higher resolution than with SL can be reached with Direct laser writing (DLW), a laser scanning fabrication technique, suitable to mask-less print structures into a photoresist. The resolution in this case depends solely on the beam waist of the used laser beam and its output power^[6–8,53]. When the optical absorption is governed by single-photon processes, this technique allows for 3D patterning with resolutions down to typically few microns, in the same order of that given by SL.

However, DLW evolves as an AM technology able to fabricate 3D micro-objects with sub-micrometer feature sizes and optically smooth surfaces when it is combined with the two photon absorption (TPA) or multi-photon absorption (MPA)^[54]. By combining the DLW with these processes, the technique can create features of hundreds of nanometers or less, thus well below the diffraction limit.

The two photons absorption (TPA) process is a non-linear third order optical phenomenon that can occur in a material between electronic states featuring the same inversion symmetry, providing that an intensity “threshold” is overcome, using narrowly focused pulsed lasers (100 fs). Typical values for the TPA cross-section of the used materials is in the order of $10\text{--}50 \text{ cm}^4 \cdot \text{s} \cdot \text{photon}^{-1}$ ^[55–61]. The achievable high spatial resolution is due to the square dependence of the TPA process on the radiation intensity that further narrows the Gaussian laser beam intensity profile, along with the presence of the intensity threshold for the TPA triggering. The inner volume of the laser beam focus figure where the TPA threshold is overcome is the smallest polymerizable volume (voxel), whose size depends

mainly on the laser intensity and on the numerical aperture of the used focusing lens. On the other side, the voxel size depends also on the optical homogeneity (at the laser wavelength) of the stack crossed by the laser beam traveling from the front lens to the focal spot^[61,62].

In the fabrication process, the laser focus is swept through a photoresist by a 3D stage, reproducing a 3D model made by a Computer Aided Design software (CAD), or analytical 2D/3D trajectories. In the first case the file is 'sliced' and each slice is afterwards "hatched" in single segments, according to the used voxel size. As it happens for SL, CAD/CAM like files are used and modified depending on the desired structure.

To move the beam focus or the sample and carry on the fabrication process, or a high-resolution xyz stage is used. In commercial systems the x-y positioning can be done by a galvo steering beam system that speeds up considerably (some orders of magnitude) the fabrication process, with the same accuracy offered by a x-y piezo movement. Nevertheless, the focus accuracy could be affected for large sweep angles, as it actually moves on a spherical surface. In any cases the z axis requires a different high-resolution translation stage, as piezo or motors. Motorized stages for the xy-axes movement, in addition to the z-axis can be used to allow large-scale movement along all the three axes.

The multiphoton absorption clearly requires high intensity and consequently, tightly focused laser beam are used. For these reasons, microscope objectives are employed and different operative configurations can be adopted. The most interesting uses the same resin as immersion medium for the objective, addressing the issue of the short lens working distance (in the order of 500 μm) that can limit the height of the fabricated structures.

The photopolymers can be selected in a wide range. In fact, it is possible to use resins (e.g. acrylates or epoxy resins), organic and natural photopolymers (bovine serum albumin (BSA), collagen...), hydrogels (hydrated PEG) and commercial photosensitive hybrid materials with proprietary formulation (ORMOCER, ORMOCOMP, ORMOCLEAR...). As in SL, these materials are in general constituted by a monomer or a mixture of monomers/oligomers which provide the final

polymer and a photo-initiator, the trigger of the photopolymerization. Both the monomer/oligomer and the photo-initiator must be transparent at the wavelength of the laser used, while the monomer/oligomer must be transparent at the two-photon absorption wavelength and the photo-initiator is specific (in the sense that a common UV photo-initiator would not necessarily make his job) absorb for the TPA process.

So far, it has been only described the combination of DLW with TPA in the practical case of TPP. However, these two aspects can be combined with other materials such as metals, nanocomposites or glassy structures. Hence, from now on we will describe this technique as *Two-photon Direct Laser Writing* (TP-DLW), which will encompass TPP and the laser-assisted AM of any other material with sub-micrometric resolution.

2.4.3. Theory behind SL and TP-DLW

As we previously discussed, SL and TP-DLW belong to the laser-assisted, vat photopolymerization category of AM techniques and they are the two best candidates for the analysis we want to perform in this work on nanofabrication, for this reason, we are going to explore in more detail the features of these two technologies and in general of the mechanism of the TPP, at the base of the TP-DLW that we will use along this thesis work

Briefly, SL physically works as a single photon absorption process (SPA) while the TP-DLW takes advantage of the two-photon absorption process (TPA).

SPA is a linear absorption process whereby one photon excites an atom, ion or molecule from a lower energy level to a higher energy level, for example, from the ground state to the first excited state.

The single photon absorption (SPA) processes allow to realize 3D patterning with the same resolution of the lithography mask (**Figure 2.11**).

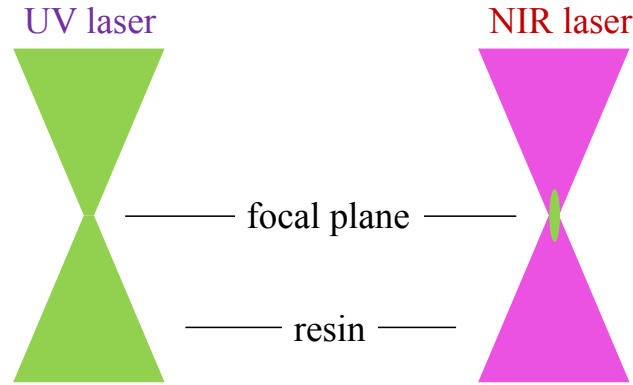


Figure 2.11 *Single Photon (left) vs Two Photon Polymerization (right) representations in terms of polymerized area*

SPA is also employed to achieve a first polymerization of an object, for instance when this is a composite that needs different treatments, in this case the SPA constitutes the first step to polymerize the photopolymer and then it will be finished by a thermal treatment or a UV curing.

TPA and MPA processes can improve hugely the resolution of the details in the objects obtained with SPA up to 50 nanometers.

Although physical principles of the TPA process underlying TP-DLW are known since the early 1930s when they were discovered by M. Goepfert-Mayer^[57], and they were first observed experimentally by Kaiser and Garrett (1961)^[31], the practical consequences of this phenomenon were introduced decades later. The first works on the TPA employment for photo-polymerization date back to the late 1990s (after the experimental demonstration of Maruo and Kawata^[63]) and the phenomenon has been relegated only to scientific curiosity for a long time or used for few laboratory research purposes only. The TPA process is a threshold, third order non-linear optical process, whose cross-section depends on the square of the intensity of the laser beam (typically a NIR femtosecond laser). If SPA is a linear optical process, TPA is the first example of the non-linear processes occurred in category of the multiphoton absorption phenomena. Non-linear optical phenomena involving the modification of the optical properties of the materials by the presence of light, are non-linear in the sense that the response of the material system to an applied optical field depends in a non-linear

manner on the strength of the field itself^[64]. To visualize better this correlation, we can describe it through the polarization $\vec{P}(t)$, the dipole moment per unit volume of a material system, depending on the electric field strength $\vec{E}(t)$, as follows:

$$\vec{P}(t) = \epsilon_0 \chi^{(1)} \vec{E}(t) \quad (4)$$

where $\chi^{(1)}$ is the linear susceptibility and ϵ_0 is the permittivity in free-space. In non-linear optics we can rewrite the optical response expressing the polarization as a power series in $\vec{E}(t)$ following the relationship:

$$\vec{P}(t) = \epsilon_0 [\chi^{(1)} \vec{E}(t) + \chi^{(2)} \vec{E}^2(t) + \chi^{(3)} \vec{E}^3(t) + \dots] \equiv \vec{P}^{(1)}(t) + \vec{P}^{(2)}(t) + \vec{P}^{(3)}(t) + \dots \quad (5)$$

where $\chi^{(2)}$ and $\chi^{(3)}$ are non-linear susceptibilities of second and third order.

To write the relation between the number of photons (or the order of the electronic transitions) and the order of the corresponding susceptibility we refer to probability amplitude of an optical $\chi^{(n)}$ process calculated according to the perturbation theory where:

$$m = n + 1 \quad (6)$$

The imaginary part of an all-optical process is related to a process involving charge carries with half the perturbation order ($m/2$) which, for TPA, is $2 \left(\frac{m}{2} = 2 \rightarrow m = 4\right)$ resulting that $n = 3$ so this explains how TPA is a third order process.

To express how the time-varying polarization can act as a source of new components of the electric field we can exploit the wave equation written in this way:

$$\nabla^2 \vec{E} - \frac{n^2}{c^2} \frac{\partial^2 \vec{E}}{\partial t^2} = \frac{1}{\epsilon_0 c^2} \frac{\partial^2 \vec{P}^{nl}}{\partial t^2} \quad (7)$$

where n is the refractive index, c the speed of light in vacuum and \vec{P}^{nl} the time-varying polarization that acts as the source term for the electric field \vec{E} , consistent with the Larmor's theorem of electromagnetism asserting accelerated charges generate electromagnetic radiation.

In the TPA, two laser photons of frequency ω are absorbed simultaneously by the atom allowing the transition from its ground state to an excited state (**Figure 2.12**).

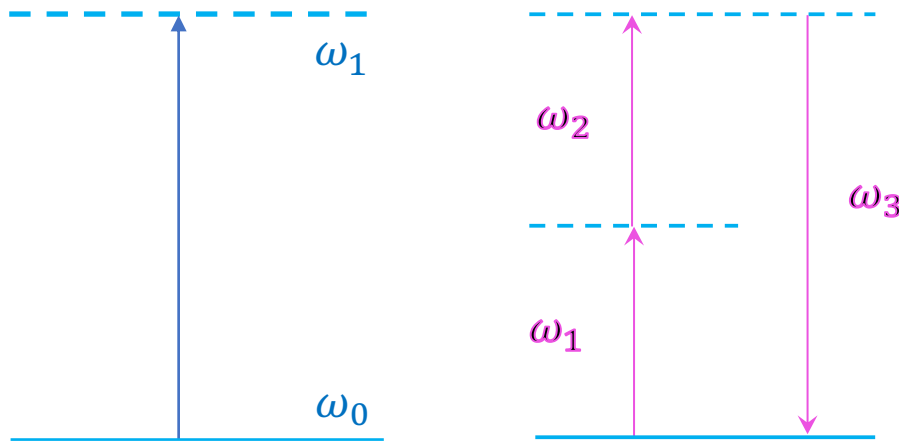


Figure 2.12 *SP and TP absorption process where one (left) or two photons (right) are absorbed and allow the transition to the higher level of energy.*

If in conventional linear optics the cross section describing the absorption process is a constant, in the two-photon absorption process the cross section increases linearly with laser intensity represented by the coefficient $\sigma^{(2)}$ that describes the strength of the process:

$$\sigma = \sigma^{(2)}I \quad (8)$$

Therefore, the rate of the atomic transition ($R = \sigma I / \hbar\omega$) clearly scales as the square of the laser intensity ($R = \sigma^{(2)}I^2 / \hbar\omega$) and it means that we need a very high density of photons for the process to occur. It is for this reason that we need pulsed tightly focused lasers of 100 fs typically which release very high energy. Generalizing to the multiphoton absorption we have $\sigma = \sigma^{(k)}I^k$ for absorption of k photons. It must be noted that on the contrary, the number of photons required is determined by the smallest k which satisfies the relation $k\hbar\omega \geq E_g$ where E_g is the band-gap energy [65,66].

The cross section of TPA is $1 \text{ GM} = 10^{-50} \text{ cm}^4 \text{ s photon}^{-1}$, in the unit that takes name from M. Goeppert-Mayer herself, and it is several orders of magnitude smaller than that of the single photon absorption, SPA, usually in the order of 10^{-16} cm^2 . Therefore, a large enough photon density is required^[58], as in the case of a tightly focused laser beam.

Polymerization occurs only inside the voxel where the TPA “threshold” is overcome. It is important to point out that the term “threshold” here doesn’t refer to any critical phenomenon, as from a principle point of view, TPA becomes only relevant beyond the “threshold”. The Gaussian intensity profile, along with the presence of a threshold, makes possible the achievement of a resolution in the order of hundred nanometers. 3D structures can be then created sweeping the laser and ‘recording’ the beam path. However, only with the recent explosion of nanotechnologies, we have been experiencing an exponential acceleration of the uptake of this nano-fabrication technique, in fact now there are at least two producers where it is possible to buy nano/micro 3D printing systems with polymeric materials ready to use, and consumables optimized by the same producer. On the other hand, the enormous versatility of these systems determines an increasing request of the specific materials development. Apart from the applications in AM of nanomaterials, TPA can be useful as a spectroscopic tool for determining the positions of the energy levels that are not connected to the atomic ground state by a one photon transition^[64].

2.4.4. Advantages and disadvantages of the techniques

In order to find the best technique to satisfy different needs related to micro- and nanofabrication it can be useful to compare them from different perspectives.

From the point of view of the resolution, TP-DLW is clearly better since with the TPA and MPA, a resolution under the diffraction limit (in particular, down to 50 nm) can be achieved. Even though, higher resolution implies longer printing times.

Moreover, the equipment to achieve such high resolution are more expensive and the amount of materials that can be used are significantly lower, since they must fulfill with the TPA condition.

Because of that, it is reasonable to use the TP-DLW technology for the smaller parts of micro-devices that need the highest accuracy in details, for example internal structures in micro-channels or microchips and then print the rest of the micro-device (structural components such as external case, supporting elements...) using SL.

Finally, it is possible to print with different materials valid both for SL and TP-DLW. Since these technologies belong to the same AM category, similar (if not the same) materials can be used in both cases, which will probably enhance the structural integrity of the micro-object printed. As it has been mentioned before, examples of materials that can be used in TP-DLW include epoxy, polyurethane and acrylic resins and hydrogels, but also the choice of metals and ceramics with a further post-processing with other techniques as atomic layer deposition, chemical vapor deposition or pyrolysis. Hence, there is plenty of options still to be explored in the use of novel materials beyond polymers suitable for these laser-assisted AM technologies.

2.5. New materials for NF with AM: nanocomposites and non-polymeric nanostructures

One promising path to enhance the mechanical and functional properties (e.g. electrical, thermal, optical...) of the already well-established polymers for SL and TP-DLW is to embed nanomaterials. Carbon-based nanomaterials are one of the most widespread fillers in the development of new nanocomposite materials given their good mechanical and functional properties. For instance, carbon nanotubes are among the strongest and stiffest materials known that can be also used in the AM process because they possess unique electrical and thermal conductivities^[67-69]. Carbon nanotubes have been consequently used as additives to polymers to improve mechanical, thermal, and electrical properties^[70-72]. They have found applications in hydrogen storage, field emission devices, sensors, and scaffolds for damaged nerve regeneration^[45]. Moreover, nanocomposites based on graphene nanoplates have also been printed via SL. These materials showed enhanced stiffness and electrical properties^[73].

Transparent materials could be embedded in a polymeric matrix, and processed by SL and TP-DLW with loads of filler, since they are not likely to interfere with the laser path. It must be considered, though, that the closer the refractive indices of both are, better is the performance in terms of the achievable resolution. This condition can be fulfilled by tuning the refractive index of the filler or by

adding a suitable dopant in the production process by coating the substrate with a thin layer of a high refractive index oxide,^[74,75] or by adjusting that of the polymer during the synthesis.^[76,77]

On the other hand, metallic nanocomposites are a combination of organic/inorganic materials where the metallic constituent has nanometric dimensions and plays a key role in the improvement of the properties of the pristine matrix. They can be realized *ex-situ* by dispersing previously-synthesized metallic nanoparticles in a polymer being able to choose in this way the size and the shape of the nanoparticles^[78] or *in-situ*, synthesizing the nanoparticles directly in a polymer by using the corresponding metallic precursor^[51]. Some of the most employed metals as additives are iron, silver or gold, which can be employed in combination with the printing materials to improve the final properties of the composites obtained. It has been proved that the use of metal nanoparticles, very popular because of their optical, thermal and electrochemical properties, is really helpful in the sintering characteristics: for instance, iron nanoparticles can be used to improve the sintering quality of steel parts created by 3D printing^[79–81]. Nanoparticles can be infiltrated, oxidized or used as nano-binders to decrease the deflection and the shrinkage of some materials printed. Silver nanoparticles can also be employed to improve the production of microelectrodes^[82–84] printed with these composites to change the electrical conductivity after annealing treatments. Silver and gold nanoparticles possess unique optical and electric properties. When they have sizes significantly below the visible light wavelengths (i.e. diameters below 100 nm) they also possess very interesting plasmonic properties. These properties can be finely tuned not only by varying the size, but also the morphology and polydispersity, which makes them versatile candidates in the development of devices for surface enhanced Raman scattering or biosensors^[85,86].

Besides, taking advantage of the TPA and MPA processes, metallic nanostructures can be obtained by reduction of a metal ion precursor. This would expand the TP-DLW applications beyond the TPP of polymeric resins into the direct fabrication of metallic structures^[87].

For the development of these new, more complex materials, the nanoparticles or their precursors must be embedded in a polymeric matrix.

Thus, a study of diffusion and the kinetics of the process are important to understand the physics behind the reactions and pave the way to the possibility of tuning the different features of the nanocomposites varying the concentration and the times of the process.

A help to this kind of study comes from Fick's law diffusion, in fact the dynamics of the ions inside a polymeric matrix.

Understanding the physicochemical processes behind the distribution of the nano-additives and the nanofabrication will contribute to create new materials and expand current range of applications including medical and microfluidic devices to electronic components and small satellites while the printing resolution is maintained^[9,54,55,58,60,90]. For instance, TP-DLW can be exploited to fabricate scaffolds imitating extracellular matrices and to culture cells there *in vitro* or *in vivo*, in the development of chiral metamaterials with unique properties or in micro-electro-mechanic systems (MEMS) as actuators^[91,92].

In this context, this doctoral thesis proposes a series of new nanocomposite materials and metallic nanostructures, which can be printed using SL and TP-DLW. The work will reveal how different variables and materials affect the 3D printing processes. Furthermore, due to the technological nature of this thesis, the potential applications of these new materials in the nanotechnology sector will also be discussed.

Unfortunately, several experiments have been inhibited by the pandemic situation of the last years. In fact, during the health emergency there was no chance to use all the research infrastructures. The missed experiments include in particular that regarding the use of surfactants to stabilize all the "inhomogeneous" emulsions given by mixing hydrophilic and hydrophobic materials.

Moreover, the use of a micellar phase would allow an almost absolute control on the AuNPs, as each single micelle constitutes a nano-reactor with well-defined volume and metallic precursor content.

3. Aim of the thesis

The aim of this thesis is to identify a new set of materials, AM technologies and combination of both that lead to the nanofabrication of new materials with improved mechanical and functional properties and potential applications in the industrial sector. In particular, the use of SL and TP-DLW technologies has been exploited in the nanofabrication of gold nanocomposites, gold nanostructures and fiber reinforced polymer nanocomposites with silica nanowires.

The particular aims in the research conducted using SL are to:

- Select a combination of polymer and gold precursor which meet the processability requirements of SL.
- Define the range of concentration of gold precursor which permits the successful fabrication of gold nanocomposites via SL without inhibition of the photopolymerization.
- Fine-tune the printing and post-processing conditions (UV-dose, temperature and time) to optimize the synthesis of nanocomposites, including the size and morphology of the gold nanoparticles.
- Evaluate the optical and plasmonic properties of the nanocomposites and correlate them with the microstructure of the material.
- Manufacture different 3D objects with different shapes and sizes, keeping a printing resolution of 10-100 μm .

The particular aims in the nanofabrication of metallic structures via TP-DLW are to:

- Select a combination of materials which meet the processability requirements of TP-DLW permitting to achieve a resolution below the optical diffraction limit and develop reproducible, new metallic nanomaterials with defined micro- and nanostructure.

- Find strategies to enhance the quality of the micro/nanostructures, by preventing the swelling of the polymer matrix used and the removal of the non-polymerized or non-reduced material.
- Optimize the TP-DLW printing conditions, including the scanning speed, exposure time and laser power to have a set of different nanostructures with controlled size, morphology and density.
- Understand the kinetics behind the synthesis and growth of the nanostructures to predict their behavior under different experimental conditions.

The particular aims in the nanofabrication of fiber reinforced polymer nanocomposites via TP-DLW are to:

- Evaluate the use of SiO₂ NWs as new substrates for the nano-polymerization of resins via TP-DLW and study their suitability to reduce the processing times and optimize the fabrication of fiber reinforced nanocomposites.
- Improve the mechanical properties of the commercially available resins for TP-DLW by including SiO₂ NWs in high amounts to expand the range of application of these materials.
- Demonstrate that the use of these substrates may increase the versatility of the TP-DLW technique since they can be used as sacrificial layers or scaffolds to produce porous nanomaterials.

4. Materials and Methods

4.1. Materials

In all cases, the reagents were used as received without further purification under ambient conditions (22 ± 1 °C and 45 ± 10 % RH). All solutions were prepared using deionized water.

4.1.1. Materials for gold nanocomposites via SL

Potassium tetrachloroaurate (III), (KAuCl_4 , $M_w = 377.88$ g/mol), purchased from Acros, was used as gold precursor. Acrylic resin Form Clear v2 (FLGPCL02, proprietary mixture of photo-initiator and of acrylic monomers and oligomers) was purchased by Formlabs. This resin is compatible with Form 1+ SL printer and allows printing with resolutions from 25 to 200 μm . Isopropanol (IPA) was purchased from Scharlau. Rectangular glass coverslips (24 x 32 mm, 0.10 mm thickness) and round coverslips (13 mm diameter, 0.10 mm thickness) were purchased from Ted Pella Inc. UV-grade, polystyrene disposable macro-cuvettes (4.5 mL) were purchased from Kartell.

4.1.2. Materials for gold nanostructures via TP-DLW

Tetrachloroauric (III) acid trihydrate ($\text{HAuCl}_4 \cdot 3\text{H}_2\text{O}$, $M_w = 393.83$ g/mol) and Polyvinyl alcohol (PVA, $M_w = 13.000\text{--}23.000$ g/mol) were purchased from Sigma-Aldrich. Fish tail collagen (isinglass) was purchased from Cameo. Commercial isotropic photoresists IP-S, IP-DIP and IP-L 780 by Nanoscribe GmbH, the first two optimized for oil-immersion configuration, suitable for plasmonic, photonic and biometric surfaces that allow a resolution down to 50 nm, are used to perform TPP on a substrate of glass singly or along with the gold precursor or the nanofiller. Coverslips ($22\text{mm} \times 22\text{mm} \times 0.17\text{mm}$) and microscope coverslips, silicon polished substrates were purchased from specialized suppliers.

4.1.3. Materials for fiber reinforced polymer nanocomposites (FRPN) via TP-DLW

Silicon wafers with a layer of Silica Nanowires were made according the PECVD protocol (plasma + SiH₄) in the Institute for Microelectronics and Microsystems (IMM-CNR, Rome); IP-S 780 from Nanoscribe GmbH (composed by 95% of carbamate and metacrylate, by less than 5% Gamma-Butyrolactone and by less than 1% of photo-initiator, attached to aromatic rings); fused Silica Glass coverslip 22x22 mm, 170 μm thick, Polypropylene Glycol Methyl Ether Acetate (PGMEA), Isopropanol (IPA), hydrofluoric acid (HF), distilled water, hydrochloric acid (HCl), Buffered solution (40 g of NH₄F, 60 ml of distilled H₂O and 10 ml of HF at 49%); aqueous solution of hydrofluoric acid (85 ml of distilled H₂O, 10 ml of HCl and 5 ml of Buffered HF Solution). All the solvents and the other products are purchased from specialized suppliers.

4.2. Additive Manufacturing technologies

4.2.1. Fabrication of gold nanocomposites via SL

Resin precursors containing 0.01 - 2.0 wt% KAuCl₄ were prepared in all cases by directly dissolving the KAuCl₄ into the FLGPCL02 acrylic resin under sonication for 30 min in order to obtain a homogeneous yellow solution.

4.2.1.1. Preliminary tests

Prior to SL printing of the gold nanocomposites, various preliminary tests were done to see the influence of the presence of KAuCl₄ in the curing of the FLGPCL02 resin. These tests consisted of different UV and thermal treatments to identify a range of KAuCl₄ concentrations suitable for SL printing which led to the formation of nanocomposites containing AuNPs. In all cases the UV treatments were done inside a UV-chamber (FormCure, Formlabs) equipped with a light source of 405 nm and power of 1.25 mW/cm².

This chamber can be used under temperatures ranging from 25 to 100 °C. Thermal treatments were done inside a Nabertherm muffle oven, which can be heated up to 3000 °C.

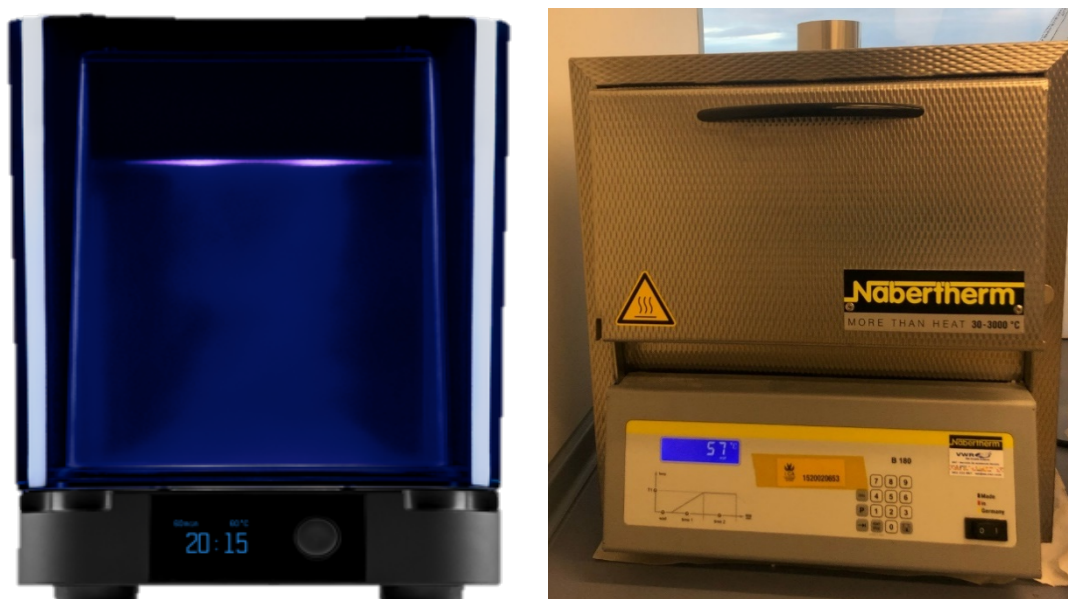


Figure 4.1 *Equipment for the different treatments: the Formlabs FCure UV-chamber for the UV-curing (left) and the muffle oven Nabertherm for the thermal treatments (right).*

The preliminary tests can be divided into 2 groups:

- a) Influence of UV-curing inside UV-Vis cuvettes. Approximately 1 mL of different resin precursors containing up to 2 wt% KAuCl_4 were poured inside UV-Vis macro cuvettes. Then, the cuvettes were introduced inside the UV chamber for 60 min at room temperature. These samples can be further used for UV-Vis spectroscopy to see the influence of the curing of the resin.
- b) Influence of combination of UV and thermal treatments. In order to see the AuNPs formation, the resin precursors containing 0.1 – 1.0 wt% KAuCl_4 were subjected to 4 different treatments, including UV treatments, thermal treatments and combinations of both. These treatments were done either into “droplet samples” and “sandwich samples”. Droplet samples were prepared pouring a small volume (less than 0.1 mL) of the resin precursor onto a round glass coverslip

while sandwich samples were prepared by pouring the same amount onto a rectangular glass coverslip and placing another rectangular coverslip immediately after to form a homogeneous, thin film. Then, these samples were subjected to different UV and thermal treatments as indicated in the **Table 4.1**.

Table 4.1 *Different treatments done to the droplet and sandwich samples. The first treatment was made to cure of the resin precursor while the second treatment was made to reduce the gold precursor into AuNPs.*

	First treatment	Second treatment
UV + (UV+T)	UV, T = 25 °C, t = 1 h	UV, T = 80 °C, t = 1 h
UV + T	UV, T = 25 °C, t = 1 h	T = 170 °C, t = 1 h
(UV+T)	UV, T = 80 °C, t = 1 h	-
T + T	T = 80 °C, t = 1 h	T = 170 °C, t = 1 h

Droplet samples were adequate for further characterization in SEM while sandwich samples were used for further characterization in UV-Vis spectroscopy.

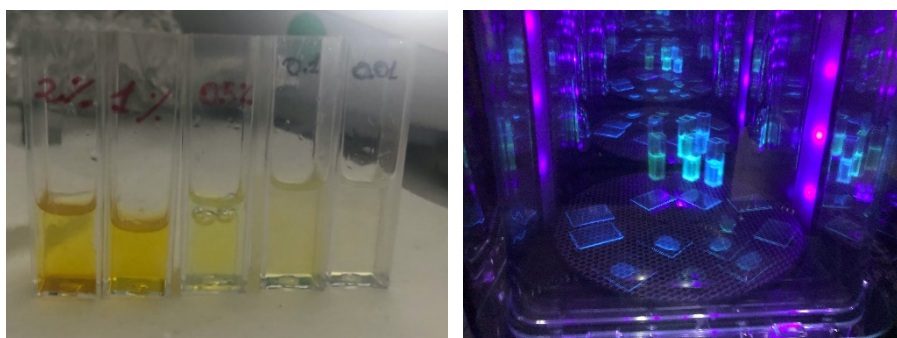


Figure 4.2 *UV-Vis Macro-cuvettes containing different concentrations of KAuCl₄ before the UV-curing treatment of 60 minutes.*

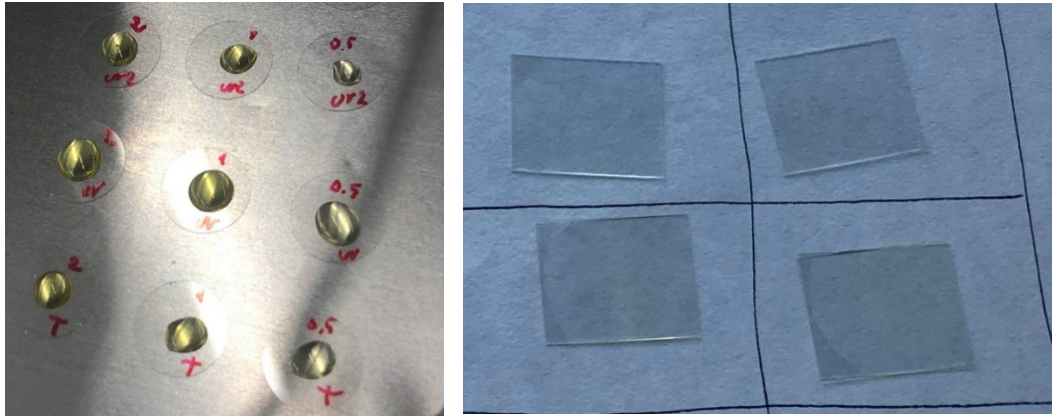


Figure 4.3 *Illustrative examples of droplet and sandwich sample*

4.2.1.2. 3D-printing via SL

The range concentrations that led to the best results in the preliminary tests (up to 0.5 wt% KAuCl_4 , see chapter 5 for more details) were used to produce actual 3D-printed objects with the SL printer (Form 1+, Formlabs). In particular, monolayers of 0.2 mm and 0.025 mm thickness and parallelepipeds (25 x 25 x 2 mm) were printed. For this purpose, digital file projects were created using a CAD software and then were loaded with the *.form* or *.stl* extension onto the SL printer.

In a similar manner as done with the preliminary tests, the acrylic resin FLGPCL02 is mixed under sonication with the gold precursor before pouring the mixture into the tank. In all these cases, the volume of resin used is 50 mL, which is the minimum recommended by the manufacturer of the SL printer to achieve good results.

The Form 1+ SL apparatus consists of a 405 nm laser acting on a focalized spot in a photosensitive resin precursor placed in a reservoir (**Figure 4.4**). The laser starts the photopolymerization solidifying the resin into a 2D patterned layer via chemical crosslinking, following the CAD-like project with the object to be printed. After one layer is cured, the printing platform moves up in a range of 25 to 200 μm (depending on the desired resolution of the object) before printing the next layer. After the objects are completely printed, a plastic spatula is used to remove them from the build platform. Then, objects are washed in a IPA solution for at least 15 min to remove possible unreacted monomer of the resin.

Finally, the objects were UV-postcured for 60 min at room temperature and underwent a subsequent thermal treatment at 170 °C for 60 min.

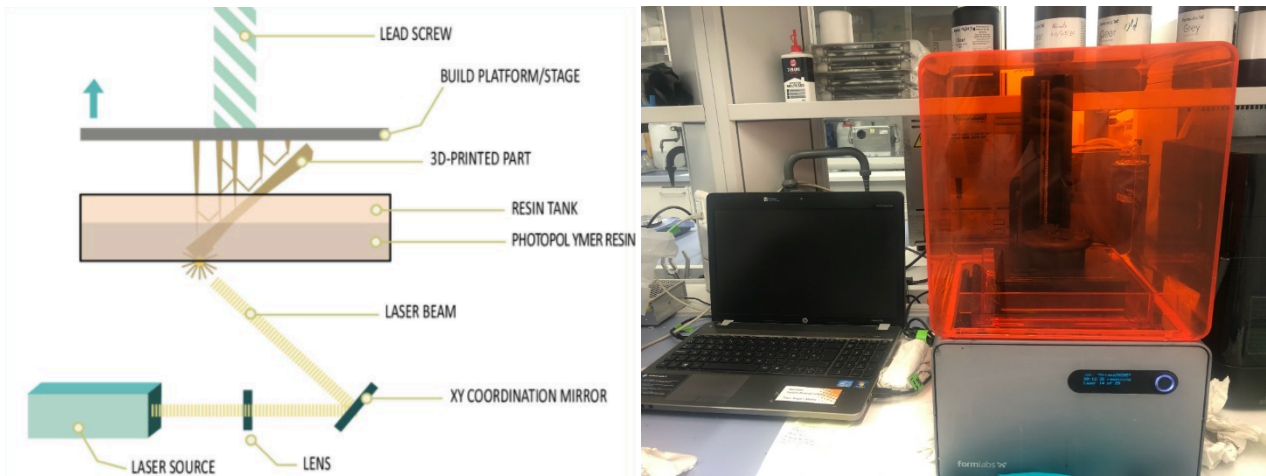


Figure 4.4 Scheme of a typical SL printing process. The laser acts on a photosensitive resin precursor placed in a tank taking advantage of a mirror and lens system (left). Image of the Form 1+ SL printer used in the manufacturing of the gold nanocomposites (right).

4.2.2. Fabrication via TP-DLW

Preliminary experiments were performed using an aqueous solution of PVA (18.06 mM) and HAuCl_4 (9.5 mg of tetrachloroauric acid tetrahydrate ($\text{HAuCl}_4 \cdot 3\text{H}_2\text{O}$)). The salt is stored in dark containers and away from light sources to ensure that it remains stable.

For the second set of experiments a powder of the gold precursor Tetrachloroauric (III) acid (HAuCl_4), purchased from Sigma-Aldrich and Milli-Q water (18.2 M Ω cm) are used to prepare the aqueous solution of Tetrachloroauric (III) acid trihydrate.

In the preliminary tests with PVA the drop is put on the substrate (**Figure 4.5**), then waited for one hour and half until full evaporation of water in the mixture before TP-DLW printing.

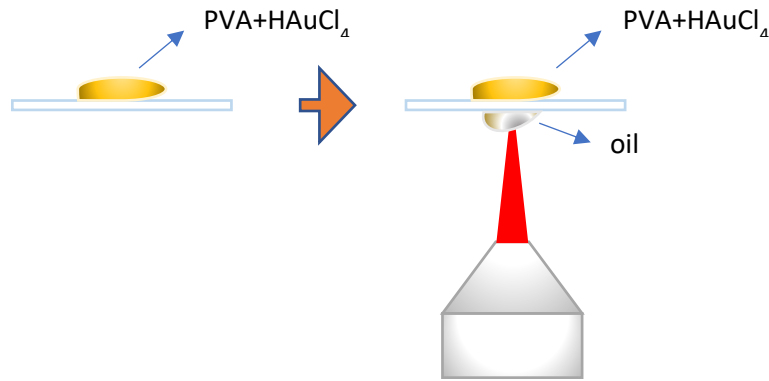


Figure 4.5 A sketch of the apparatus of the first test with a glass substrate, a drop of PVA+ HAuCl_4 solution and the Laser beam. A NIR femtosecond laser ($\lambda = 780 \text{ nm}$) with the objective working in oil immersion is used.

The same test will be repeated on a silicon substrate. But in this case a creation of a cell is necessary. We need a glass as interface between the objective and the gold precursor and so we created a sample with glass and silicon (**Figure 4.6**) where a thickness (max $10 \mu\text{m}$) between is created with two stripes of mylar, or other surface coupling agent like silica-microspheres ($5 \mu\text{m}$) or DMOAP (Dimethyloctadecyl[3-(trimethoxysilyl)propyl]ammonium chloride). The gold precursor is infiltrated by capillarity between the two layers. Since the total thickness of the sample is larger than the case of only glass substrate we have to be careful and to monitor the working distance during the approach to the sample in the printing process.

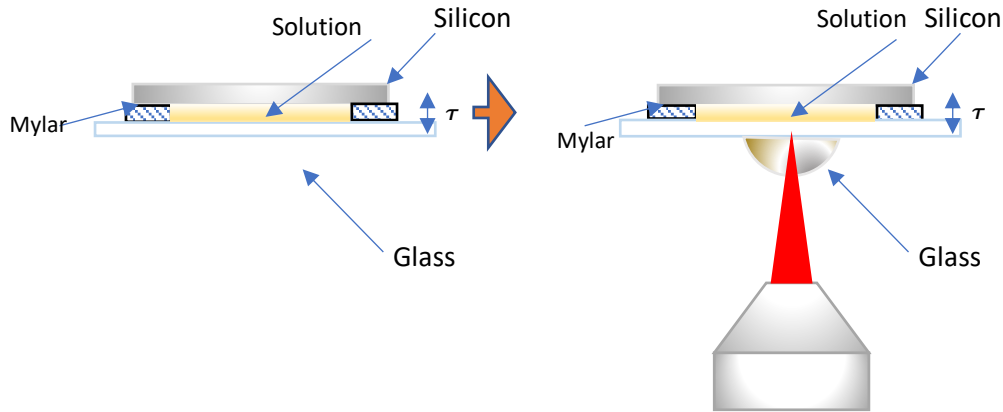


Figure 4.6 A sketch of the apparatus of the second test with a silicon substrate, a drop of PVA+HAuCl₄ solution is infiltrated for capillarity in the cell of 10 μm of thickness given by two stripes of mylar and the Laser beam. NIR femtosecond laser ($\lambda = 780 \text{ nm}$) with the objective working in oil immersion is used.

With this method the focus figure of the laser beam is reduced due to the thickness of the cell and it must pass several layers before reaching the silicon substrate, so it is necessary a laser power up to 100 of percentage intensity ($I_{LB} \propto \sigma^2$ where σ is the cross section).

It is for this reason that we did an attempt to change the configuration: the objective working in air. In this way we can approach the sample directly without other interfaces in between.

For TP-DLW printing using an isinglass matrix, a thin film of isinglass was deposited by spin coating onto a silicon substrate using the FR10KPA Spin Coating System by CaLCtec. This was done after a stirring process (500 rpm at 40 °C) in order to get a hydrogel film of uniform thickness of about 3 μm (**Figure 4.7a**), considerably thicker than the diameter voxel size ($300 \text{ nm} < d < 1 \text{ μm}$). The coated substrate was subsequently immersed in a $10^{-2} \text{ M H AuCl}_4$ aqueous solution for 30 min to allow Au³⁺ diffusion into the hydrogel network (**Figure 4.7b**). Then, the substrate containing H AuCl₄ was extracted from the bath and then exposed to laser light source. Honeycomb-patterned dots and lines were fabricated as 2D structures by TP-DLW using the workstation Photonic Professional GT, Nanoscribe GmbH with a pulsed femtosecond NIR Ti-Sapphire laser source ($\lambda = 780 \text{ nm}$, pulse duration 100-200 fs, repetition rate = 80 MHz) connected to an inverted microscope (**Figure 4.7c**). The laser beam is focused on the sample through a 63x (N.A. 1.4) and a 25x (N.A. 1.1) objective in

air configuration. Micro/nano structures were formed by sweeping the laser beam in X-Y directions using a galvo-scanner with different speeds. In order to create manifold structures, the following parameters were tested: Laser power (LP) was ranged in all cases from 40 to 100 mW. The exposure time (ET) was ranged from 100 to 150 ms for honeycomb-patterned, isolated structures and a scan speed (SS) of 200 $\mu\text{m/s}$ was used in the case of printed lines. After the exposure to the TP-DLW laser, the substrate is immediately immersed in a bath of deionized water that removes the metal precursor ions from the hydrogel film (**Figure 4.7d**).

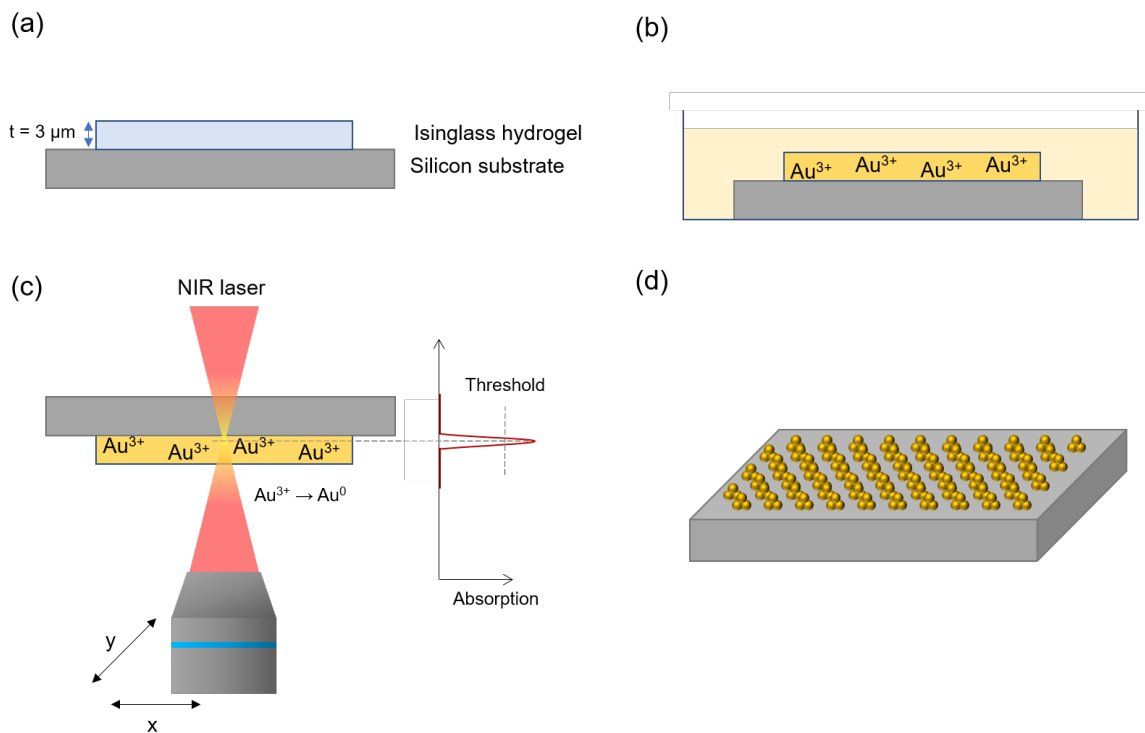


Figure 4.7 Scheme depicting the nanofabrication of AuNSs via TP-DLW process: (a) a hydrogel layer is deposited on the top of a silicon substrate; (b) immersion of the hydrogel film in a HAuCl_4 solution for 30 minutes to allow Au^{3+} diffusion into the hydrogel matrix; (c) photoreduction of Au^{3+} into Au^0 via TP-DLW using a NIR laser taking advantage of the TPA process; (d) a washing step with deionized water stops the created AuNPs growth; a second washing step with warm water removes the hydrogel film, leaving the AuNSs attached to the silicon substrate.

After the formation of the AuNSs, they may keep growing until the hydrogel film is washed with deionized water. In order to tune the size of the AuNSs, a second immersion in a 10^{-2} M HAuCl_4 solution is done. This process allows the growth of the AuNSs onto the substrate with the reduction

of Au^{3+} into Au^0 , as depicted in **Figure 4.8**. After 30 min, a bath in deionized water stops the growth process.

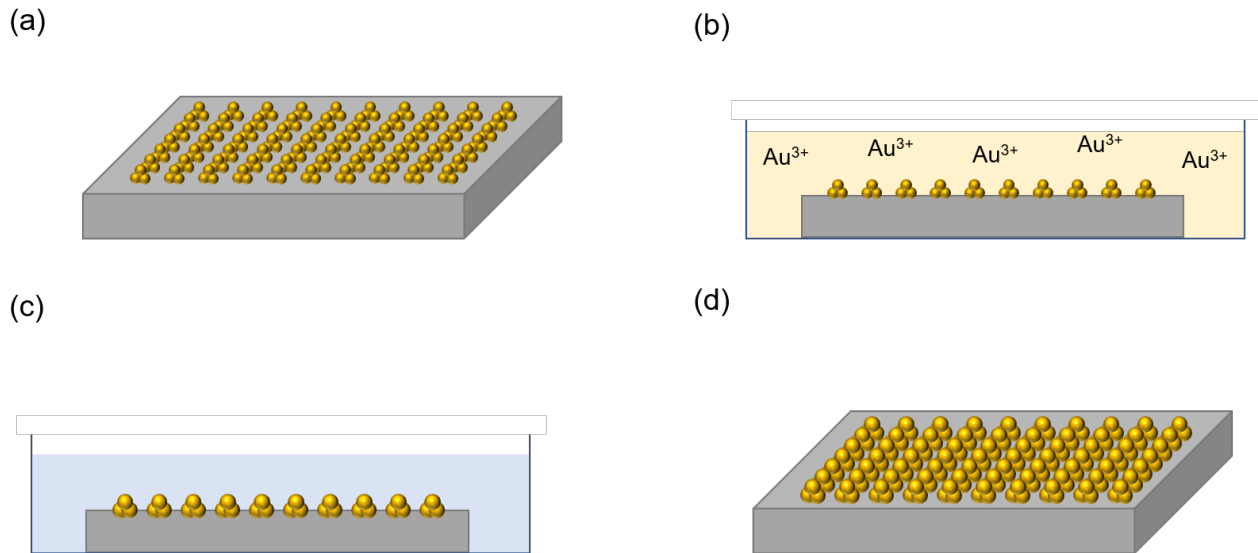


Figure 4.8 Scheme depicting the nucleation and the growth of the AuNSs created. The first step is (a) the creation via TP-DLW of the AuNSs on the silicon substrate; during the lag between the exposure and the first washing step with deionized water to remove the hydrogel, the autocatalytic growth of the nanoparticles goes on; (b) during the lag between the exposure and the washing steps the growth of the nanoparticles goes on then, in order to tune the size of the AuNSs, a second immersion in a 10^{-2} M HAuCl_4 solution is done allowing the growth of the AuNSs through the migration of the chloroauric ions towards the nanostructures and the reduction of Au^{3+} into Au^0 ; (c) a subsequent bath in deionized water stops the growth; (d) the AuNPs have grown in a controlled way only where the AuNSs are lodged.

4.2.3. Fabrication via TP-DLW on SiO_2 NWs substrate

Silica NWs on Si wafer were produced by thermal annealing of Si NWs grown by plasma enhanced chemical vapor deposition (PECVD). First, to induce the Si NW growth, a 2 nm thick Au film was evaporated onto the Si substrate prior to growth. The growth was performed using pure SiH_4 as precursor at a total pressure of 1 Torr and substrate temperature of 350 °C. A 13.56 MHz radiofrequency with power density of 50 mW/cm^2 was used to create the plasma. In these growth conditions tens of μm long Si NWs with average diameter of 150–200 nm at the bottom and tapered shape are obtained. After the growth, the Si NWs were thermally oxidized to form SiO_2 (silica) NWs via a thermal treatment in a convection oven (controlled O_2 atmosphere) at 980 °C for 8 h.

The TP-DLW processes were performed with a Photonic Professional GT system, from Nanoscribe GmbH, based on an inverted microscope, using a 150 mW-pulsed Erbium laser with $\lambda = 780$ nm and pulse length between 100 and 200 fs with a 100 MHz repetition rate.

The silicon chip is wet with a drop of IP-S resist on the NWs side and put on the inverted microscope stage. A 25x objective with numerical aperture (N.A.) of 1.2 (Zeiss, Plan Apochromat) in immersion mode was used, according to the scheme of **Figure 4.9**.

A simple parallelepiped was designed 500 x 500 x 20 μm as sample and printed it in two different z-positions, namely: adherent at the interface with the Si wafer, and at a few microns above the substrate, anchored to the SiO₂ NWs only. In both cases, several samples (500 x 500 x 20 μm , 2000 x 2000 x 15 μm parallelepipeds) were printed as shown in **Figure 4.10**, both as fully solid objects and as simple shells.

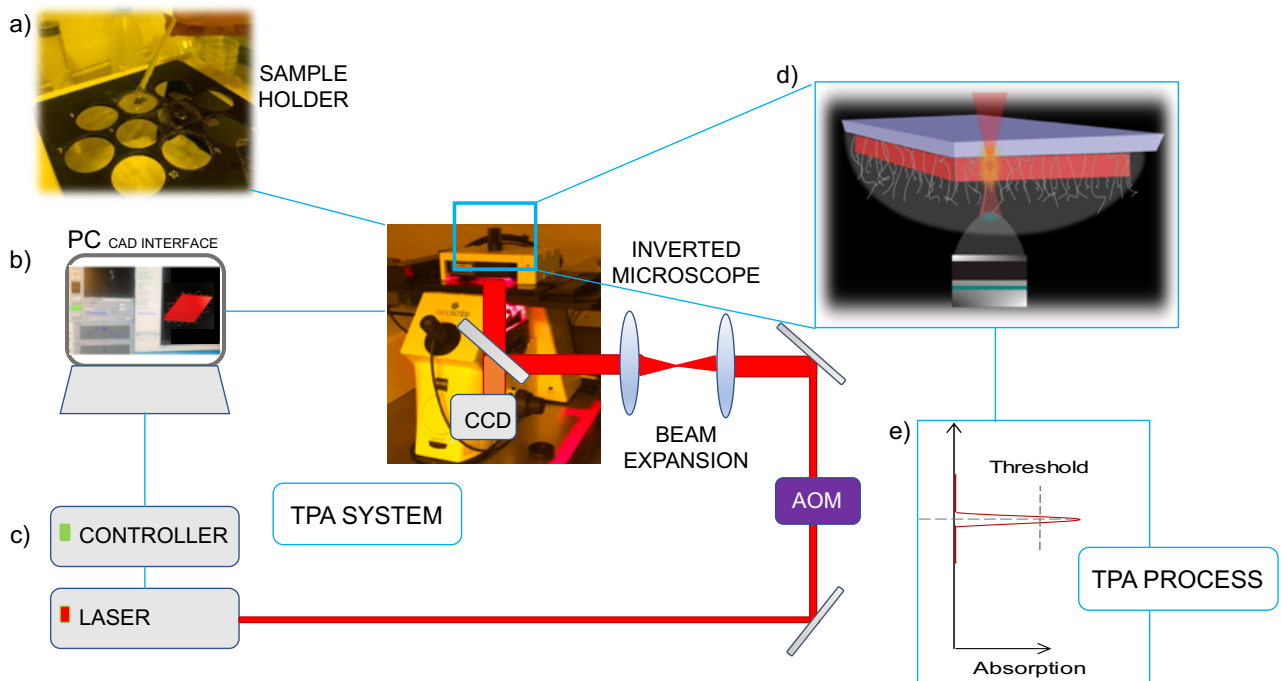


Figure 4.9 Set-up of the TP-DLW system. a) The Si chip, carrying the SiO₂NW carpet soaked with the IP-S photo-resin, is fixed on a glass coverslip and placed in the sample-holder of the inverted microscope with the SiO₂NWs facing the focusing lens; b) a 500x500x20 μm parallelepiped is designed through a CAD file c) with a P.C. connected to the TPA system: d) the polymerization is performed inside the voxel and through the carpet of SiO₂NWs, e) leveraging the TPA process.

It is possible to import the objects from image files, namely BMP, PNG, TIF, TIFF, JPG and JPEG files which are accepted for printing 2.5D topographies. Print jobs are produced and various tools can be used to tune printing parameters such as layer height or printing speed. Some programs permit the variation of geometrical features as the slicing distance and hatching distance (i.e. the horizontal layers and the parallel lines of the object), object splitting and angle stitching to optimize the times of printing and the strength of the structure. In analogy to this, the external part (shell) and the internal backbone (scaffold) are other parameters that can be tuned in order to optimize the final product. Moreover, depending on the AM technology used other parameters may also be tuned. For instance, scan speed, exposure time or light intensity for vat photopolymerization techniques or nozzle and platform temperatures for material extrusion technologies. The parameters can be customized, saved and re-used to print particular structures with high reproducibility.

After the exposure the samples are developed in PGMEA for 10 min to remove the excess of non-polymerized resist and then washed in IPA during 3 min in order to completely remove the PGMEA from the polymer.

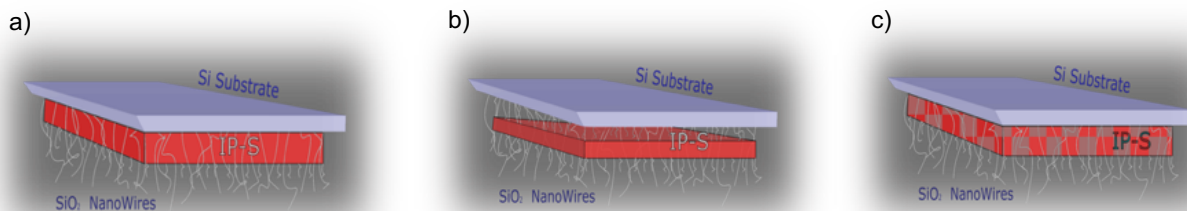


Figure 4.10 *Three different kind of structures are realized with the process protocol that grants considerable advantages in all the types: a) adhesive layer, for adherent structures; b) sacrificial layer, for detaching structures; c) only shell, for structures sustained by the Si O₂ NWs scaffold*

The polymerized and developed resist still contains an excess of SiO₂ NWs which can be degraded in a hydrofluoric (HF) buffer. The samples are immersed in an aqueous solution of 49% HF (85 ml of distilled H₂O, 10 ml of HCl and 5 ml of Buffered HF Solution) for 15-30 min. The etching progress was controlled at regular times.

4.3. Characterization

Characterization of all the nanocomposites and nanostructures has been done to describe the structure and the principal features of the new materials manufactured. Characterization on these composite materials to understand physical and chemical processes have been grouped in three different aspects to analyze and test the products from different angles and perspectives:

- a) A structural characterization to study the topography and the morphology of the nano-patterning fabricated as well as the distribution of the nano-additives in the polymeric matrix in the case of the nanocomposites using high resolution microscopy techniques.
- b) Optical characterization to study the properties like light absorption with potential applications in plasmonics or optoelectronics.

Mechanical characterization to study the elasticity and stiffness response to external stresses applied at the nanoscale.

4.3.1. Characterization of the topography and morphology

The structures of all the different nanocomposites and nanostructures manufactured, including gold nanocomposites via SL, AuNSs via TP-DLW and GFRP via TP-DLW were characterized via scanning electron microscopy (SEM). SEM measurements were performed using a FEI Nova NanoSEM 450 microscope equipped with a field-emission gun for high- resolution analyses, with a concentric annular detector, capable to render Z-contrast imaging and with a FEI Quanta FEG 400 F7 eSEM (Eindhoven, The Netherlands) electron microscope.

Further characterization of gold nanostructures via TP-DLW was carried out via transmission electron microscopy (TEM) analyses. For this purpose, electron transparent lamellae (ca. 100 nm thickness) were prepared in a Thermo Scientific Scios 2 DualBeam focused ion beam scanning electron microscopy (FIB-SEM). A Pt layer was first deposited to protect the sample in the area of interest during the milling process. Then, the lamella was extracted and thinned by Ga ions at 30 kV.

The final thinning and cleaning were done at 5 kV. FIB cross-section samples were analyzed by TEM and STEM (including high-resolution TEM, HRTEM; high-angle annular dark field STEM, HAADF-STEM and energy dispersive X-ray spectroscopy, EDX). Measurements were carried out using a Jeol J2100 provided with a LaB6 filament operated at 200kV, and a FEI TALOS F200X equipped with a field emission gun (FEG) source at 200 kV, combining high resolution (S)TEM imaging with EDX signal detection. The morphology and size of the AuNSs and AuNPs analysis was done using ImageJ software.

The GFRP nanocomposites were further characterized using an atomic force microscopy (AFM) Bruker Catalyst + Multimode 8 (Fluid and environmental cell, Quantitative nano-Mechanics module, practically all working modes available). AFM was used in a very high-resolution type of scanning probe microscopy (SPM), with demonstrated resolution on the order of fractions of a nanometer and it takes advantage from interaction (Van der Waals force) between the tips and the specimen surface.

4.3.2. Characterization of the optical properties

The optical properties of the gold nanocomposites fabricated via SL were investigated by UV-Vis spectroscopy. For this purpose, the absorbance of the nanocomposites was investigated in the range of 200 – 900 nm using a Varian Cary 50 Conc UV-Vis spectrophotometer. Samples analyzed include the preliminary tests carried out inside the UV-Vis macro-cuvettes and the sandwich samples as well as the monolayers and parallelepipeds printed via SL.

4.3.3. Characterization of the mechanical properties

The mechanical characterization for the glass polymer fiber reinforced nanocomposites was carried out on the nano-scale by instrumented nano-indentation method with the aim of measuring the nano-hardness and elastic moduli. The tests were executed by a nano-indentation platform (NHT, Anton Paar) by using a sphero-conical tip, with a radius of 20 μm . The spherical tip was adopted instead of more common sharp tips (such as Berkovich, Vickers, etc.) to limit the maximum penetration depth,

due to the reduced thickness of the nanocomposite. A typical force-displacement curve obtained from instrumented indentation is illustrated in **Figure 4.11**. The indentation curve ($P - h$), in fact, can be used to calculate the nano-hardness and Young's modulus.

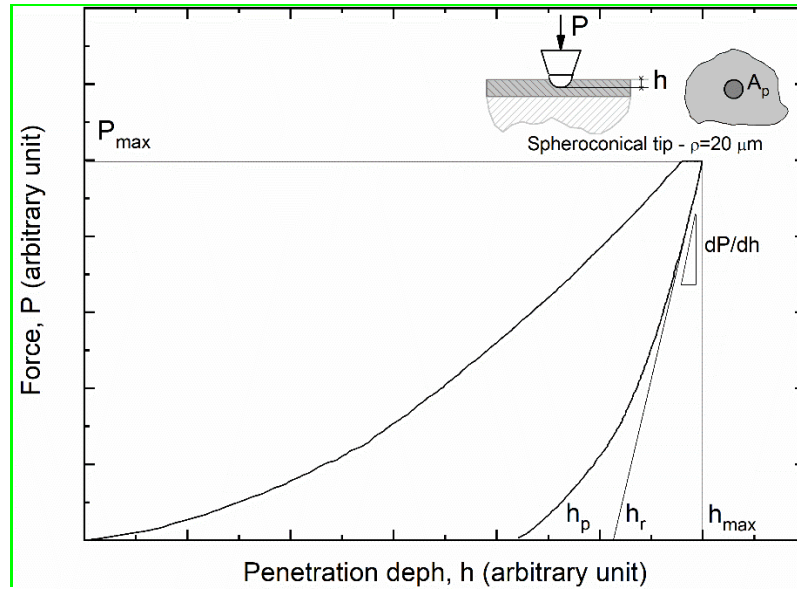


Figure 4.11 *Typical nano indentation curve force (P) vs indentation depth (h) together with significant indentation parameters used to calculate the indentation nano hardness (H_{IT}) and Young's modulus (E_r)*

The nano-hardness (H_{IT}) can be directly measured from the indentation curve as reported in the following equation:

$$H_{IT} = \frac{P_{max}}{A_p(h_p)} \quad (1)$$

where A_p is the projected area after indentation, that is obtained geometrically as a function of the residual depth h_p . The reduced Young's modulus (E_r) can be calculated from the contact stiffness ($S = dP / dh$), that is the slope of the initial path of the unloading curve (**Figure 4.11**), according to the standard ISO 14577-1 (2002), based on the Oliver and Pharr (1992) method:

$$E_r = \frac{1}{2} \sqrt{\frac{\pi}{A_p(h_p)}} S \quad (2)$$

where dP / dh is calculated in the range $0.4-0.98 P_{max}$. The indentation modulus of the material, E_{IT} , can be obtained from E_r by considering the elastic properties of the indenter tip ($E_i=1140$ GPa and $\nu_i=0.07$ for diamond):

$$E_{IT} = (1 - \nu^2) \left(\frac{1}{E_r} - \frac{1-\nu_i^2}{E_i} \right)^{-1} \quad (3)$$

Due to the average thickness of the NWs layer over the fabrication substrate, that is about 7-8 μm a proper indentation load should be chosen in order to ensure that the plastic and elastic volume, involved during the test, is not affected by edge effects. With this purpose, an indentation matrix was performed on the sample in which the indentation load was varied in the range 0.5 mN-10 mN. This was made to avoid possible estimation errors of both Young's modulus and material hardness due to load/size effects as well as to keep the maximum indentation depth (h_{max}) below 10% of the composite thickness.

5. Additive Manufacturing of AuNPs composites via SL

In this chapter, we introduce SL as a technique used to fabricate nanocomposites containing gold nanoparticles. It represents a strategy applied in order to improve or tune the optical, electronic and plasmonic properties of the new composites and to produce solid structured objects rich in metallic nanoparticles, homogeneously dispersed within. A fine tuning of the metallic precursor concentration and a control on the time and temperature are also performed to allow the best conditions of the polymerization of different 3D structures, hence to study the best technique of post-treatment. In fact, after the 3D printing process, the green sample obtained can be treated either with temperature and/or with UV light in order to obtain AuNPs with controlled size and morphology.

Before proceeding with the SL of the nanocomposites, preliminary tests are performed using small amounts of material (the so-called “droplet samples” and “sandwich samples”, see **Chapter 4** for more details). This allows to find an adequate range of concentrations that can be further used in the SL apparatus for the production of nanocomposites containing AuNPs. First, an optical characterization is done leveraging the macroscopic properties of the objects like color and UV-vis spectra. Then, complementary analysis with SEM are done to correlate these macroscopic properties with the nanostructure of the material manufactured. The physical processes behind this technology, the technology itself and the used materials and equipment are described in **Chapter 4**.

5.1. Preliminary tests

The preliminary tests are done to identify a range of concentrations that are suitable for SL printing using as few reagents as possible. It has to be noted that the tank of the SL apparatus needs to contain at least 50 mL of photosensitive resin for a proper printing. Instead, the preliminary tests need only few drops of solution or even smaller amounts which in any case are below 3 mL of resin precursor. These alternative tests avoid wasting material.

In particular, in the case of the gold precursor (which is rather expensive, around 160€/g) it implies saving hundreds of milligrams of gold precursor for each test if every experiment were to be conducted in the SL apparatus.

5.1.1. Study of the range of KAuCl_4 concentrations valid for SL

The first attempts are done simulating the SL machine conditions to reproduce the photopolymerization of the resin without using the SL 3D Printer. These tests were performed to identify a range of KAuCl_4 concentrations that allow successful UV-curing of the resin in similar conditions than in the SL apparatus. To obtain a homogeneous concentration of gold solution in the resin, a bath with sonication is done. This helps to dissolve the gold precursor in the resin, which does not occur immediately, since the resin is a very viscous liquid of organic nature. Hence, one of the first experiments is to identify the maximum amount of KAuCl_4 that can be successfully dissolved in the SL resin. These experiments were first carried out in disposable polystyrene UV-Vis macro-cuvettes because later they can directly be placed in the spectrophotometer for testing the optical properties of the material. For 1 wt% KAuCl_4 concentration and below (down to 0.01 wt%) 15 min of sonication is enough to dissolve the gold precursor in the resin, while at least 20 min are necessary for resin precursor containing 2 wt% KAuCl_4 because the solution becomes more viscous and KAuCl_4 tends to sediment at the bottom of the cuvette longer (Figure 5.1). Solutions containing above 2 wt% KAuCl_4 did not fully dissolve in the resin, so 2 wt% was set as the maximum amount of gold precursor that can be used.

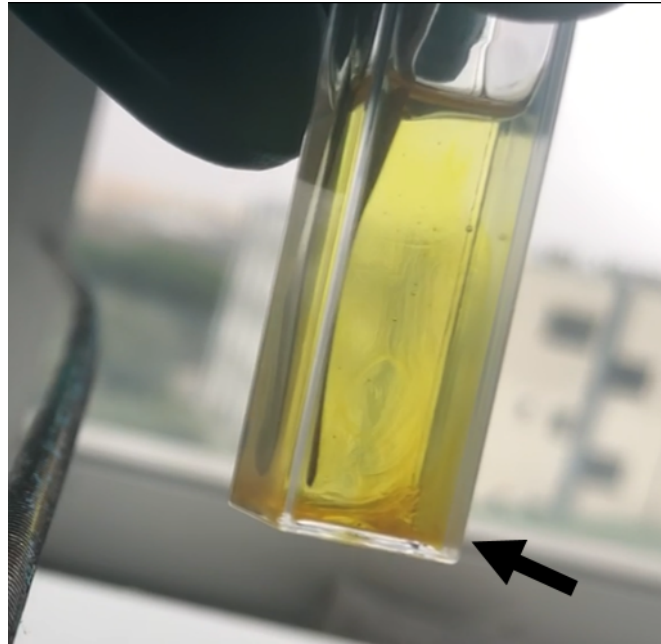


Figure 5.1 *UV-Vis macro-cuvette containing the SL resin and the gold precursor KAuCl_4 . Black arrow points at the region where the KAuCl_4 is not fully dissolved in the resin. Sonication for at least 30 min is needed to ensure a homogeneous mixture.*

It was established a sonication time of 30 min for all the concentrations. A prolonged duration of sonication will ensure to have a homogeneous solution longer. This time was also found adequate to prevent the thermal effects on the composite derived of long sonication times, which can affect the resin photo-initiator before the polymerization reaction. At the end of the sonication process, all the mixtures ranging from 0.01 to 2 wt% KAuCl_4 look well homogeneous, with a transparent, homogeneous yellow color, as shown in Figure 5.2a).

A UV-curing test using 1-3 mL of resin containing 0.01 - 2 wt% KAuCl_4 is done using the FCure UV chamber using the polystyrene UV-Vis macro-cuvettes as container. These tests were conducted at room temperature in intervals of 10 min up to 60 min. This was done to simulate the exposure conditions of the SL laser and to identify the maximum amount of KAuCl_4 that allows proper polymerization of the resin with UV light. Figure 5.2b shows an illustrative example of the resin with different amounts of gold precursor after UV-curing for 30 min. It was observed that higher concentrations needed longer UV-curing times. In particular, for 1wt% and 2 wt% KAuCl_4 the resin

did not fully polymerize, having a partially solid product with some uncured liquid remaining in the center of the cuvette. Longer UV-curing times, up to 60 min did not enhance the curing of the resin in the case of 2 wt% KAuCl₄. Hence, it was identified this concentration as the first threshold, i.e. the upper limit which inhibits the polymerization of the resin. This is probably because this amount of gold precursor absorbs and/or scatters a sufficient amount of UV light, hindering the proper curing of the resin.

Moreover, the influence of the temperature in the photopolymerization of the resin was studied. Different temperatures ranging from room temperature (25 °C) to 80 °C in intervals of 10 °C were tested. It was observed that higher temperatures in the UV chamber increase the polymerization time and the samples which typically polymerize after 10 min need at least 30 min when the UV-curing is done at 60 °C. As a result, it was concluded that photopolymerization of the resin is not enhanced by increasing the temperature and UV-curing procedure was set back to room temperature.

Hence, resins containing 0.1, 0.5 and 1 wt% KAuCl₄ were successfully cured after 60 min of UV radiation (Figure 5.3). However, the morphology of the resin contained within the macro-cuvette does not remain in a homogeneous shape after UV-curing, presenting some bubbles and inhomogeneities in the center. This effect happens regardless of the concentration of KAuCl₄ and can be attributed to the shrinkage of the resin during the curing process. In any case, the color and transparency of these materials does not vary after the UV-curing, which seems to indicate that the gold precursor is stable during this treatment in this range of concentrations. Thus, this range of concentrations was chosen as the optimal and they will be studied in further detail.

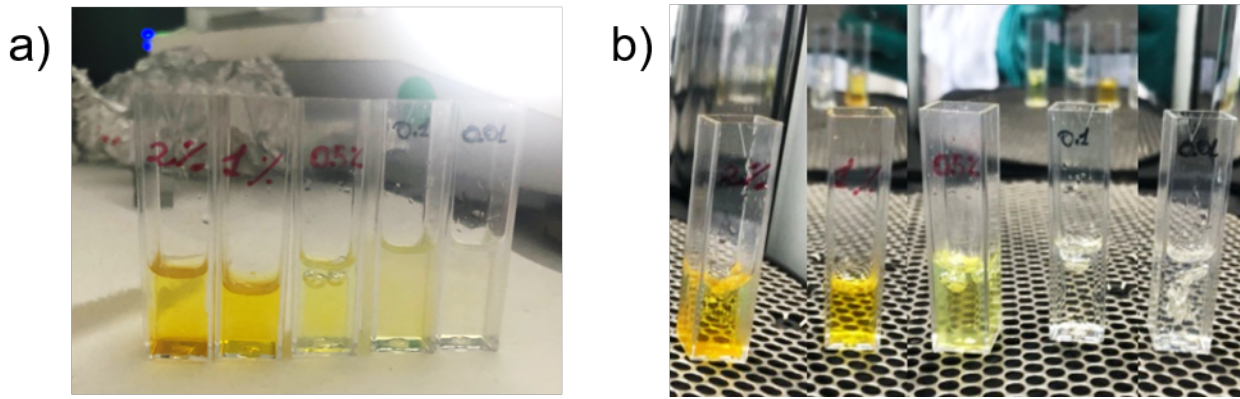


Figure 5.2 Macro-cuvettes containing the full range of concentrations studied (0.01 wt%, 0.1 wt%, 0.5 wt%, 1 wt% and 2 wt% KAuCl_4) a) before and b) after UV-curing for 30 min. Samples with KAuCl_4 concentrations below 0.5% wt are properly cured, while 1 wt% and 2 wt% KAuCl_4 are not completely polymerized, in particular in the center of the cuvette.

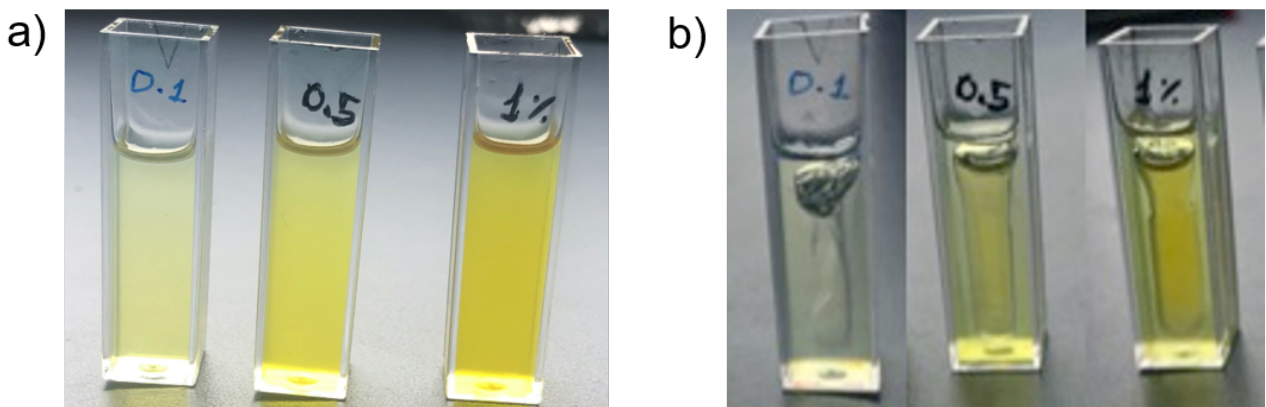


Figure 5.3 Macro-cuvettes containing the full range of concentrations studied (0.01 wt%, 0.1 wt%, 0.5 wt%, 1 wt% and 2 wt% KAuCl_4) a) before and b) after UV-curing for 60 min. In these conditions, samples with 1 wt% KAuCl_4 were successfully cured. Although all the samples are solid after curing, some irregularities are observed due to the contraction of the resin during the photopolymerization.

Then, a thermal treatment at 170 °C was done onto the cured resin inside these cuvettes to reduce the gold precursor into AuNPs^[1-3]. However, the polystyrene cuvettes did not resist this thermal treatment and were deformed within a few seconds after being introduced in the muffle oven. This can be simply explained because the glass transition temperature of polystyrene is 100 °C, meaning that any thermal treatment above this temperature cannot be applied when using these cuvettes.

In any case, interestingly, the resin inside the cuvettes underwent a color change from yellow to dark pink after being introduced in the muffle oven. As it is shown in **Figure 5.4**, some pink shades can be observed in the resins containing 0.1 and 0.5 wt% KAuCl_4 , while large areas with dark red color are identified in the resins with 1 wt% KAuCl_4 . This is a first evidence that this thermal treatment induces the formation of AuNPs.

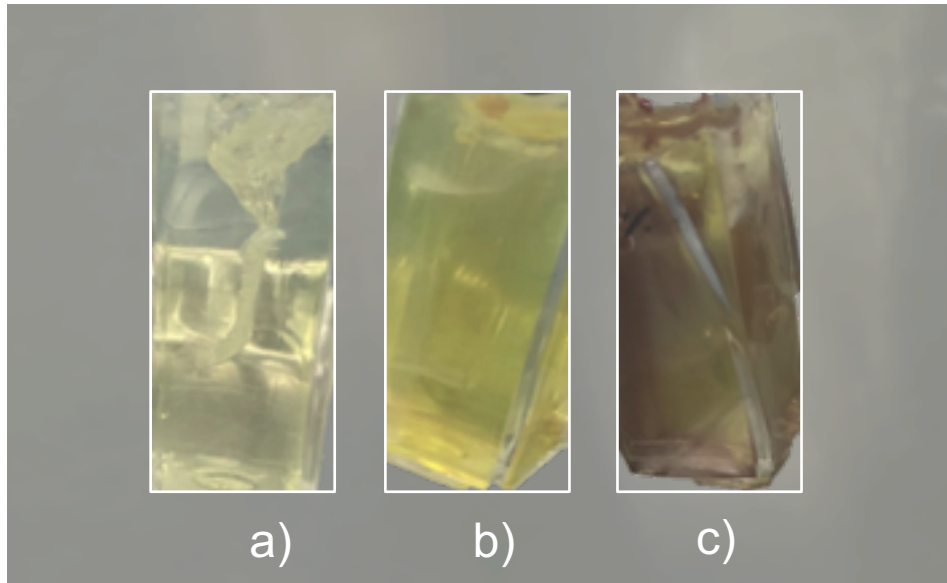


Figure 5.4 *Cross-sections of samples containing a) 0.1 wt%; b) 0.5 wt% and c) 1 wt% KAuCl_4 after the thermal treatment in the muffle oven in the cuvettes. In a) and b) some pink shades can be observed while in c) regions of red color are evident.*

As previously observed, polystyrene macro-cuvettes are not optimal substrates, since the thermal treatments above 100 °C cannot be done and the formation of the bubbles during the curing process does not allow measuring properly the optical properties of the materials via UV-Vis spectroscopy. As an alternative, the “sandwich samples” and “droplet samples” are proposed. The sandwich samples will allow to have a thin layer of nanocomposite precursor that can be directly measured by UV-Vis spectroscopy and the droplet samples will allow the study of the morphology of the nanocomposites via electron microscopy techniques.

5.1.2. Influence of UV and thermal treatments in the formation of AuNPs

The “Sandwiches tests” (**Figure 5.5 - Figure 5.6**) are an alternative approach in which one small amount of resin (which may contain KAuCl_4 or not) is placed between two glass coverslips so one thin layer of comparable dimensions to one SL layer (20 – 200 μm) is formed. These samples are expected to be used in UV-Vis analysis to correlate the change of color from yellow (typical from the Au^{3+} cations) to the characteristic color of the AuNPs (ranging from red to blue depending on the particle size and morphology) after reduction. The aim of these experiments is to find the best combination of UV and thermal treatments that produce AuNPs in a more optimized way.

Four different alternatives with two subsequent treatments were tested. In each alternative, the aim is to polymerize the resin in the first treatment and to reduce the gold precursor into AuNPs in the second treatment. For comparative purposes, all of these treatments are done for 1 h. The four alternatives include: 1) Curing with UV light and then a combination of UV and thermal treatment at 80 °C [**UV + (UV + T)**]; 2) Curing with UV light and then a thermal treatment at 170 °C [**UV + T**]; 3) one single step with combined with UV and temperature at 80 °C. In this case the aim is to study the possibility of curing the resin while the gold precursor is photo-reduced into AuNPs in one single step [**(UV + T)**]; and 4) a control in absence of UV light by applying two consecutive thermal treatments: first at 80 °C and then at 170 °C [**T + T**]. A summary of all these treatments can be found in **Table 4.1** in the **Chapter 4**.

Based on the results obtained after curing the resin inside the macro-cuvettes, these alternatives are done for concentrations of 0.1, 0.5 and 1 wt% KAuCl_4 . Figure 5.5 shows the sandwich samples before any treatment. It can be observed that they look transparent, or even pale yellow in the case of 1 wt% KAuCl_4 samples. At these point all the samples with the same concentration look the same. Figure 5.6 show the same sandwich samples displayed in the same position but after all the UV and thermal treatments have been applied. Here, it can be observed that in some cases, the color of some of the samples has changed into a purple color with different intensities and shades of blue or red. It is true that some of these samples do not exhibit a uniform color along all the surface. The irregular shape

can be attributed to the disposition of the droplet before preparing the “sandwich”, which may not have been fully even. In any case, these samples look more homogeneous than in the case of the samples prepared in the cuvettes.

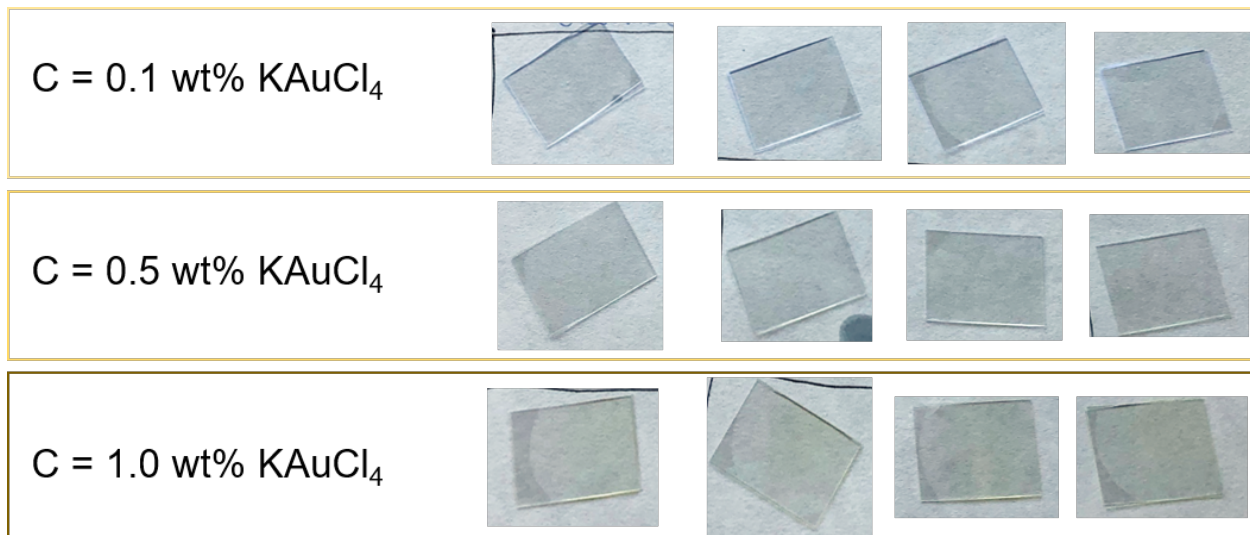


Figure 5.5 Sandwich samples containing 0.1 wt% KAuCl_4 (top row), 0.5 wt% KAuCl_4 (middle row) and 1 wt% KAuCl_4 (bottom row) before any UV or thermal treatment.

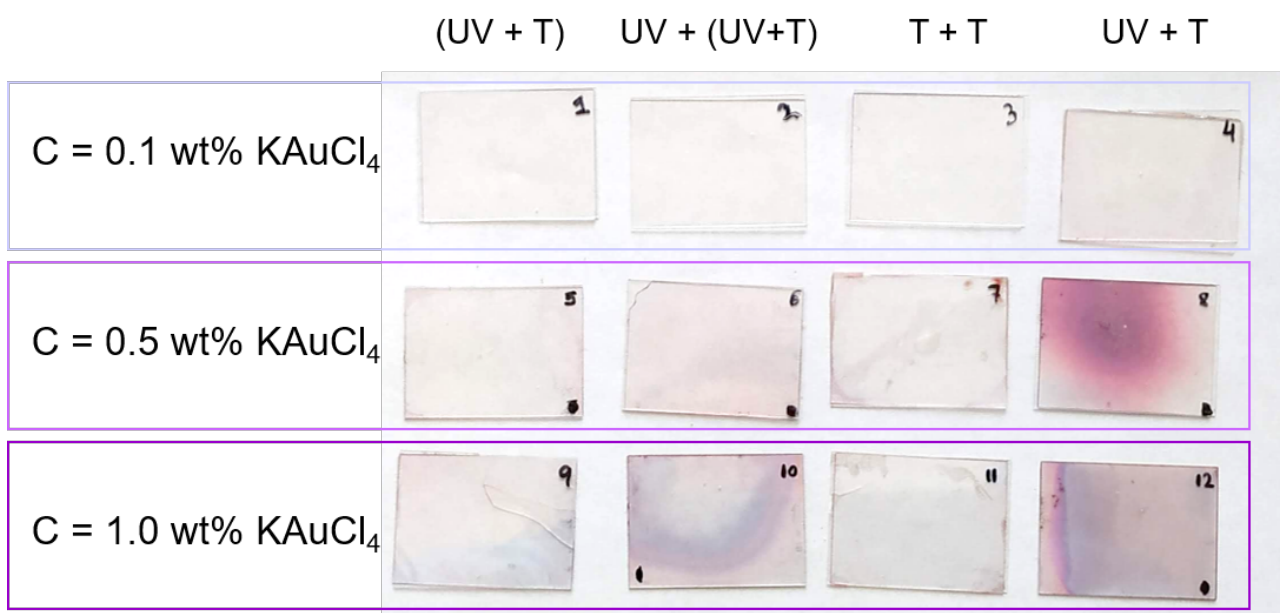


Figure 5.6 Sandwich samples containing 0.1 wt% KAuCl_4 (top row), 0.5 wt% KAuCl_4 (middle row) and 1 wt% KAuCl_4 (bottom row) after the four different UV and thermal treatments proposed.

Samples subjected to [UV + (UV+T)] and [UV + T] show significant changes in color for samples containing 0.5 and 1 wt% KAuCl₄, indicating that these two treatments are valid to achieve the reduction of the Au³⁺ cations into AuNPs. Samples containing 0.1 wt% KAuCl₄ do not show a significant change in color, at least observable by the naked eye. This can be either because the AuNPs are not being formed with such low concentration or because the amount of gold is too low so the sample is too thin to observe any change in color.

For these two treatments, changes in color were already observed after only 10 min, especially for samples containing high concentrations. However, to ensure that all the samples are comparable, all samples were treated for 60 min. Also, different temperatures of the muffle in the [UV + T] treatment were studied. The initial temperature used in this alternative was 80 °C, so this treatment could be directly compared with [UV + (UV + T)]. However, in these conditions no change in color was observed. This was the first evidence that the combination proposed in [UV + T] seems to have an influence in the reduction of Au⁺³ into AuNPs. Then, an increase of the muffle temperature in steps of 10 - 20 °C was done until it was noticed that around 170 °C the samples underwent a change in color. Finally, the upper thermal limit was set to 200 °C, since above this temperature, the resin started to degrade.

The [(UV + T)] and [T + T] treatments did not show any relevant changes in color. [(UV + T)] suggests that formation of AuNPs does not happen during the photopolymerization of the resin at either room temperature or 80 °C. This experiment can be taken as a control to indicate that the photopolymerization of the resin and the photoreduction of the gold precursor must be separated and, therefore, tuned individually. In the case of the [T + T] treatment, the color of the sample changed from yellow to red but the resin was not fully solidified, which evidences that an increment in temperature allows the thermal reduction of Au⁺³ but it is not enough for the polymerization of the resin. This complements the previous results observed, where the bare UV-curing does not allow the photoreduction of Au⁺³, at least at room temperature. In summary, we concluded that a UV-curing

and then a thermal treatment is necessary to obtain the formation of AuNPs in these polymeric materials.

A more in detail analysis of the color of the sandwich samples is done by UV-Vis spectroscopy. The **Figure 5.7** shows the spectra of all the sandwich samples prepared. The presence of AuNPs can be confirmed by the presence of a local maximum in at 500-600 nm, which corresponds to the plasmon of the AuNPs. This maximum can also provide information of the size and morphology of the AuNPs^[4,5]. It can also be observed some peaks at 365, 385 and 405 nm in some of these graphs (it is particularly clear in Figure 5.7a)), which correspond to the photo-initiator of the resin. These peaks are not expected to interfere with the AuNPs plasmons and have not been taken in account in the evaluation of the optical properties.

In good agreement with what we observed in Figure 5.6, the samples subjected to treatments [(UV + T)] and [T + T] do not absorb any visible light, indicating that no AuNPs have been formed. Samples treated with [UV + (UV+T)] exhibit a certain absorption in the visible range, with a shoulder starting around 500 nm for samples containing 0.5 and 1 wt% KAuCl₄. In both cases, the absorbance values are below 0.1, which indicates that this treatment may reduce the gold precursor into AuNPs, but at a very slow rate. Moreover, since the peak observed does not possess a Gaussian distribution, the AuNPs formed probably do not possess a homogeneous distribution in size and have different morphologies. In the case of samples that underwent the [UV + T] treatment, the UV-vis spectra show a peak in all the range of concentrations studied (it is even formed for 0.1 wt% KAuCl₄ although it is very subtle, with a maximum absorbance of 0.02). This peak is particularly interesting in the case of 0.5 wt% KAuCl₄, since it reaches a maximum absorbance around 0.4, indicating that for this concentration the amount of AuNPs produced is higher than in any of the other cases studied. Moreover, this peak exhibits a well-defined, Gaussian shape, which may suggest that the AuNPs sizes are quite monodisperse^[6].

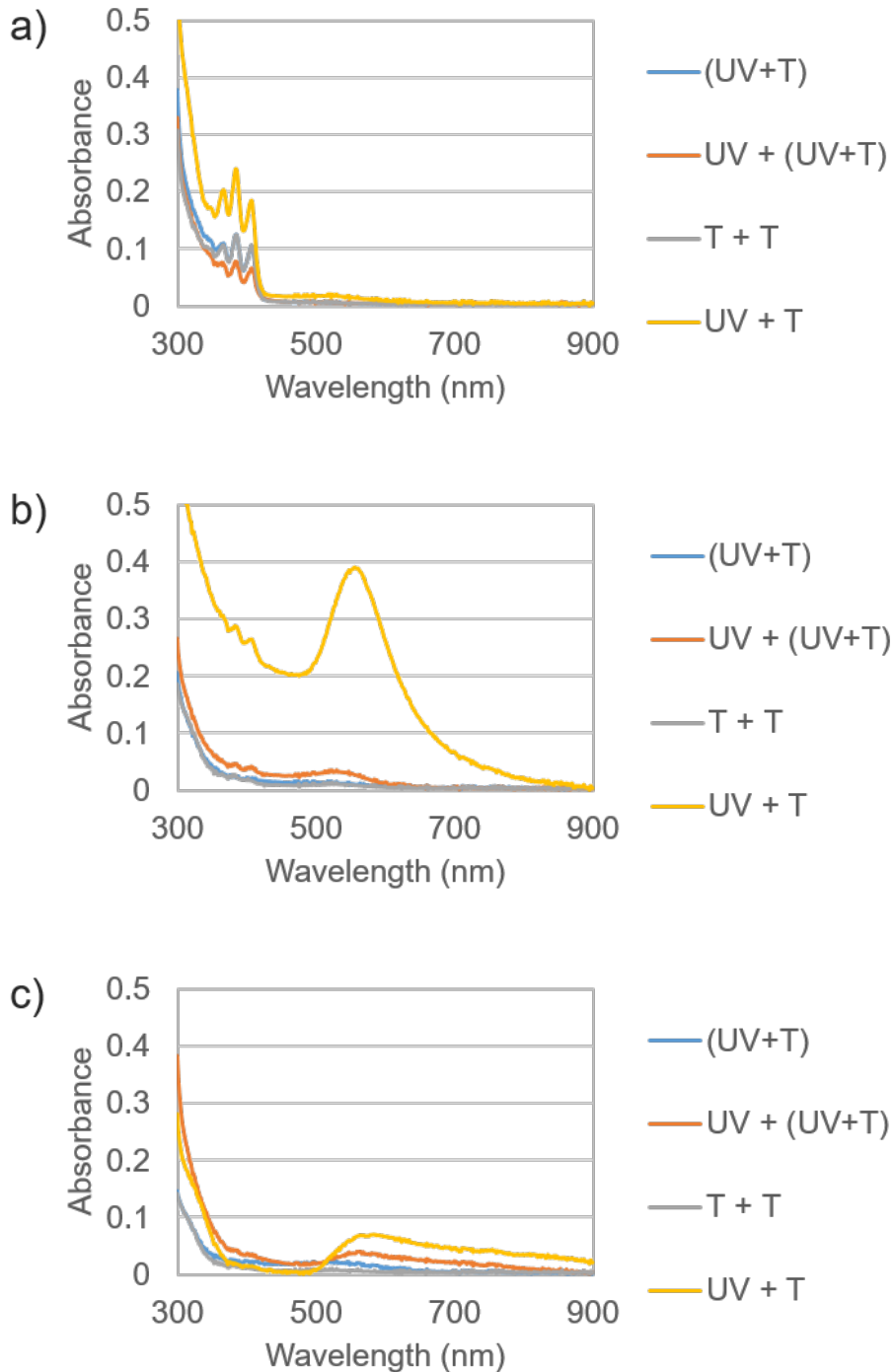


Figure 5.7 *UV-Vis spectra of sandwich samples after the different UV and thermal treatments for nanocomposites containing a) 0.1 wt%, b) 0.5 wt% and c) 1 wt% KAuCl₄.*

The position of the local maximum corresponding with the AuNPs plasmon was studied as a function of the KAuCl₄ concentration in the resin, as illustrated in **Figure 5.8**. This graph shows interestingly, that the maximum is shifted with the initial concentration of gold precursor, following a linear trend.

Assuming that these AuNPs are spherical and are composed solely of gold, the expected sizes for these AuNPs are 15, 82 and 120 nm for precursor concentrations of 0.1, 0.5 and 1 wt% KAuCl₄, respectively^[5,7]. These results suggest that the size of the AuNPs could be tuned by simply modifying the initial concentration of gold.

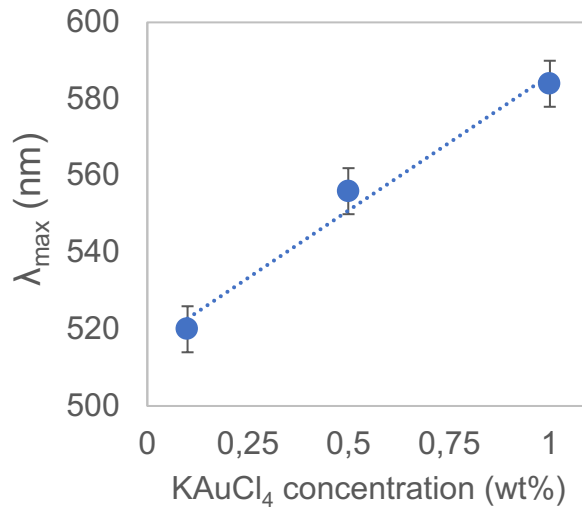


Figure 5.8 *Wavelength values corresponding to the maximum absorbance in the visible range (λ_{\max}) of the sandwich samples as a function of KAuCl₄. Values are extracted from the UV-Vis spectra after [UV + T].*

Complementary to the sandwich tests, the droplet tests are done for concentrations in the range of 0.01 - 2 wt% KAuCl₄. Compared to the samples prepared in the cuvettes, the droplets (a surface of around 5 mm of diameter) were fully cured after only 10 min for concentrations below 1 wt% KAuCl₄. Samples with 1 wt% KAuCl₄ require longer times, up to 60 min, to complete the curing process and concentrations above this value are not fully cured even when increasing the time above several hours. These results are in accordance with what it was observed in the preliminary tests done in the cuvettes.

As in the other tests, it can be seen in **Figure 5.9** that samples exhibit a yellow color before curing, which increases its intensity with the concentration. After the [UV + (UV + T)] thermal treatment, the droplets change from yellow to red while samples show a pale pink or purple color after

[UV + T] thermal treatment. In all cases, samples exhibit a high grade of transparency, indicating that the size of the formed AuNPs is expected to be below the range of visible wavelengths (400 nm), confirming that these results are in agreement with what it was observed in the UV-Vis spectra of the sandwich samples.

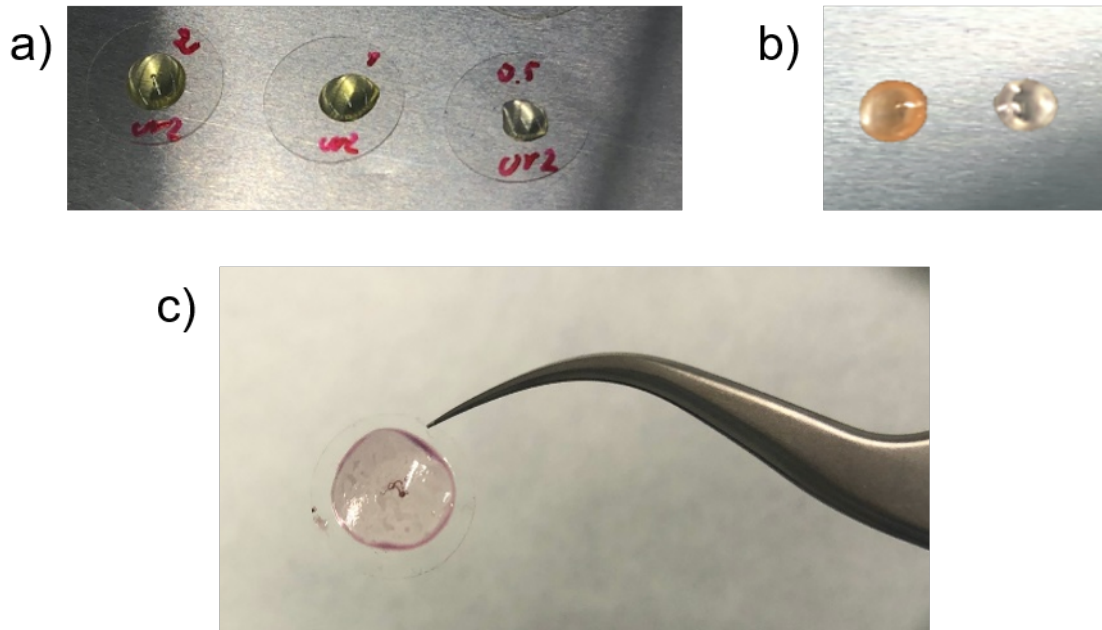


Figure 5.9 Droplet samples with a) 0.5 wt%, 1 wt% and 2 wt% KAuCl_4 after 1 h of UV-curing; b) 0.5 wt% and 1 wt% KAuCl_4 after [UV + (UV + T)] and c) 0.5 wt% KAuCl_4 after [UV + T].

The first interesting experimental evidence of plasmonic behavior in these samples is the difference in color when white light is directed onto them with different angles. In Figure 5.10 is shown a sample containing 1 wt % KAuCl_4 after [UV + T] treatment.

When the light falls into this sample transversally (reflected light) the sample looks red. When the orientation is perpendicular (transmitted light), it changes gradually its color into blue or purple. This behavior reflects an optical property of the AuNPs: when they are embedded in other materials and they reach the size of the wavelengths of visible light, a surface plasmon resonance effect takes place (an extraordinary famous example of this property is the ancient Lycurgus cup^[8]).

This effect is also observed in **Figure 5.9**, where samples appear to be red with reflected light (**Figure 5.9b**) while the sample appears to be light purple when the light is transmitted (**Figure 5.9c**).

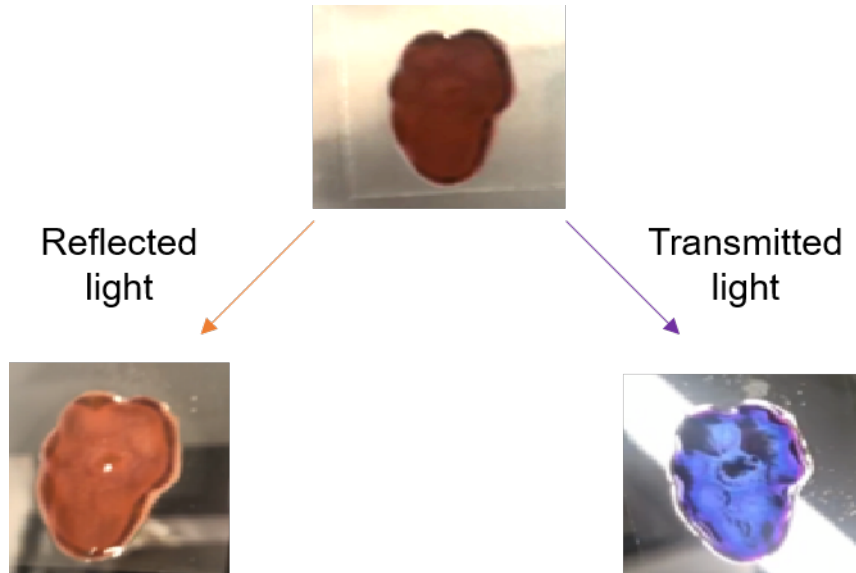


Figure 5.10 Sample containing 1 wt% KAuCl_4 after $[\text{UV} + \text{T}]$ treatment. Change of color is shown when the light orientation and angle varies. Sample looks red when white light is reflected and turns into blue or violet when light is transmitted.

Figure 5.11 shows two different droplet samples with 0.5 wt% KAuCl_4 after two different treatments. The UV-curing with a subsequent thermal treatment of 80°C for 1 h in the UV chamber $[\text{UV} + (\text{UV} + \text{T})]$ leads to homogeneous samples with color looking clear and transparent, with shadows of purple and light blue. The $[\text{UV} + \text{T}]$ treatment, however, brings a coloration of the samples leaning more towards dark pink or red.

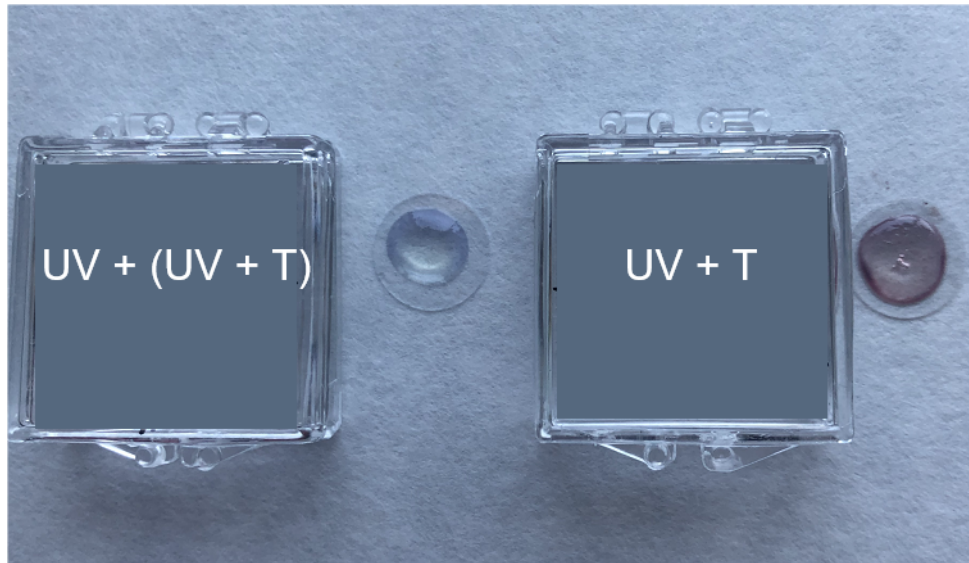


Figure 5.11 *Samples after the second treatment in [UV+(UV+T)] (left) and [UV + T] (right). The coloration is noticeably different.*

SEM experiments were conducted on the two samples shown in **Figure 5.11** to gain more information about the morphology, distribution and sizes of the AuNPs. These experiments were done on the surface of the nanocomposites using a concentric back-scattered electron (CBSE) detector without using any metallic sputtering with gold, palladium or other noble metals, as typically done since the CBSE detector provides signals with higher intensity in regions with high atomic number. In our case, this will provide a good contrast between C and O (main atoms in the resin) and Au^[9]. However, the samples are electrostatically charged inside the microscope when high magnifications are used, given the non-conductive nature of the resin. Even though Au is a great conductive material, the amount of AuNPs does not seem to be sufficient to reach the electric percolation limit and have a (semi)conductive sample.

As presented in **Figure 5.12**, SEM images of samples after [UV + (UV + T)] show a surface with AuNPs with different sizes, some of them grouped into larger clusters. On the other hand, samples after [UV + T] treatment, show a surface with AuNPs homogeneously distributed with a narrow distribution in size. A coarse analysis of the size of these AuNPs showed that they possess sizes comprised between 80 and 100 nm and they possess a platelet-like morphology.

These preliminary results are in agreement with what observed previously in the group when nanocomposites containing AuNPs with a polystyrene matrix^[10], where AuNPs in with morphologies of nanotriangles and nano-hexagons were observed for a similar range of concentrations. SEM images suggest that, even though both thermal treatments allow the reduction of Au³⁺ into AuNPs, [UV + T] leads to a more optimized nanocomposite material, with homogeneously distributed AuNPs with a well-defined size and morphology. This can also be correlated with the UV-Vis spectra of the sandwich samples, where it was observed a peak at 556 nm, characteristic of the plasmonic activity of AuNPs with a defined size at 80 nm^[11].

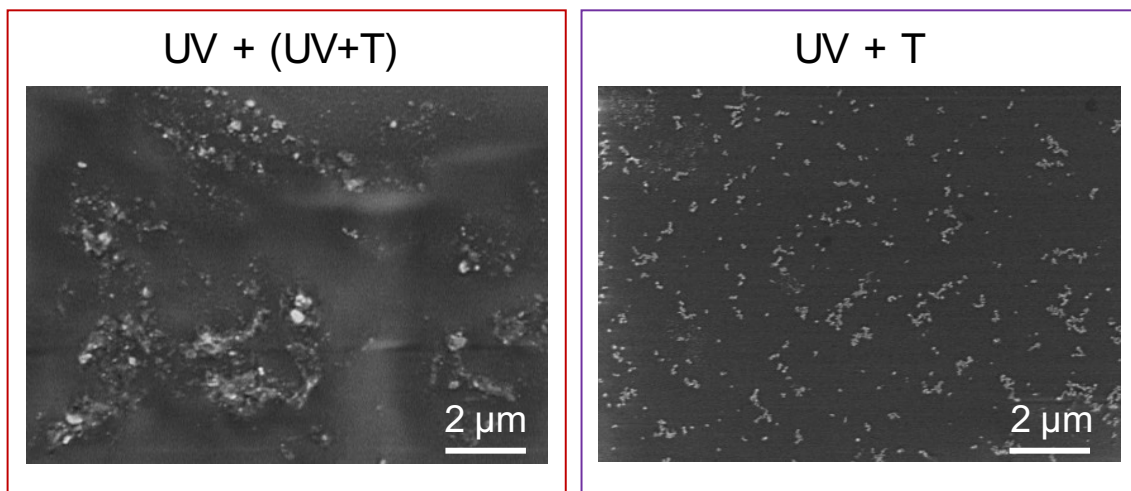


Figure 5.12 SEM micrographs of nanocomposites with 0.5 wt% KAuCl₄ after [UV + (UV + T)] (left) and after [UV + T] (right). CBSE detector show high contrast images where brighter regions correspond to elements with higher atomic number (i.e. Au).

5.2. SL Printing of 3D objects

Preliminary studies allowed to identify a range of suitable concentrations for the synthesis of gold nanocomposites via SL in the range of 0.1 – 0.5 wt% KAuCl₄. UV-Vis spectra showed that nanocomposites prepared with concentrations above 0.5 wt% do not exhibit plasmonic properties, while concentrations below 0.1 wt% may lead to a very small amount of AuNPs, which is less interesting for practical applications.

Various kinds of 3D objects, including monolayers, and parallelepipeds with 1 mm and 1 cm thickness were successfully printed via SL for samples containing 0.1 wt% KAuCl_4 . However, when concentration was increased up to 0.5 wt%, only monolayers could be printed. This concentration probably allows the polymerization of the first layer but absorbs enough laser light to hinder the polymerization of a second layer during the SL process. Hence, it was established 0.5 wt% KAuCl_4 as the upper threshold concentration for SL printing of these nanocomposites and additional tests using 0.05 and 0.3 wt% KAuCl_4 were performed to gain more information of the SL manufacturing process.

5.2.1. Influence of the UV and thermal treatment in 3D printed monolayers

In analogy with the preliminary tests, printed objects were subjected to different thermal treatments. In particular, the alternatives [UV + (UV+T)] and [UV + T] were chosen, since they are able to produce nanocomposites with AuNPs. After SL printing, the objects are already solid but the degree of cure of the resin is not 100% (green samples), even in absence of KAuCl_4 ^[12]. Therefore, it must be noted that in this case, the first UV treatment performed at room temperature for 1 h aims to fully polymerize the resin and provide the material with enhanced strength and stiffness (post-cured samples). As it was previously observed in the preliminary tests, this UV treatment is not expected to induce the reduction of Au^{3+} into AuNPs.

The first study was done onto monolayers of 0.2 mm thickness. First, as a control, SEM of green samples containing 0.1 and 0.3 wt% KAuCl_4 was done. As shown in the **Figure 5.13**, monolayers printed with 0.1 wt% KAuCl_4 do not show any change in color, which indicates that no AuNPs have been formed. SEM image shows some irregularities in the surface, but they can be attributed to the own roughness of the resin or small aggregates of the gold precursor that have precipitated during the SL process. For samples with 0.3 wt% KAuCl_4 some nanoparticles are observed. However, these nanoparticles are not likely to be AuNPs but crystals of the gold precursor instead, either in the form of KAuCl_4 or KCl . As we indicated after performing the SEM of the preliminary analysis, the AuNPs were obtained in the shape of nanotriangles or nano-hexagons, characteristic of thermally induced

AuNPs. Instead, the nanoparticles observed in **Figure 5.13c)** possess a squared/cubic shape, characteristic of the gold precursor^[10]. These crystals have a size below 1 μm and they may not be observable to the naked eye. Moreover, a change in color is not observed in these green samples. More in depth microscopy analysis including high resolution techniques would be required to ensure the nature of these crystals but they are beyond the scope of this thesis and they are proposed as future work.

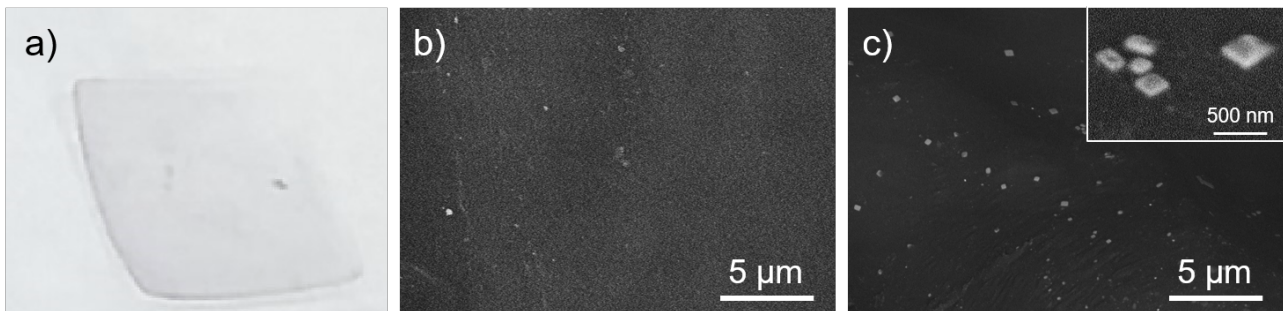


Figure 5.13 a) Digital picture and b) SEM micrograph of a monolayer with 0.1 wt% KAuCl_4 and 0.2 mm thickness printed by SL without any further treatment (green sample); c) SEM micrograph of a monolayer with 0.3 wt% KAuCl_4 and 0.2 mm thickness printed by SL without any further treatment (green sample). Inset in c) shows some KAuCl_4 cubic crystals.

Samples containing 0.1 wt % KAuCl_4 did not exhibit significant (if any) precursor precipitates, so this concentration was set to compare the two different treatments proposed to obtain AuNPs.

Monolayers treated with [UV + (UV + T)] do not show a significant change in color. A slight coloration of the sample with some violet shades and dark blue spots is observed, as illustrated in **Figure 5.14a)**. SEM analysis (**Figure 5.14b-c)**) show that the AuNPs are self-assembled into clusters that may reach sizes above 1 μm . These clusters are not present in the whole sample, which could be the proof that under these conditions, some AuNPs are produced but only in some areas and not all over the sample. These areas might be the regions where small crystals of the gold precursor were entrapped during the SL process. These results are in agreement with the preliminary tests, where these aggregates were also observed (see **Figure 5.12)** and UV-Vis spectra did not present a well-defined plasmonic peak.

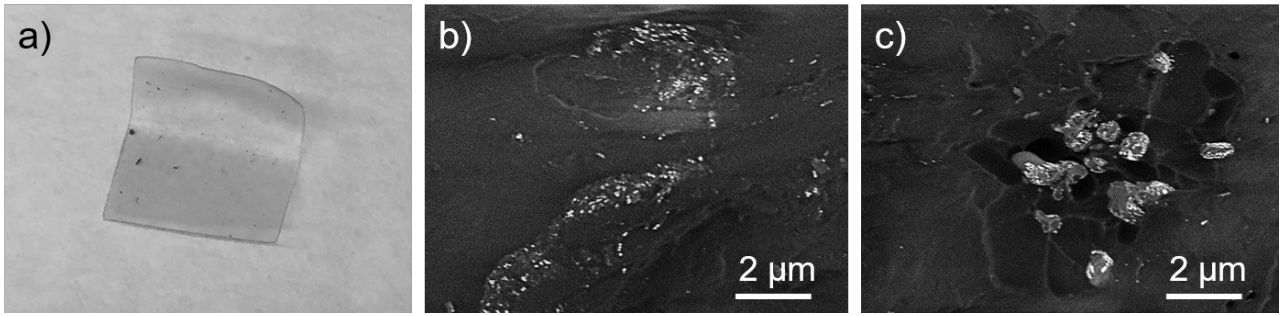


Figure 5.14 a) Digital picture and b), c) SEM micrographs of a monolayer with 0.1 wt% KAuCl_4 and 0.2 mm thickness printed by SL after $[\text{UV} + (\text{UV} + \text{T})]$.

After 1 h at 170 °C in the muffle oven, the monolayers which underwent the $[\text{UV} + \text{T}]$ treatment, exhibit a homogeneous pink color, as shown in the **Figure 5.15a**). The higher contrast between the resin and the AuNPs, given by the CBSE detector evidences that these structures are indeed AuNPs, not the gold precursor. In fact, a good distribution of AuNPs with different polygonal shapes (e.g. hexagonal, triangular...) is observed after this treatment, in agreement with previous studies^[10,13,14]. These aspects are different to what it was observed in the green samples (for instance, in **Figure 5.15c**), proving that the variation of color, together with the change in the morphology of the nanostructures is caused by the formation of AuNPs via thermal reduction of KAuCl_4 .

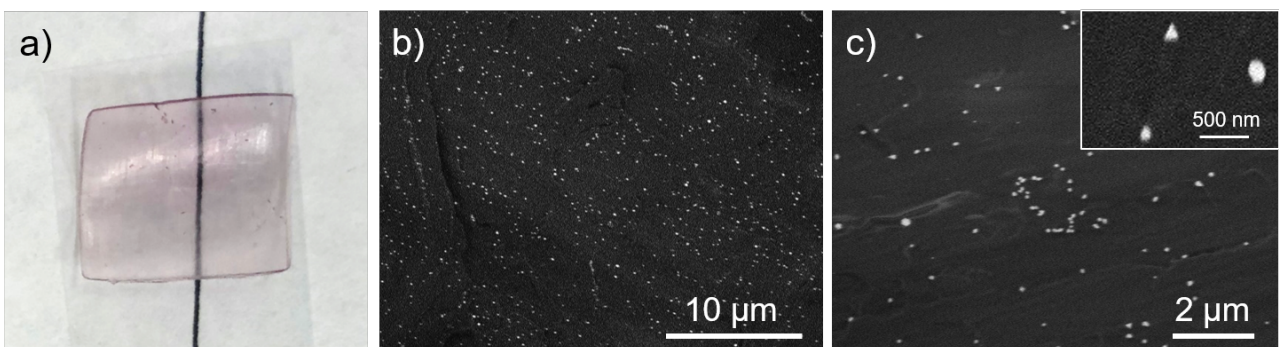


Figure 5.15 a) Digital picture and b), c) SEM micrographs of a monolayer with 0.1 wt% KAuCl_4 and 0.2 mm thickness printed by SL after $[\text{UV} + \text{T}]$. Inset in c) shows some AuNPs in the shape of nanotriangles and nano-hexagons.

A comparison of the size of the AuNPs for the two types of treatment is presented in **Figure 5.16**. It shows that the AuNPs are significantly bigger after [UV + T] treatment. This indicates that, although [UV + (UV + T)] treatment produced less homogeneous nanocomposites, with large aggregations of AuNPs, the individual AuNPs clustered into these bigger structures are smaller. Hence, although UV may play a role in favoring the AuNPs formation (since AuNPs are not formed at 80 °C in absence of UV light), the reduction of the gold precursor into AuNPs is mostly driven by the thermal reduction of Au³⁺ as higher temperatures increase the reduction and growth kinetics of the AuNPs.

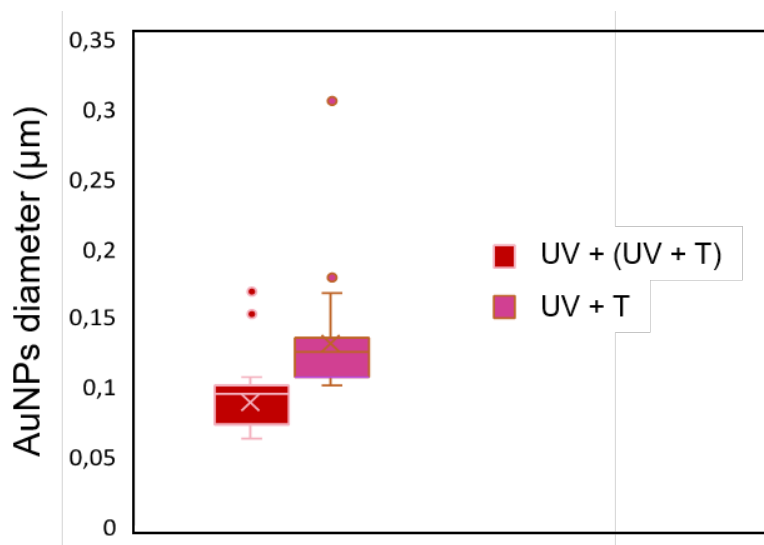


Figure 5.16 Box plot of the average AuNPs diameter for monolayers with 0.1 wt% KAuCl₄ and 0.2 mm thickness printed by SL after [UV + (UV + T)] and [UV + T].

From hereafter, all the studies will be focused on the [UV + T] treatment, since it has been proven to provide the best results in terms of distribution and amount of AuNPs synthesized, both for the preliminary tests and the printed samples by SL.

5.2.2. Influence of the concentration of gold precursor

The influence of KAuCl₄ concentration in the size and morphology of the AuNPs in SL printed monolayers is presented in **Figure 5.17**, where all the images included have been modified so they have the same magnification for direct comparison.

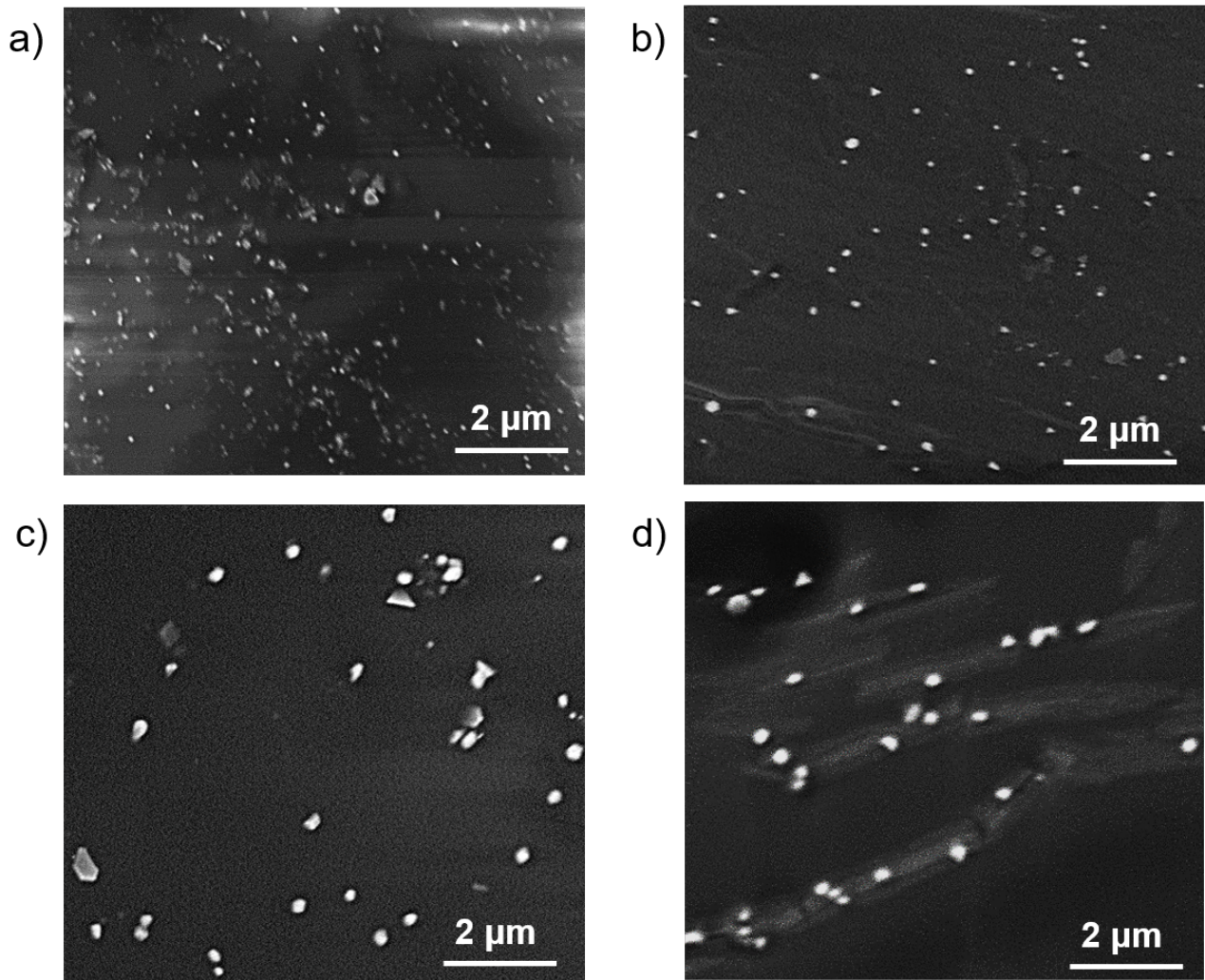


Figure 5.17 SEM micrographs of a 0.2 mm thickness monolayer printed by SL after [UV + T] with a) 0.05 wt% KAuCl₄; b) 0.1 wt% KAuCl₄; c) 0.3 wt% KAuCl₄; and d) 0.5 wt% KAuCl₄.

Interestingly, it is observed that, when the KAuCl₄ concentration is increased from 0.05 to 0.5 wt%, the number of AuNPs formed decreases, while they become bigger. This suggests that a higher amount of gold precursor does not lead to the formation of more individual AuNPs. Instead, it is likely that the Au³⁺ moieties entrapped in the polymeric matrix tend to reduce in the surface of the already present AuNPs, increasing the size of the nanoparticle following an autocatalytic growth mechanism^[15].

The AuNPs formed in 0.5 wt% KAuCl₄ samples (Figure 5.17d)) are significantly larger for printed samples than the ones produced in the preliminary tests (Figure 5.12). Also, they appear to be distributed only in some defined areas of the sample. On the other hand, samples containing 0.05 an

0.1 wt% KAuCl₄ exhibit a good distribution of the AuNPs along the whole surface of the material, indicating that lower concentration values lead to more homogeneous nanocomposites for printed samples. Since this effect was not observed in the preliminary tests, it suggests that this is somehow related to the SL printing process. Since it was previously observed the presence of KAuCl₄ crystals in the green samples after SL printing, it may be attributed to the formation of these structures prior to the thermal treatment.

A quantitative analysis of the AuNPs for this range of concentrations is presented in **Figure 5.18** and **Figure 5.19**. As previously discussed, an increase in the concentration causes an increase in the diameter of the AuNPs, with a reasonable linear correlation ($R^2 = 0.9597$). In all cases, there can be found several outliers with diameters significantly above the average values. These bigger AuNPs may be originated from the coalescence of individual nanoparticles that have merged into a bigger one. However, in general, the polydispersity index is similar in all these cases, as it can be extracted from the different error bars corresponding to the standard deviations of the data analyzed.

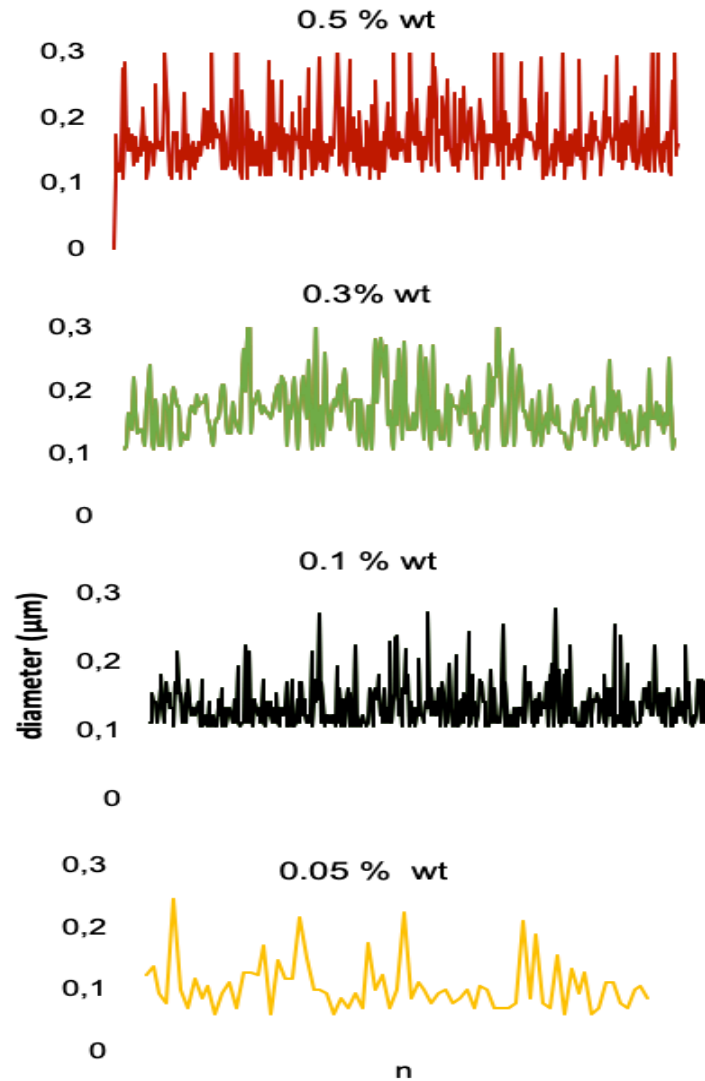


Figure 5.18 *Quantification of the AuNPs diameter in a 0.2 mm thickness monolayer printed by SL after [UV + T] with KAuCl_4 ranging from 0.05 to 0.5 wt%.*

5.2.3. Influence of the size of the printed object

A comparison between monolayers and multilayered objects (namely, 3D structures) is made for nanocomposites containing 0.1 wt% KAuCl_4 . For this purpose, a parallelepiped with 5 layers (i.e. 1 mm thickness) and the same area than the monolayers are printed. In the same study, monolayers with 0.2 and 0.02 mm thickness are also printed. Then, all these samples are subjected to the [UV + T] treatment. The procedure is represented in **Figure 5.20**.

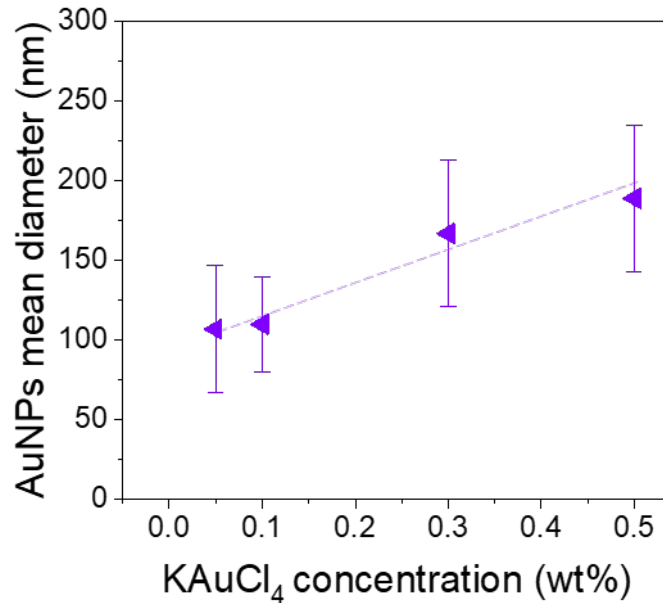


Figure 5.19 Influence of the KAuCl_4 concentration in the AuNPs mean diameter for 0.2 mm thickness monolayers printed by SL after [UV + T]. The mean diameter follows a linear trend with the concentration of the gold precursor.

As expected, all samples are transparent before the thermal treatment in the muffle oven due to the absence of AuNPs. However, after the thermal treatment, samples exhibit a different color, ranging from pink to blue depending on their thickness. The sample with 0.02 mm thickness shows a homogeneous, intense pink coloration. The monolayer with 0.2 mm thickness manifests a similar pink color than the 0.02 mm thickness, but only at the edges of the sample. In the center of the sample the coloration turns gradually into purple and then into light blue. The same behavior is observed for the multilayered 3D structure with 1 mm thickness, although the pink color is observed more locally at the edges and the transition towards the blue color is more abrupt.

The mechanical properties of the monolayers are rather poor and often bend over themselves or even break, especially in the case of the samples with 0.02 mm thickness. On the other hand, the multilayered structure is self-standing, does not bend and exhibit good mechanical properties. These results show that both the mechanical and the optical properties are affected by the thickness of the sample.

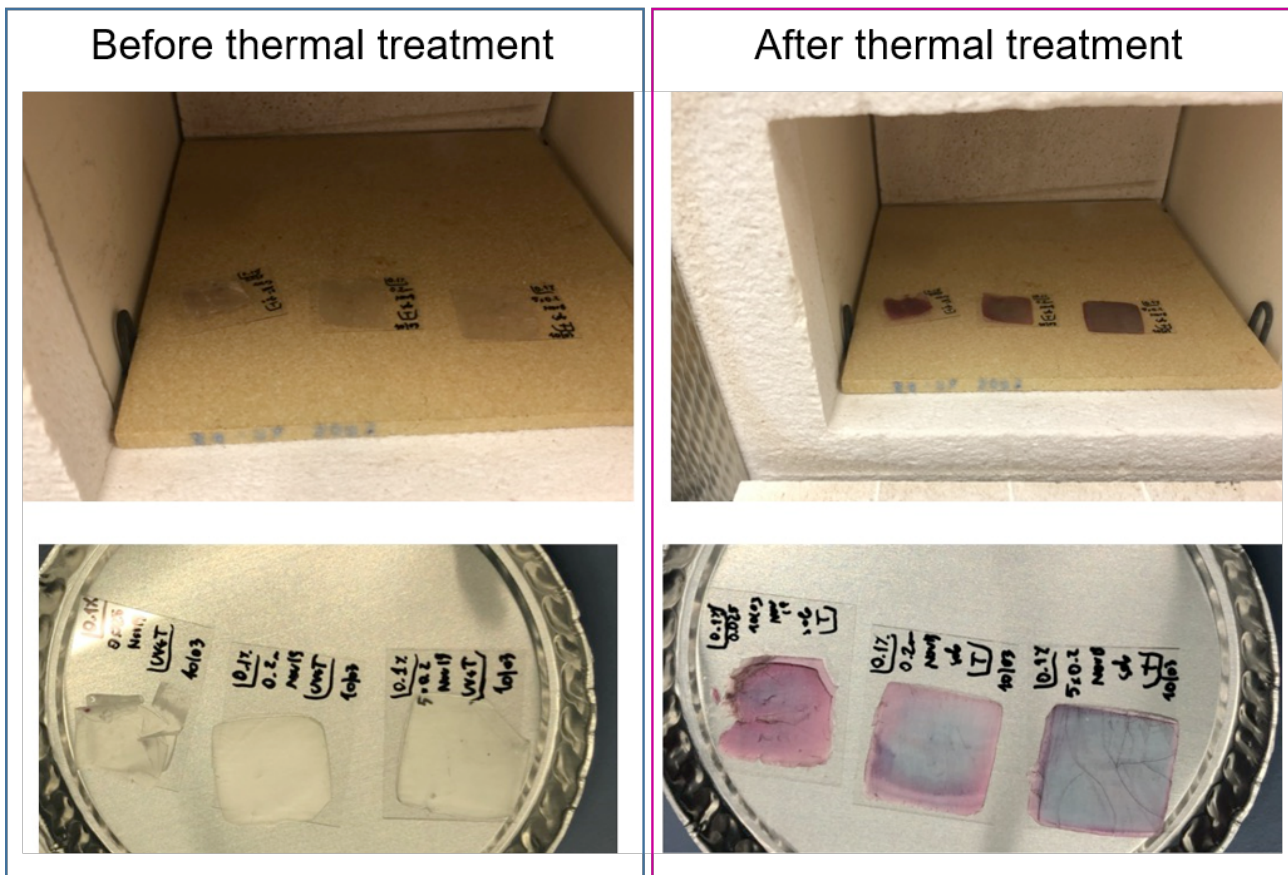


Figure 5.20 Digital pictures of samples printed by SL with 0.1 wt% KAuCl_4 and 0.02mm, 0.2 mm and 1 mm thickness before (left) and after (right) the thermal treatment of [UV + T]. The samples are arranged in increasing order of thickness, from left to right, in all pictures.

To gain further insight in the variation of the optical properties of these samples (i.e. the change in color), SEM analyses was done in the samples with 0.2 and 1 mm thickness. These samples contain 1 and 5 layers respectively. Monolayers of 0.02 mm thickness could not be analyzed by SEM since they got immediately charged under the electron beam and no images could be taken. **Figure 5.21** shows that the amount of AuNPs found in the multilayered 3D structure is substantially higher and the average size of the AuNPs is slightly smaller than in the monolayer sample. However, the differences in size are not really significant and could be attributed to some local effects (either triggered by temperature or UV) during the SL or the post-curing processes.

For instance, heat transfer processes during the thermal treatment at 170 °C that may have an influence in the kinetics of thermal formation of the AuNPs.

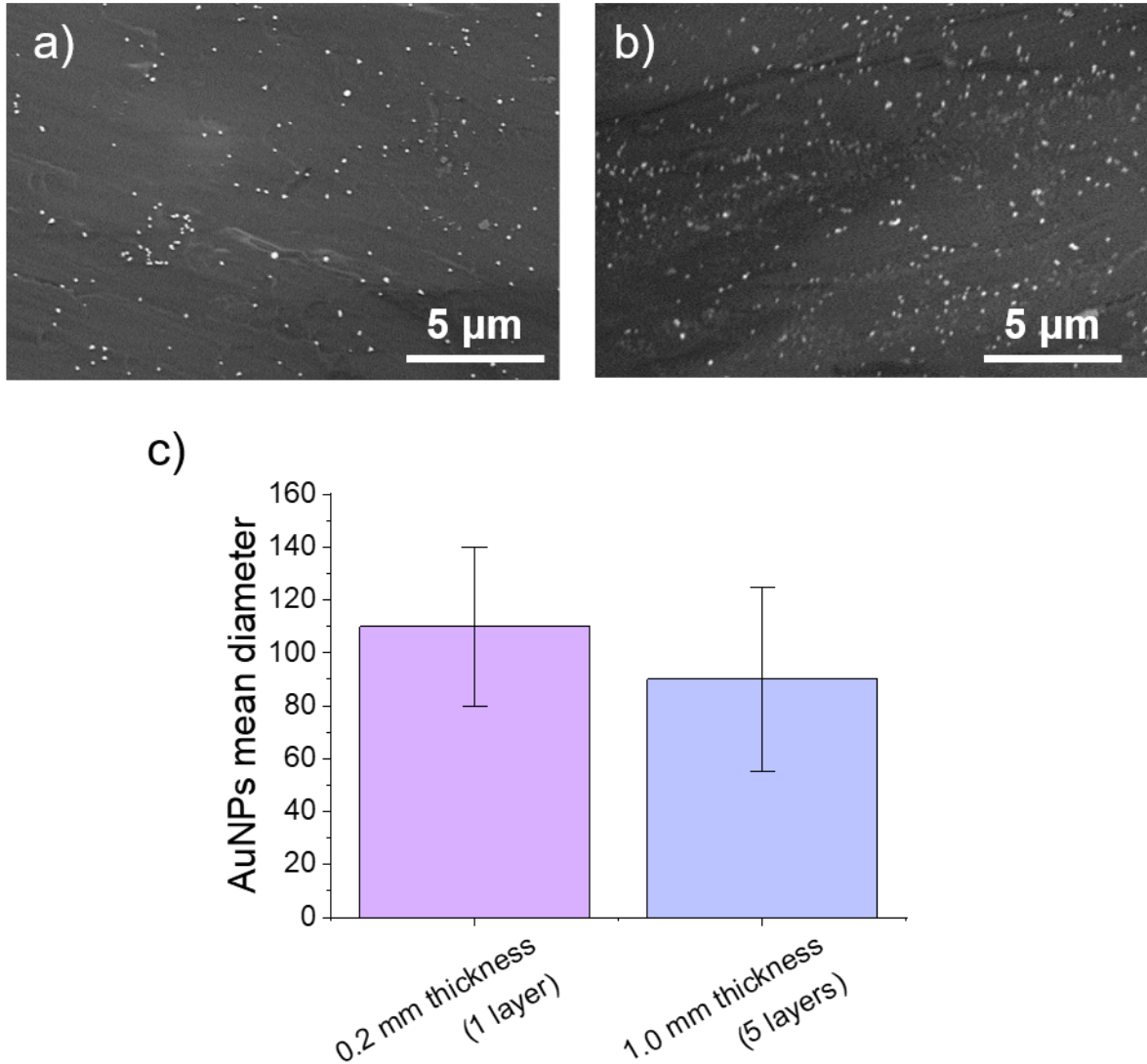


Figure 5.21 SEM micrographs of a) a monolayer with a 0.2 mm thickness and b) 3D object with 1 mm thickness containing 0.1 wt% KAuCl_4 printed by SL after [UV + T]; c) influence of the thickness of the sample in the AuNPs mean diameter.

To gain more information about the optical properties of 3D printed gold nanocomposites, a bigger parallelepiped (20 x 20 x 10 mm, 50 layers) was printed keeping a constant layer height of 0.2 mm and a concentration of 0.1 wt% KAuCl_4 . In these conditions, the object looked completely transparent without any color after being printed (green sample, **Figure 5.22a**).

Sample remained colorless after UV treatment and only after 1h at 170 °C changed into an intense, dark pink color when light is reflected (Figure 5.22b)). This color slightly changes towards violet with transmitted light (Figure 5.22c)). Sample is colored yet transparent, since the AuNPs formed possess sizes below 400 nm, i.e. under the visible range of wavelengths. As illustrated in Figure 5.22d), the text behind the 10 mm thickness sample can be easily read.

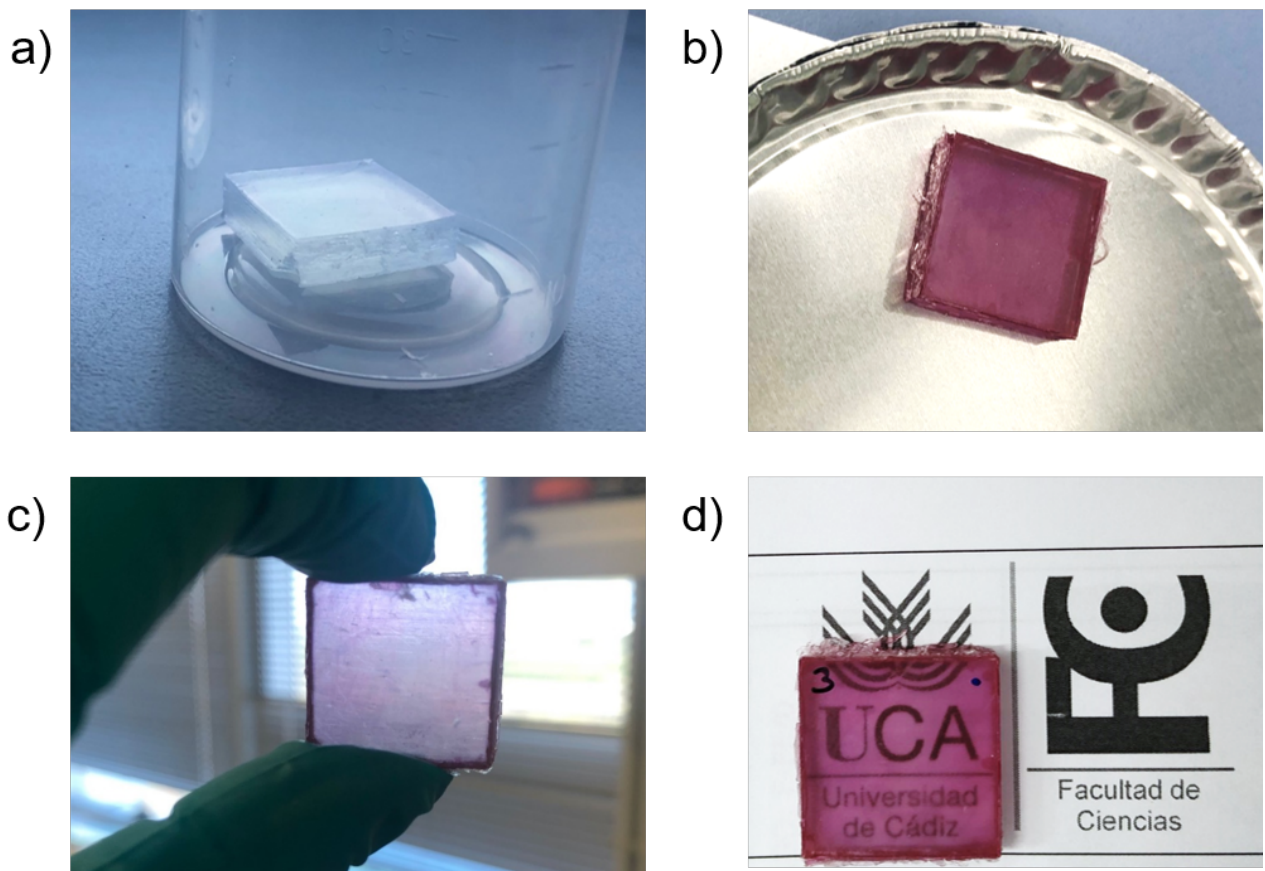


Figure 5.22 3D-printed parallelepiped with dimensions $20 \times 20 \times 10$ mm with 0.1 wt% KAuCl_4 using a layer height of 0.2 mm a) right after printing (green sample); b) after [UV + T] under reflected white light; c) after [UV + T] under transmitted white light; d) after [UV + T] on top of a text to illustrate its degree of transparency.

UV-Vis spectra of these objects were recorded to study the macroscopic optical properties of the 3D printed gold nanocomposites. Figure 5.23 shows the curves for the 3D printed sample with 10 mm thickness. Before any post-processing with UV and T, the green sample presents absorbance values between 0.2 and 0.3 in the whole visible range (400-700 nm approximately).

These values indicate that the sample is able to transmit 50-63% of if the incident light, evidencing that the sample is translucent although it holds a good degree of transparency, even with 10 mm thickness (see **Figure 5.22d**). After the thermal treatment, the UV-Vis spectra of these samples show a peak at 548 nm. These values are above the results obtained in the preliminary tests for the sandwich samples in Figure 5.7a) for this concentration, but are in well agreement with the sizes of the AuNPs observed for the monolayers and 3D object with 1 mm thickness, as depicted in the **Figure 5.21**. This data is also consistent with what can be found in the literature about the conditions of the plasmon peak^[4].

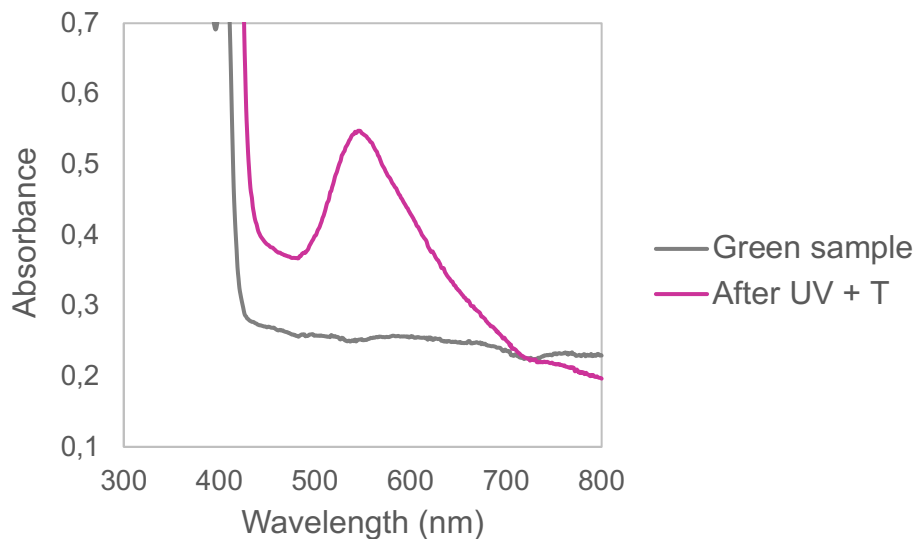


Figure 5.23 *UV-Vis spectra of a 3D-printed parallelepiped with dimensions 20 x 20 x 10 mm with 0.1 wt% KAuCl₄ before (green sample, grey curve) and after [UV + T] (pink curve).*

Finally, SEM analysis of this 3D object was done. In this case, one lateral side of the object (i.e. in the direction where the layers grow) was analyzed instead of the top surface, as it has been done until now. **Figure 5.24** shows that, unexpectedly, the AuNPs are not homogeneously distributed along the lateral XZ surface, as it happens with the top XY surface. By contrast, they are self-assembled at the edges of the individual layers, with 0.2 mm height, in a periodic manner. High magnification SEM images reveal that the size and morphology of these AuNPs are in the range of the monolayers and

previous 3D objects studied in **Figure 5.17** and **Figure 5.21**, evidencing that the mechanism of formation of the AuNPs is the same in every plane of the object. Thus, it can be concluded that 3D objects with self-assembled AuNPs in the junctions of the layer heights can be printed by combination of SL printing and a subsequent treatment combining UV light and temperature.

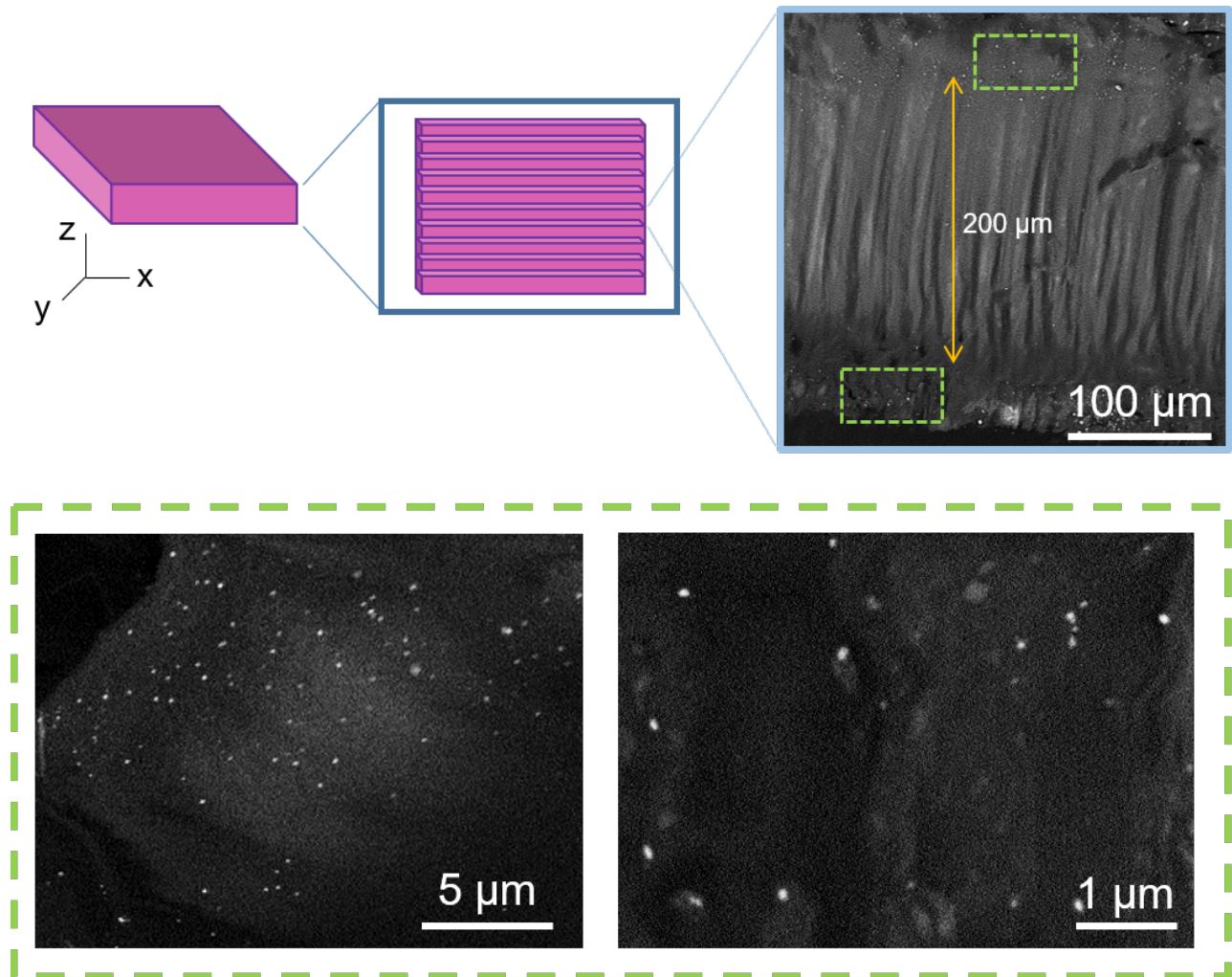


Figure 5.24 *Cartoon and SEM images of a 3D-printed parallelepiped with dimensions 20 x 20 x 10 mm with 0.1 wt% KAuCl₄ using a layer height of 0.2 mm after [UV + T]. Low magnification SEM image on top (light blue frame) demonstrates that AuNPs are selectively located at the edges of the printed layers in the XZ plane (dashed, green frames). High magnification SEM images below correspond to the detail of these regions where the AuNPs can be found.*

5.2.4. Stability of the nanocomposites. Influence of time and aging

Green nanocomposites (or those which received a post-processing that did not form AuNPs) underwent a gradual change from colorless to red and violet shades, suggesting the slow, spontaneous and uncontrolled formation of AuNPs in ambient conditions. This change in color is visible after few days and keeps evolving towards more intense tones for weeks and months (see an illustrative example in **Figure 5.25**). This effect happened even for samples stored in a dry and dark environment. Therefore, this change of color can be attributed to the oxidation of the sample due to ambient oxygen. In fact, sandwich samples, which are physically protected from air by the glass coverslips did not experienced any change in color.

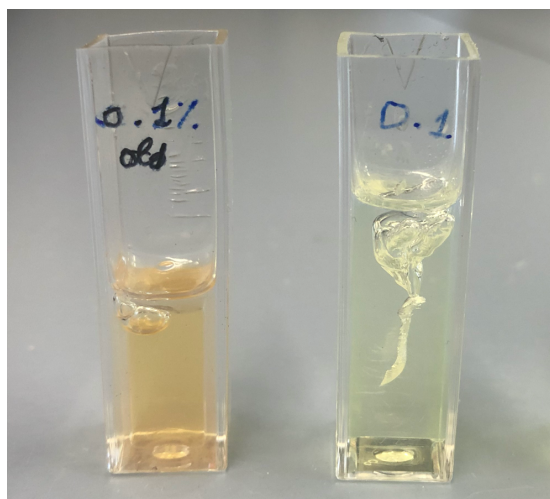


Figure 5.25 *Nanocomposites containing 0.1 wt% KAuCl_4 after UV-curing for 60 min at room temperature. Sample in the left was prepared months before the picture was taken and exhibits an orange color, caused by the presence of Au^{3+} (yellow) and AuNPs (red). Sample in the right is a fresh sample which exhibits only the characteristic color of the Au^{3+} species.*

It was also observed that printability of the liquid resin containing the gold precursor became less and less efficient if the mixture was not used immediately after preparation. This also suggests that the AuNPs might be formed by some chemical reaction with any of the monomers or even the photo-initiator which inhibits the polymerization of the resin.

However, it is important to notice that the Au^{3+} species cannot be oxidized into Au^0 , but they must be reduced. In fact, gold is one of the few elements whose most thermodynamically stable form is its non-oxidized, metallic structure^[16].

Hence, we hypothesize that the mechanism is as follows: the polymer matrix is slowly oxidized (degraded) by presence of oxygen in air. This process favors the reduction of the Au^{+3} entrapped in the polymer matrix via redox reaction, forming AuNPs in an uncontrolled manner.

To avoid any alteration in the microstructure of the gold nanocomposites, all the characterization (i.e. SEM measurements) was done in less than two days after preparation. Also, as a good laboratory practice, it is recommended to store this samples in vacuum or under an inert atmosphere such as argon or nitrogen. The gold nanocomposites that underwent the [UV + T] treatment, no further changes in color were observed, evidencing that this treatment fully reduces all the gold precursor into AuNPs and these materials are stable with time.

6. TP-DLW of metallic structures on opaque substrates

In this chapter we are going to introduce the novel technique employed to produce gold nanopatterns on opaque substrates of silicon, taking advantage of the TPA process, the photoreduction of photosensitive metallic precursors and of a particular growing mechanism which allows to have a better control on the nanoparticles' size.

Before proceeding with the nanofabrication of the gold nanostructures (AuNSs), preliminary tests for calibration are performed using the commercial photoresists usually employed with the TP-DLW apparatus, and different polymeric matrices in combination with the gold precursor (see **Chapter 4** for more details). This allows to find an adequate polymeric network for entrapping the metallic nanoparticles preventing unwanted diffusive processes, along with a better control on the hydration conditions of the sample. Moreover, a study on the range of concentrations and exposure/growth times can be used in the TP-DLW apparatus for the production of high quality AuNSs while a specific protocol of seeding and growth of the nanoparticles and the nanostructures is used to further fine-tune the size and density of both.

First, a SEM characterization is done leveraging the electronical properties of gold to verify the quality of the nanopatterns and to find a correlation between the printing parameters and the size of the structures. Then, complementary analysis with TEM and STEM (HR-TEM, HAADF-STEM, EDX) are done to investigate the morphology of the AuNPs, their size and shape depending on the different parameters. The physical processes behind this technology, the technology itself and the used materials and equipment are described in **Chapter 4**.

6.1. Preliminary tests: TP-DLW with commercial photoresists (TPP)

The preliminary tests are performed to find the most suitable materials between the candidates for the role of polymeric matrix and for the metallic precursor.

In analogy with the SL, we made preliminary tests with little amounts of gold precursor to avoid waste of material and time, we also made for TP-DLW a calibration test to find the best printing parameters, using the commercially available photoresists by NanoScribe GmbH (Germany). Then, these experiments will be repeated with the mix between polymers and the gold precursor.

The polymers and fillers must fulfil specific requirements to allow a good processability. In particular it is appropriate to monitor the:

- optical absorption that has to be negligible in the region of the wavelength of interest to minimize the single-photon (SP) processes. It could negatively affect the *voxel* definition combined with the thermal effects which may give rise to thermal undesired initiated polymerization and trigger stress or distortion of the object¹⁻³;
- refractive index of the polymeric matrix and the filler which have to be as much as possible near to 1.52, to match the refractive index of the hosting matrix (polymer), in order to mitigate any damaging of the focus figure of the laser beam and a degradation in resolution;
- matching between host matrix index and filler index, to avoid the scattering, especially when the material is optically inhomogeneous on wavelength scales of interest.

Then, the control of the filler surface chemistry is important to promote the homogeneous dispersion inside the host matrix. This will grant a better processability and maximum consistency of mechanical properties of the composite.

The study of using micro-porous materials as substrates for fabrication is a necessary pursuing approach to find the most suitable material which means transparent (glass or polymer) or opaque highly reflective (silicon) substrate, with a micro-porous structure in the dimension perpendicular to the working plane, thereby adding a degree of freedom to the process strategies. A further condition is that the material has to ensure adhesion of the created object when a solvent is used. For this aim organic and inorganic coatings will be tested.

By using TP-DLW with IP-L 780, one of the photosensitive resins apt especially for plasmonic, photonic and biometric surfaces, first experiments are made following the traditional protocol on a glass substrate with the oil immersion configuration.

In a previous work, our group elucidated the physics behind this DLW fabrication method triggered by the TPA process and pointed out the diffusive process underlying the created nanoparticles growth and the necessity to have a polymeric network in order to synthesize self-standing metallic nanostructures, preventing their free diffusion ^{4,5}.

Here we are going beyond, aiming to improve and optimize the printing parameters as laser power (LP) and scan speed (SS) or exposure time (ET) for our kind of structures (**Figure 6.1**), using as the test bench the TPP. Values allowed for LP are below 70 mW and those of SS are very high, up to 12000 $\mu\text{m/s}$.

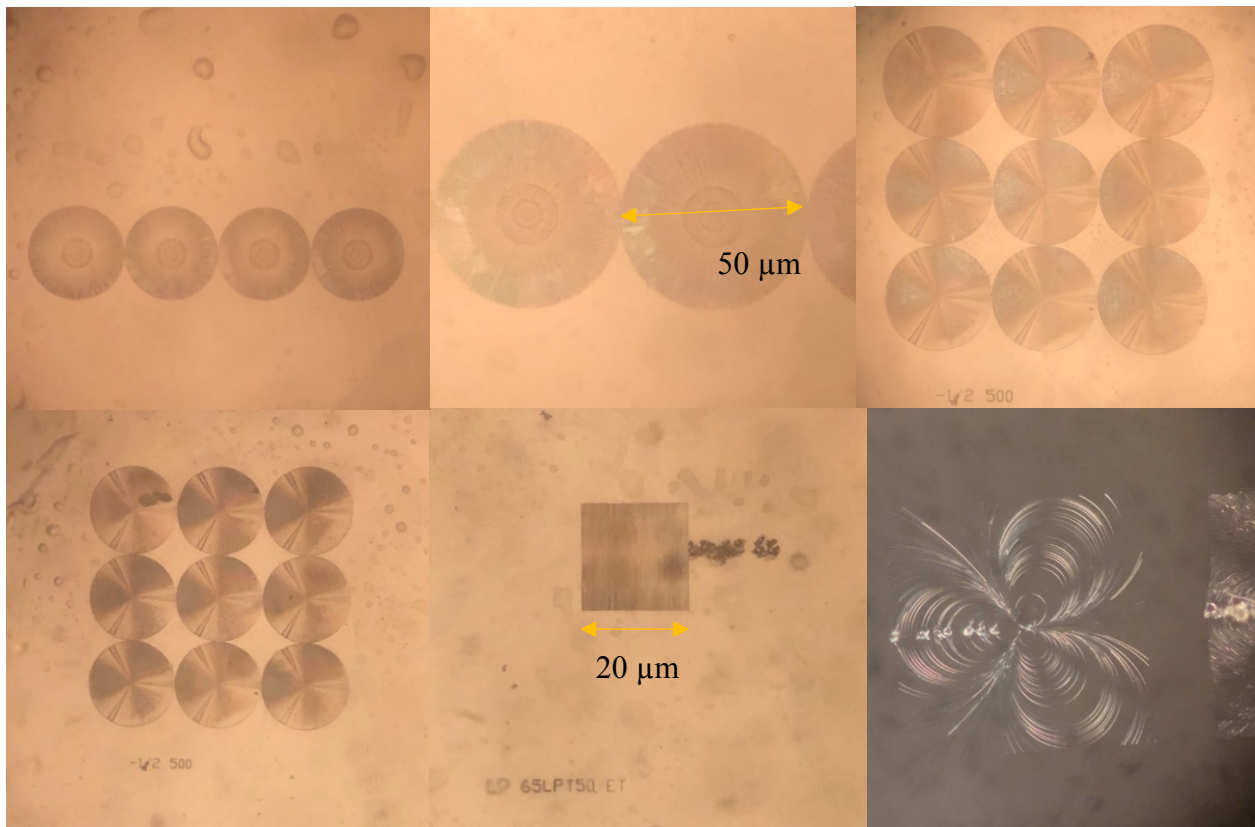


Figure 6.1 *Optical microscope images are shown as example of the kind of patterns we can realize with the traditional protocol, using IP-L photoresist and the 63x objective in the oil immersion configuration, LP = 65 mW, SS = 12000 $\mu\text{m/s}$.*

6.2. TP-DLW with PVA and gold precursor on a transparent substrate

Then we proceeded with a glass substrate, a polymeric matrix, the polyvinyl alcohol (PVA, molecular weight: 13.000–23.000 g/mol) and the gold precursor, tetrachloroauric acid tetrahydrate ($\text{HAuCl}_4 \cdot 3\text{H}_2\text{O}$). The use of metallic precursors as silver nitrate (AgNO_3), copper chloride (CuCl_2), nickel (II) chloride (NiCl_2) and tetrachloroauric acid (HAuCl_4) allow to obtain the corresponding metallic nanoparticles (NPs) through a photoreduction reaction. In particular, HAuCl_4 is the most common gold precursor used for the optical synthesis of gold nanoparticles and it can be photo-reduced by single photon UV irradiation and by two-photon absorption of infrared light.

In this case, it is necessary a polymeric network in order to hold the created NPs at their place, preventing their free diffusion. The structures can be fabricated through a glass, with an oil-immersion objective or using the objective working in air.

The disadvantage of this approach is that the aqueous solution of PVA and HAuCl_4 is deposited directly on the glass substrate in the form of a drop, but it is necessary to wait the evaporation of water before proceeding with the printing. It means that typically one hour and half has to pass until only an amount of 0.4 mg of solution remains on the glass substrate, assuring the correct hydration conditions. At this point, the TP-DLW can begin. Moreover, after printing the substrate must be immersed for 20-25 min in a deionized water bath because it is necessary to stop the growth of the gold nanoparticles and to remove the PVA matrix.

Printing parameters used are: LP=10÷20, SS=10 for linear and isolated points structures and LP=20, SS=50 for the text.

The results are shown in **Figure 6.2**. Some remnants of polymeric matrix are still visible and this forbids to have clean substrates with nanopatterns only.

For a glass substrate, the optimization of printing parameters and of times for removing the excess of ions lead to low values of LP (10-20 mW), SS of 10 $\mu\text{m/s}$ and a short time between the printing and the bath in deionized water (less than 1 day).

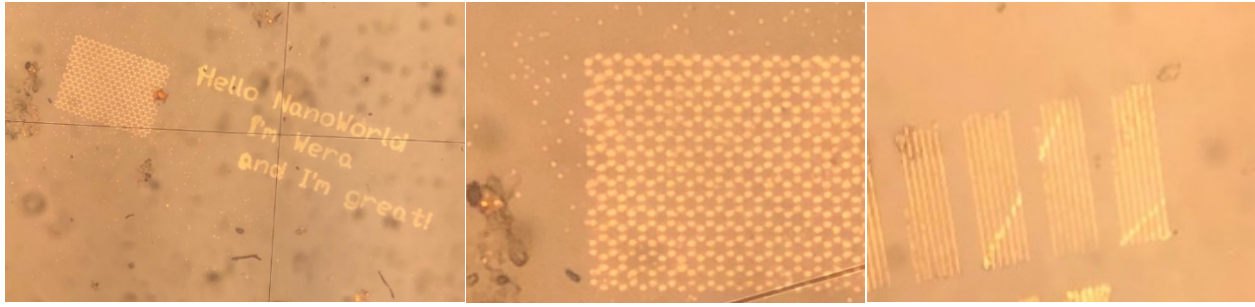


Figure 6.2 *Optical microscope images of nanopatterns printed on glass with $LP=10-20$ mW, $SS = 10\mu\text{m/s}$, $d=2\ \mu\text{m}$. The (b) image is a magnification of isolated points shape structure of (a). (c) Linear structures ($l = 20\ \mu\text{m}$).*

6.3. TP-DLW with PVA and gold precursor on an opaque substrate

The same tests are then repeated on a silicon substrate in order to expand the many applications that the use of the TP-DLW onto an opaque substrate can bring.

In this case the creation of a closed chamber (i.e. a cell) is necessary. We need a glass as interface between the objective and the gold precursor and so we created a sample with glass and silicon where a thickness (max $10\ \mu\text{m}$) between is created with two stripes of mylar, or other surface coupling agent like silica-microspheres ($5\ \mu\text{m}$) or DMOAP (Dimethyloctadecyl[3-(trimethoxysilyl)propyl] ammonium chloride). The gold precursor is infiltrated by capillarity between the two layers. Since the total thickness of the sample is larger than the case of only glass substrate we have to be careful and to monitor the working distance during the approach to the sample in the printing process.

With this method the thickness of the layer is a problem because the focus figure of the laser beam is reduced and it must pass several layers before reaching the silicon substrate, and it is necessary a Laser Power up to 100 mW ($I_{LB} \propto \sigma^2$ where σ is the cross section).

It is for this reason that an attempt to change the configuration is done: we try to print with the objective that works in air. In this way we can approach the sample directly without other interfaces in between.

A comparison between the structures produced with the objective working in oil immersion and those ones produced with the objective working in air is made.

At this point a second novelty is introduced: it regards the separation of the drying stages, namely:

- first a controlled deposition: with the use of the spin coater, by which we can control thickness and temperature of the polymeric matrix, it is allowed to the matrix to dry in very short times (few minutes);
- then the deposition of the gold precursor is possible to ensure that the gold nanoparticles become trapped in the lattice created by the matrix.

First tests are made with a drop cast (100 μL) of the gold precursor on the substrate (**Figure 6.3 - Figure 6.4**), but this method introduced a problem about the control of the concentration so the third novelty is introduced: instead to use a drop of solution it will be used a bath in an aqueous solution of the gold precursor. This change leads to two advantages:

- a better control on ionic concentration because with the bath it is possible to reach quickly, by estimating diffusion times (following the Fick's law $\sim 100\text{ms}$), the steady state between the bath and the matrix;
- saving of materials, because it is not necessary to wait evaporation times and lose a great amount of aqueous solution, in fact the bath can be re-used.

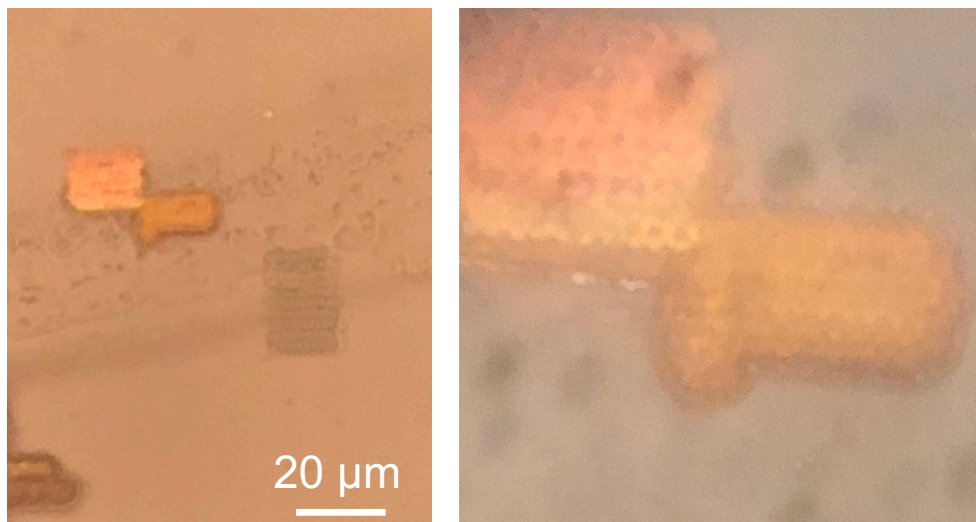


Figure 6.3 *Optical microscope images of nanopatterns. On the right a magnification of the isolated points structures.*

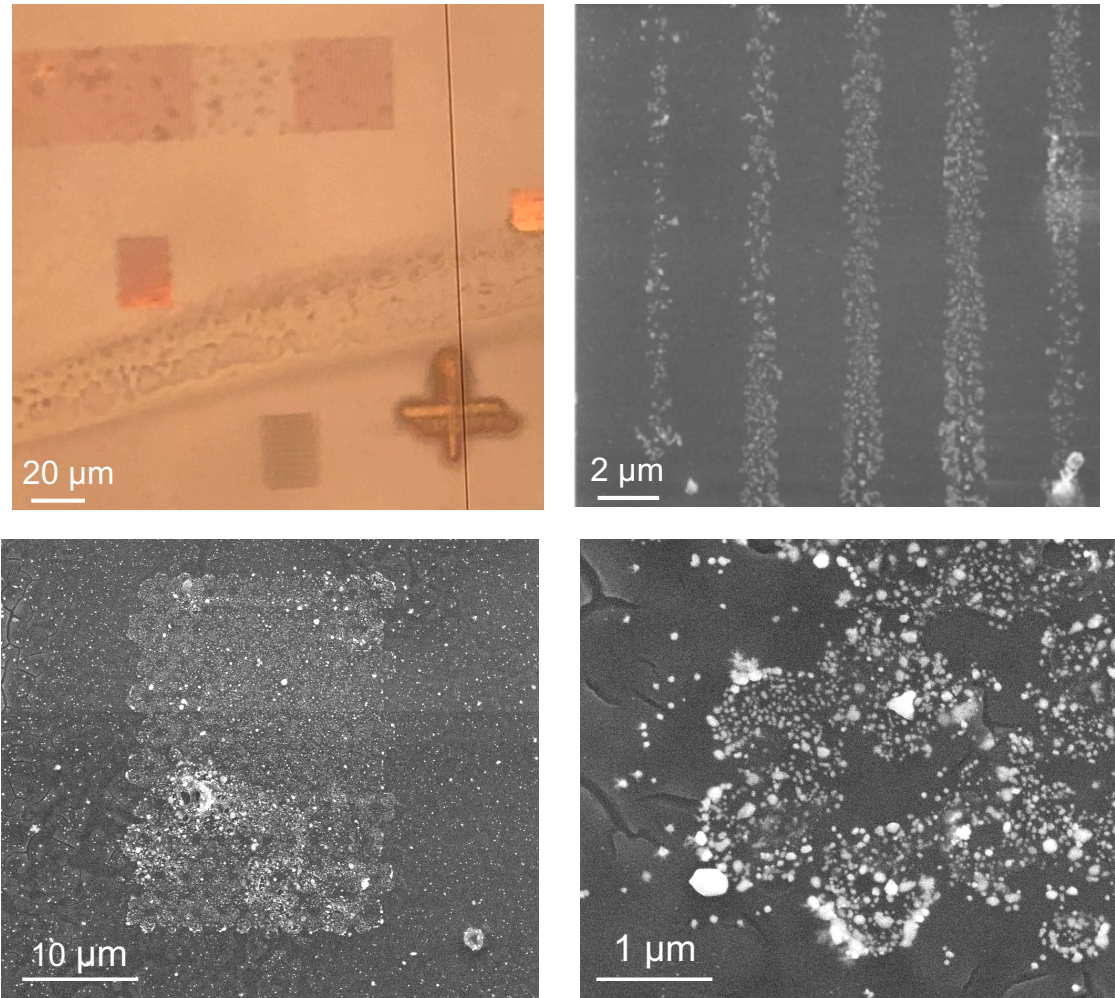


Figure 6.4 (a) An optical microscope image of nanopatterns. (b), (c), (d) SEM images of the structures, linear and isolated points respectively, and a magnification of the isolated points structures. We need to use two drops of solution ((50+50) μL to obtain visible structures.

The behavior of the PVA after the bath is not ideal because this polymer is water-soluble and the entrapment of the AuNPs is only partially achieved. For this reason, the concentration is not homogeneous all over the sample the same and the sensitivity to the TPA process is different in the various areas depending whether the matrix is present or not (**Figure 6.5**). Furthermore, if the entire process is not carried out in 24 hours (**Figure 6.6**) despite the deionized water bath not all the matrix it can be removed and the sample doesn't result totally clean (**Figure 6.7**).

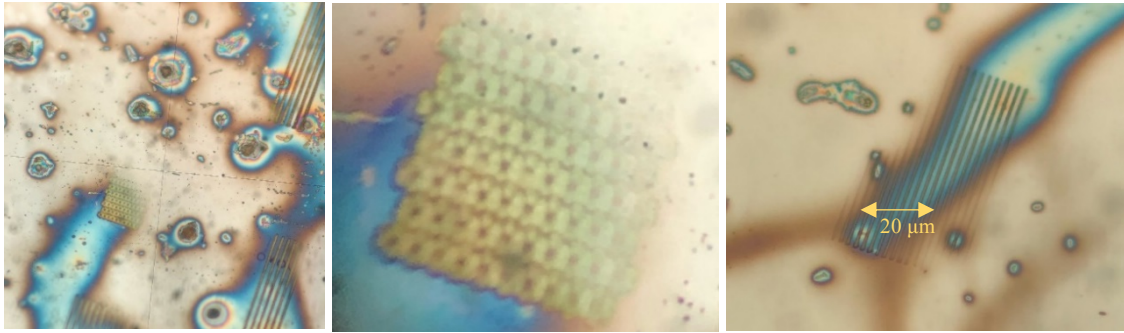


Figure 6.5 Structures are printed but only in some areas, where the drop is dryer and the process can be carried out. After the deionized water bath some structures are washed away.

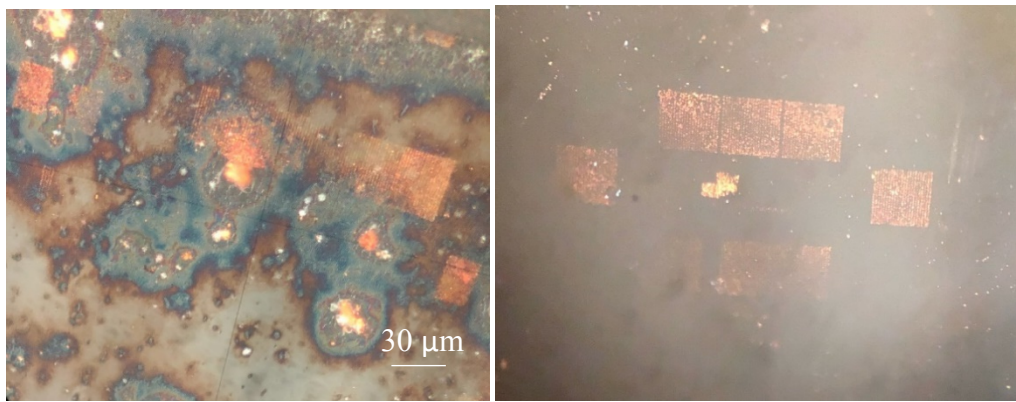


Figure 6.6 Before and after the deionized water bath, in a time in less than 24 h.

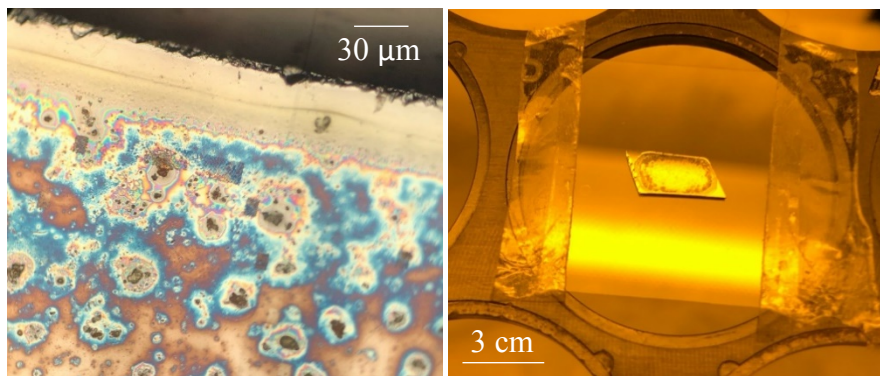


Figure 6.7 (a) An optical microscope image where is shown that the sample does not result totally clean also at naked eye (b), despite the bath in deionized water.

6.4. TP-DLW with isinglass and gold precursor on an opaque substrate

With the purpose of improving the results achieved with PVA, especially the removal of the polymeric matrix from the sample and the quality of the structures rich of gold and a better compliance with the geometrical model, we decided to use a different polymeric matrix. We decided to adopt a hydrogel because of the higher optical homogeneity and better controlled diffusive properties comparing to the “traditional” PVA matrices. In particular we choose isinglass, a hydrogel of natural origin.

The advantages of this material are:

- is a natural, protein-based matrix, fully in accordance to the principles of the green chemistry;
- is a highly performing hydrogel, especially in terms of diffusive processes and ionic mobility (i.e. is a colloid, hydrophilic so it can remain as damp as a sponge and it is possible to write more times on the same sample if re-hydrated);
- it is transparent, hence optically accessible at the wavelength of the laser ($\lambda \sim 780$ nm).

Along with the control of the laser parameters, the fine-tuning of the ionic concentration is also exploited to monitor the seeding density and the growth size of AuNPs clustering in the laser focus.

The advantages of the proposed approach, combining TP-DLW and the AuNPs growth strategy are evident in terms of resolution and control of the structures created.

In fact, in the high resolution nanofabrication scenario, this TP-DLW combined technique, especially for the production of gold nanostructures, is highly powerful compared to other tactics, like focused ions beams based (FIBID, EBID), self-assembling or molecular beam epitaxy, since it allows to realize 2D but also complex 3D structures, in very short times (high printing rates) and with reduced costs⁶⁻⁸.

Moreover, thanks to the triggering of TPA, it is possible to widen the choice of the materials employed and to integrate the use of metallic precursors with polymeric materials in addition to the usual photoresists for TPP.

6.4.1. Seeding and Growth

Gold nanostructures (AuNSs) were synthesized through the TP-DLW process, taking advantage of the photo-reduction with a fine-tuning of shape and size acting on the ionic concentration of the salt. For the first set of seeding experiment, 10^{-2} M HAuCl₄ concentration is chosen for the 30 minutes first bath. The time is set quite larger than the expected one from the Fickian diffusion to ensure the homogeneous diffusion of the Au³⁺ cations from the solution into the isinglass hydrogel matrix.

In fact, a help to this comes from the Fick's law of diffusion that explains well the dynamics of the nanoparticles/ions which diffuse inside a polymeric matrix, neglecting viscosity and friction side effects. This relationship links the ion diffusivity D_{ion} and the ions concentration c , expressed as:

$$\frac{dc(x,y,z,t)}{dt} = D_{ion} \nabla^2 c(x, y, z, t) \quad (9)$$

Due to the symmetry of the system, we can consider it as a polar reference frame. Assuming that c does not depend on polar and azimuthal angles, the equation (9) can be rewritten as:

$$\frac{dc(r,t)}{dt} = D \frac{d^2 c(r,t)}{dr^2} \quad (10)$$

Then the equation (10) is a second order differential equation, that can be solved by considering the boundary conditions: at time $t=0$, for $r > R$ the ionic concentration is $c = c_0$, for $r < R$ concentration is $c = 0$, with R as the radius of the voxel. A possible solution is:

$$c(r, t) = c_0 \left(1 - \operatorname{erf} \left(\frac{r}{\sqrt{4D_{ion}t}} \right) \right) \quad (11)$$

and D_{ion} is given by:

$$D_{ion} = \mu_{ion} K_B T = \frac{K_B T}{6\pi R_{ion} \eta} \quad (12)$$

where μ_{ion} is the ion mobility, K_B is the Boltzmann constant, $T = 300$ K is the room temperature, R_{ion} is the radius of the considered ion, and η is the viscosity of the medium⁹⁻¹¹.

The diffusion times in our case are in the order of magnitude of $1 \mu\text{m/s}$ as already found in our previous work¹².

Then, thanks to the focused NIR laser at the interface with the Si substrate, photoreduction of Au^{3+} into Au^0 is activated (**Figure 4.5**), causing the reduction of Au (III) into Au^0 inside the voxel ^{13,14}.

These gold atoms are the seeds on which the synthesized AuNPs are grown through the autocatalytic reduction of the surrounding ions (**Figure 4.5d**). The use of the isinglass matrix allows for a much finer control on the AuNSs density and growth kinetics, compared to the PVA matrices commonly used, leading to the creation of high-quality structures rich in AuNPs with a reduced size dispersion. A subsequent bath in deionized water removes the chloroauric ions from the hydrogel film, stopping the AuNPs growth. This method aims to separately control the nucleation and the growth processes. However, it is important to point out that the lag between the laser exposure and the removal of the chloroauric ions should be at least in the range of 10^{-1} s to achieve a proper control of these two events. On the other hand, even using microfluidic systems embedded in the sample holder to “instantaneously” flux bare water this time cannot be made shorter than typically 10 s, considering the water diffusion time in the isinglass film, in the order of 1 $\mu\text{m}/\text{s}$. As a consequence, there is an unavoidable initial autocatalytic growth of Au ^{15,16}.

Different patterns, including isolated spots and linear structures, were tested. At first, an analysis of the dots size as a function of the laser power (LP) was performed for values ranging from 40 to 100 mW. At fixed values of the exposure time (ET = 100 ms) the mean values of the spot sizes are reported in **Figure 6.8** where the expected increasing trend with the LP is confirmed. At higher values, the beam diameter of the laser increases, which causes larger voxel sizes, forming bigger AuNSs ¹⁷. Furthermore, at high values of LP, thermal effects occur which may also promote the reduction of the Au precursor ¹⁸. The mean size of the AuNSs spots varies from (1.22 ± 0.52) μm for LP = 40 mW to (1.97 ± 0.53) μm for LP = 100 mW.

Further insight in the tuning of the dots size was done by studying the influence of a longer exposure time (150 ms) in similar LP conditions. **Figure 6.9(a-b)** shows the printed AuNS for LP = 40 mW and 100 mW. They were compared to the ones manufactured at ET = 100 ms in **Figure 6.10(a-c)** and the average values were presented in **Figure 6.11(c-d)**.

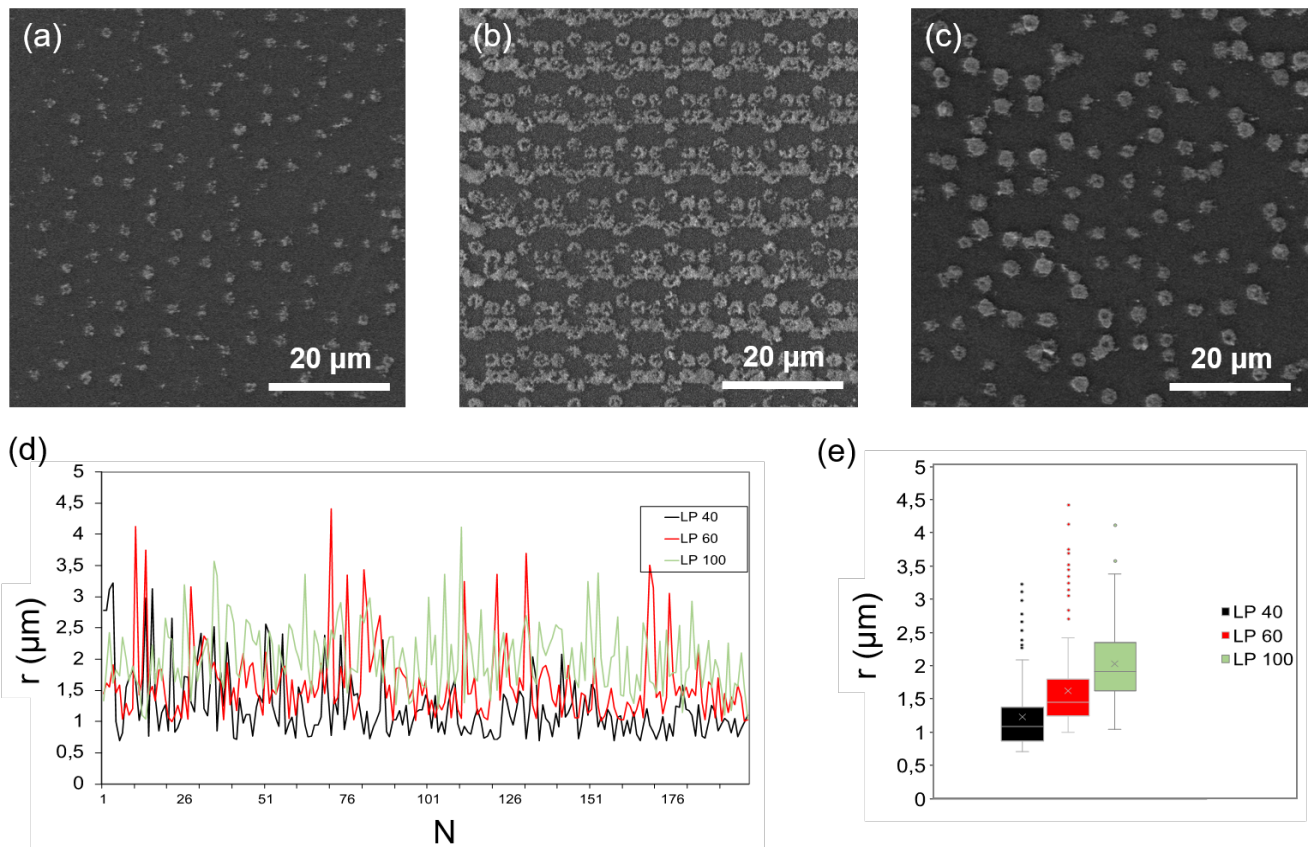


Figure 6.8 SEM micrographs showing AuNSs fabricated via TP-DLW using an $ET = 100$ ms and a LP of a) 40 mW; b) 60 mW; c) 100 mW; d) Quantification and e) box plot of the radius of the different AuNSs printed. Box plots were made in all cases from at least 180 independent measurements ($N > 180$) as shown in (d).

For LP = 40 mW the structures made with $ET = 100$ ms have smaller size than the ones fabricated with $ET = 150$ ms, even though some outliers can be observed. This could be due to a relatively low transition probability, as expected for a third order non-linear optical process. Hence, in these low LP conditions, the photoreduction of Au^{3+} can be tuned with the ET, allowing to control the AuNSs size. However, for LP = 100 mW the values are practically identical, confirming the low transition probability.

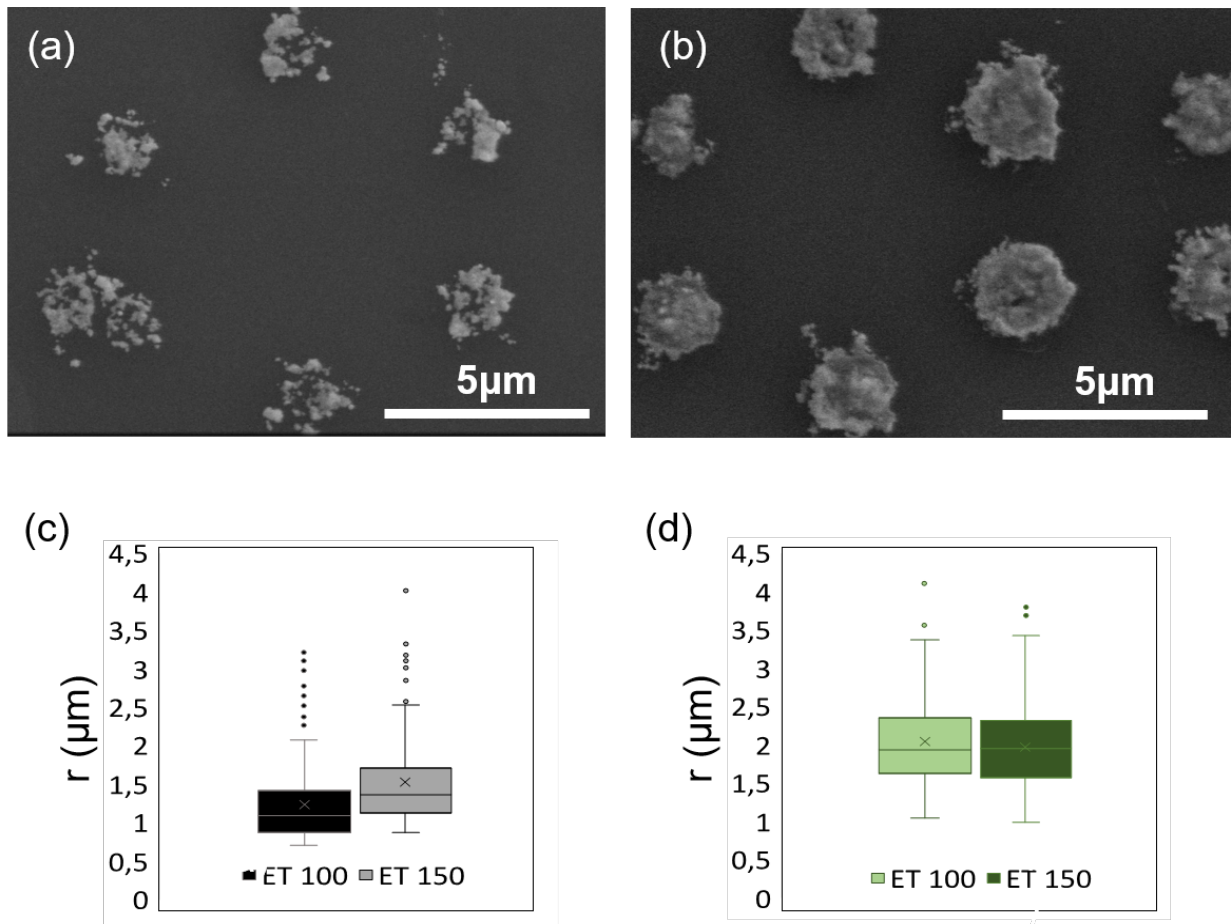


Figure 6.9 SEM micrographs showing AuNSs fabricated via TP-DLW using an $ET = 150$ ms and (a) $LP = 40$ mW; (b) $LP = 100$ mW. Box plots comparing the radius of the different AuNSs printed with different ET at (c) $LP = 40$ mW and (d) $LP = 100$ mW. Box plots were made in all cases from at least 180 independent measurements ($N > 180$).

Fabrication of continuous AuNSs (e.g. lines) in different conditions was also done. A comparison of the thickness of the lines printed at LP 40, 80 and 100 mW is presented in **Figure 6.10**. Raising the LP determines an increasing in the width of the printed lines, with mean values ranging from 1.2 to 1.6 μm when the laser power is increased from 40 to 100 mW, in analogy to the two-photon polymerization technique ¹⁹.

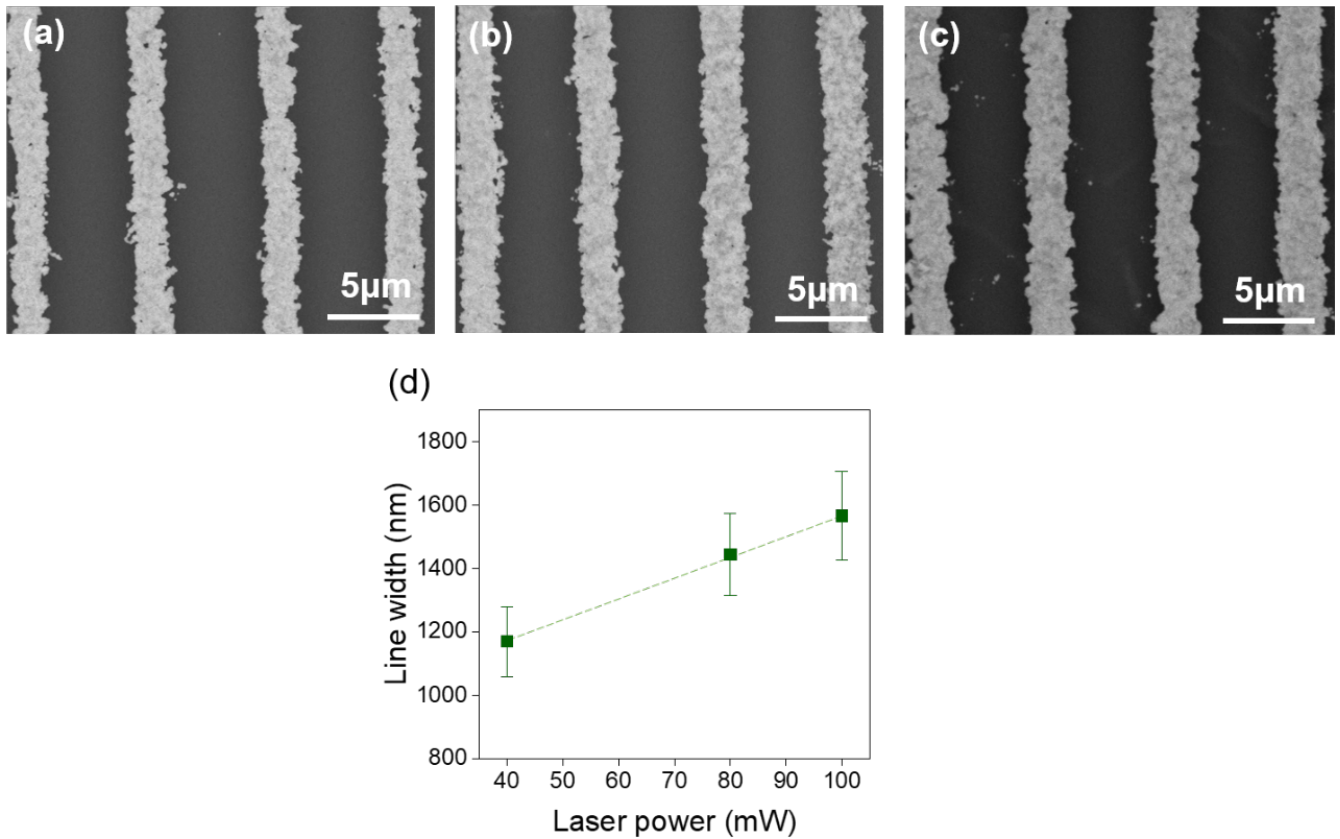


Figure 6.10 SEM micrographs showing AuNSs fabricated via DLW using a $SS = 200 \mu\text{m/s}$ and a LP of (a) 40 mW; (b) 60 mW; (c) 100 mW; (d) Average line width of the different AuNSs printed as a function of the LP.

In order to assess the possibility to control the growth of the AuNPs, a second bath in HAuCl_4 was done (see **Figure 4.6**). In this case, the isinglass hydrogel has already been eliminated and the AuNSs are fully accessible, so it is expected that the Au^{3+} in solution can be deposited onto the AuNSs and reduced into Au^0 , contributing to increase the sizes of the AuNSs in a controlled manner. **Figure 6.11** shows honeycomb-patterned AuNSs before (**Figure 6.11 (a)**) and after (**Figure 6.11 (b)**) immersion in a bath containing 10^{-2} M HAuCl_4 for 30 min. Quantification of the size of these features in **Figure 6.11 (c)** illustrates that there is a clear influence of the second bath in the growth of the AuNSs.

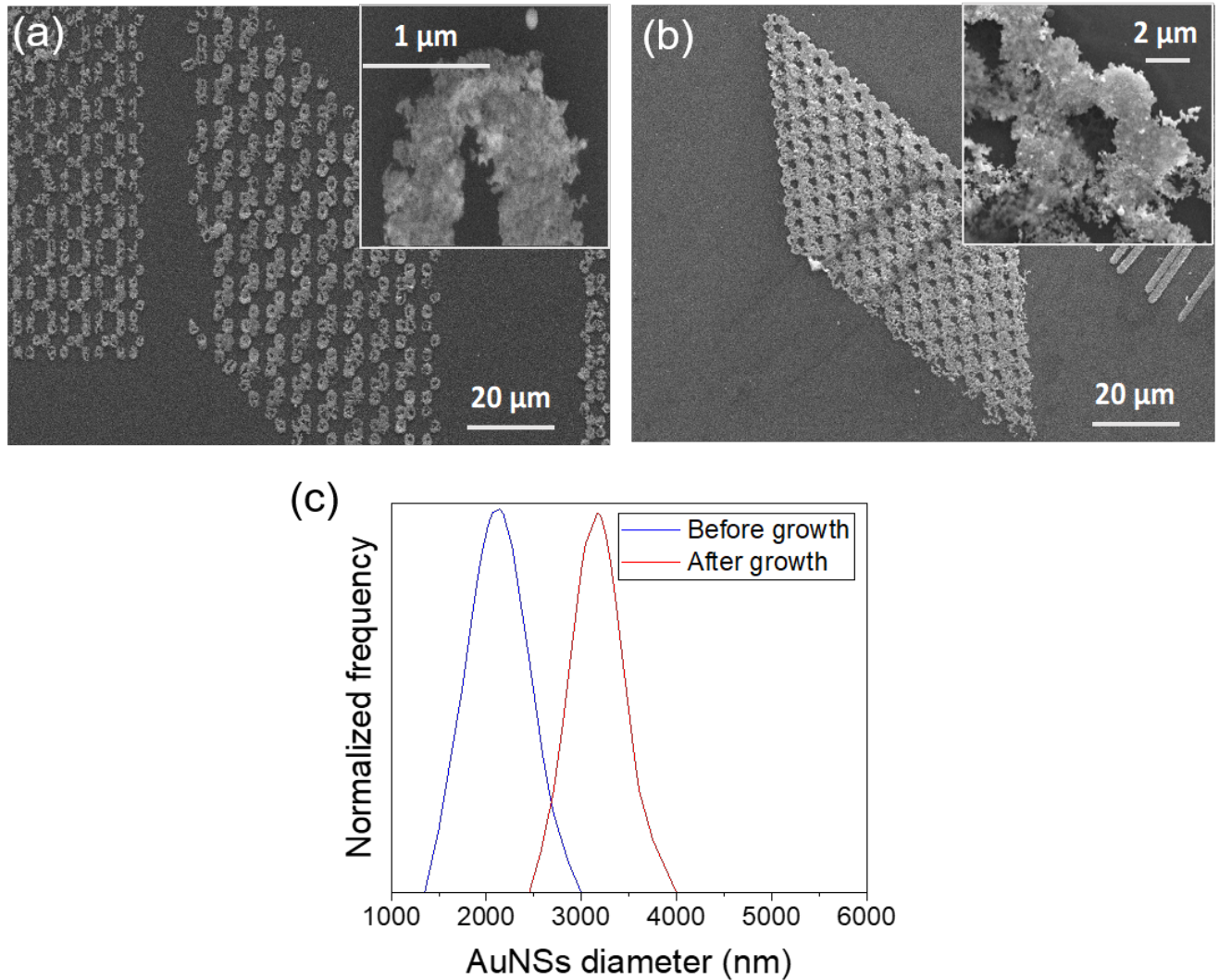


Figure 6.11 SEM images of the nanopatterns (a) before and (b) after AuNSs growth by immersion in a 10^{-2} M HAuCl_4 bath for 30 min; (c) Distribution of the AuNSs size before growth (blue, $N = 29$) and after growth (red, $N = 26$).

These AuNSs seem to be composed of individual gold nanoparticles (AuNPs) which are likely to grow individually, even if part of them coalesce. However, it is quite difficult to distinguish the single AuNPs in the SEM images and determine their size (see for instance, **Figure 6.9 (a-b)**). This is specially challenging for structures made at high LP and ET conditions, as the thermal effects lead to an even higher photoreduction nearby producing larger AuNSs.

6.4.2. Analysis of the morphology of AuNPs

To obtain more information on the morphology of the individual AuNPs of the linear AuNSs manufactured by the TP-DLW process, TEM analyses were done. These studies were conducted on a sample where the AuNSs were printed using $LP = 100$ mW and $ET = 150$ ms before and after growth in the second bath with HAuCl_4 (see **Figure 4.6**). For each sample, an electron transparent lamella with the AuNSs and the silicon substrate was extracted by FIB, as shown in the **Figure 6.12**. A Pt layer was deposited prior to FIB cut to protect the AuNSs. The lamella was several microns of width to ensure the acquisition of the cross-sections of various printed lines (depicted as gold nanowires, AuNWs in **Figure 6.12**).

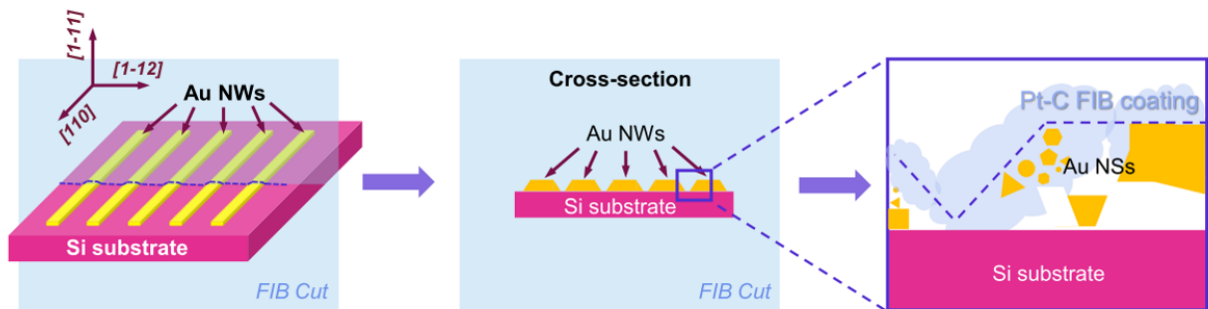


Figure 6.12 Scheme of the sample preparation for TEM analysis via FIB cut. The sample was studied along the Si (substrate) $[110]$ zone axis. A layer of Pt is deposited on the top of the sample with ion beam to protect the structures from the destructive cutting procedure.

HAADF and HRTEM images of the AuNSs after TP-DLW are presented in **Figure 6.13**, where the individual AuNPs can be appreciated more in detail. As explained before, it should be noted that in this case, there is a time gap of approximately 10 s between the AuNSs formation via TP-DLW and the washing in deionized water that stops the autocatalytic growth of the AuNPs, even though the sample has not been immersed in the HAuCl_4 bath yet. HAADF images provide chemical contrast (Z-contrast), and they indicate that areas with heavier elements are those containing AuNPs. Here, it can be observed that TP-DLW is able to create larger structures by the coalescence of smaller individual AuNPs, leading to polycrystalline, highly faceted AuNSs, as previously observed in SEM images. HAADF (**Figure 6.13 (b)**) and HRTEM (**Figure 6.13 (d)**) images also show that some of

these AuNSs are physically deposited onto the Si substrate surface, likely due to a stochastic heterogeneous nucleation event. Complementary EDX analyses presented in **Figure 6.14** support the HAADF results, indicating that AuNSs consist of solely AuNPs, without the presence of oxidized species, precursor residues or any other impurities. EDX mappings also show the thin SiO_x native layer at the substrate surface, about 2 nm thick. These AuNPs are able to self-assemble into larger micron-sized clusters. Moreover, the AuNPs formed possess different shapes (decahedral, pentagonal bipyramid, trigonal pyramidal, spherical and cylindrical), as discussed by Polte and Turner^{20,21} exhibiting a polycrystalline morphology which may facilitate the merging into larger AuNSs by photoreduction during the TP-DLW process.

A lamella of similar dimensions was cut by FIB after the AuNSs were immersed in a 10⁻² M HAuCl₄ bath for 30 min. Direct comparison between **Figure 6.13** and **Figure 6.15** allows to evaluate the influence of the bath in the growth of the AuNSs and AuNPs. After the bath, individual AuNPs are not appreciated, but they have been merged by their facets and exhibit a higher polycrystalline morphology. Quantitative analysis of these AuNPs sizes show that they range from 50 ± 11 nm to 123 ± 35 nm (see **Figure 6.16**). These results support our previous findings in **Figure 6.11**, where a significant increase in the AuNSs size was also observed.

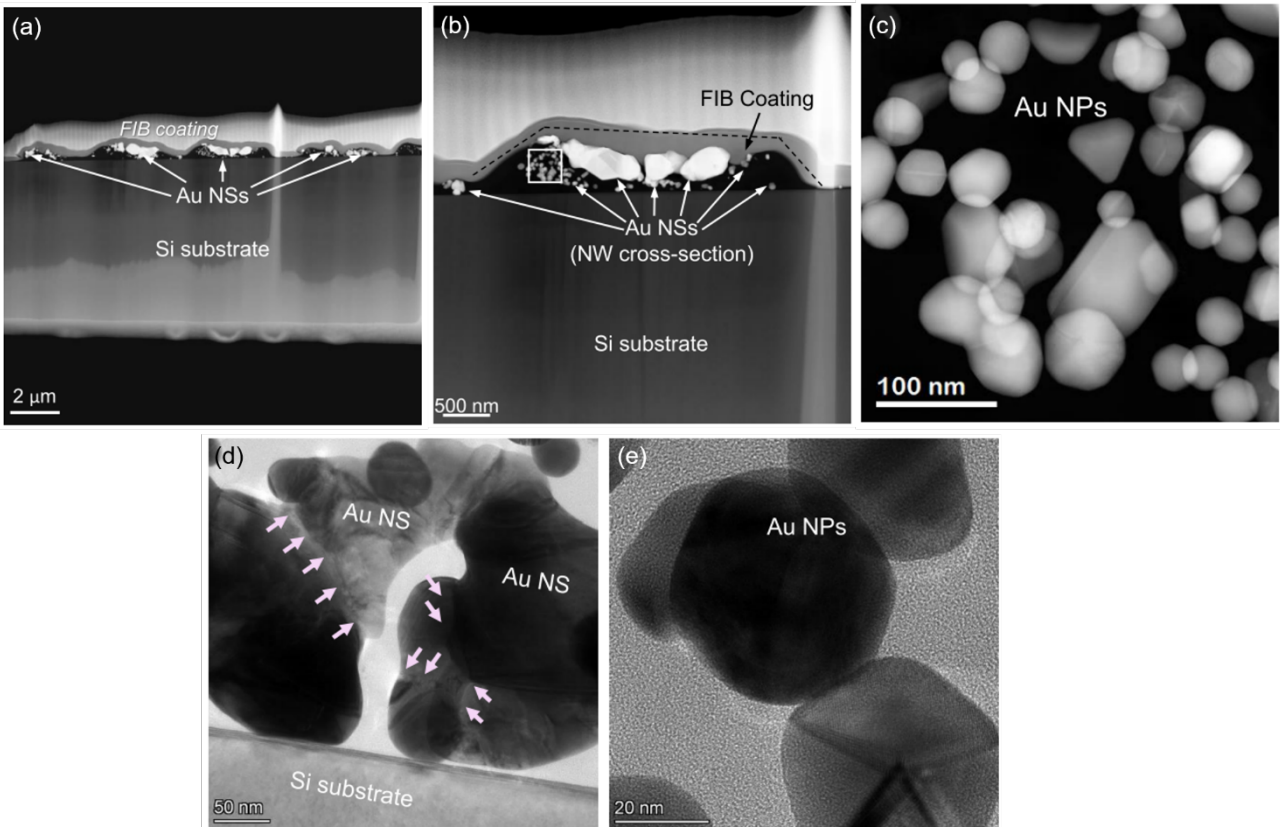


Figure 6.13 (a), (b), (c) HAADF and (d), (e) HRTEM images of the cross section of different AuNSs made with a LP = 100 mW and ET = 150 ms after TP-DLW. The first step of the growth before the second HAuCl₄ bath, the autocatalytic one, can be observed in these images. HAADF images provide Z-contrast indicating that areas with heavier elements are those containing AuNPs. (b) and (d) show that some of the AuNSs are physically deposited onto the Si substrate surface, likely due to a stochastic heterogeneous nucleation event. Arrows in (d) indicate merging regions: TP-DLW is able to create larger structures by the coalescence of smaller individual AuNPs, leading to polycrystalline, highly faceted AuNSs. Different shapes of individual AuNPs (decahedral, pentagonal bipyramid) are shown in (c) and (e).

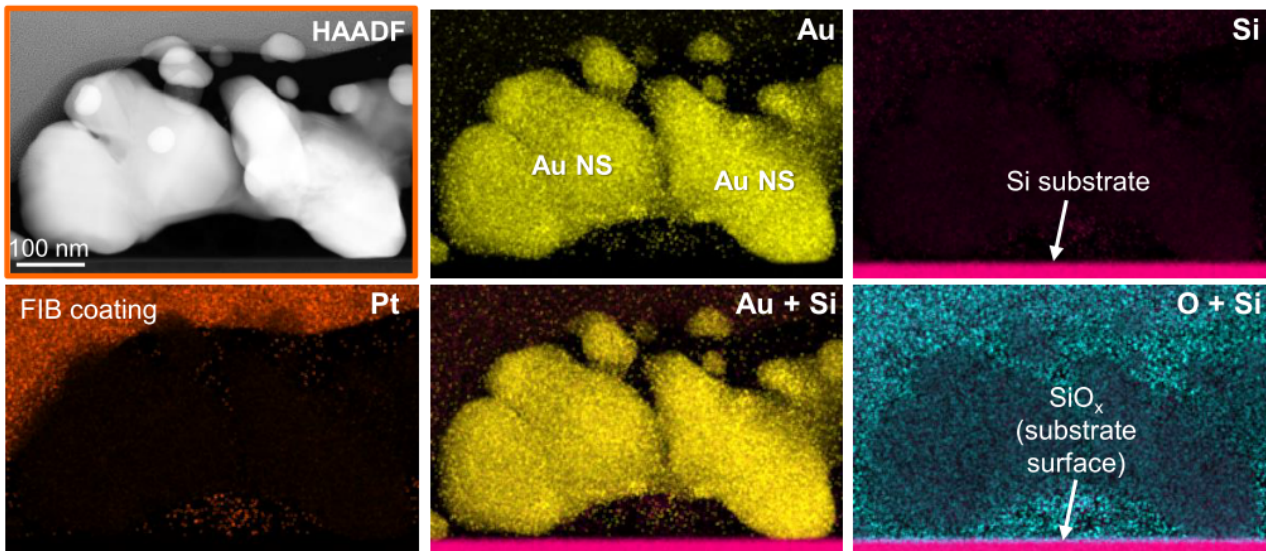


Figure 6.14 HAADF image and EDX maps of AuNSs made with a $LP = 100 \text{ mW}$ and $ET = 150 \text{ ms}$. Au, Si, Pt and O signals are displayed in yellow, magenta, orange and cyan, respectively. AuNSs consist of solely AuNPs, which are able to self-assemble into larger micron-sized clusters, without oxidized species, precursor residues or other impurities. EDX also shows a thin SiO_x native layer at the substrate surface ($\sim 2 \text{ nm}$ thick).

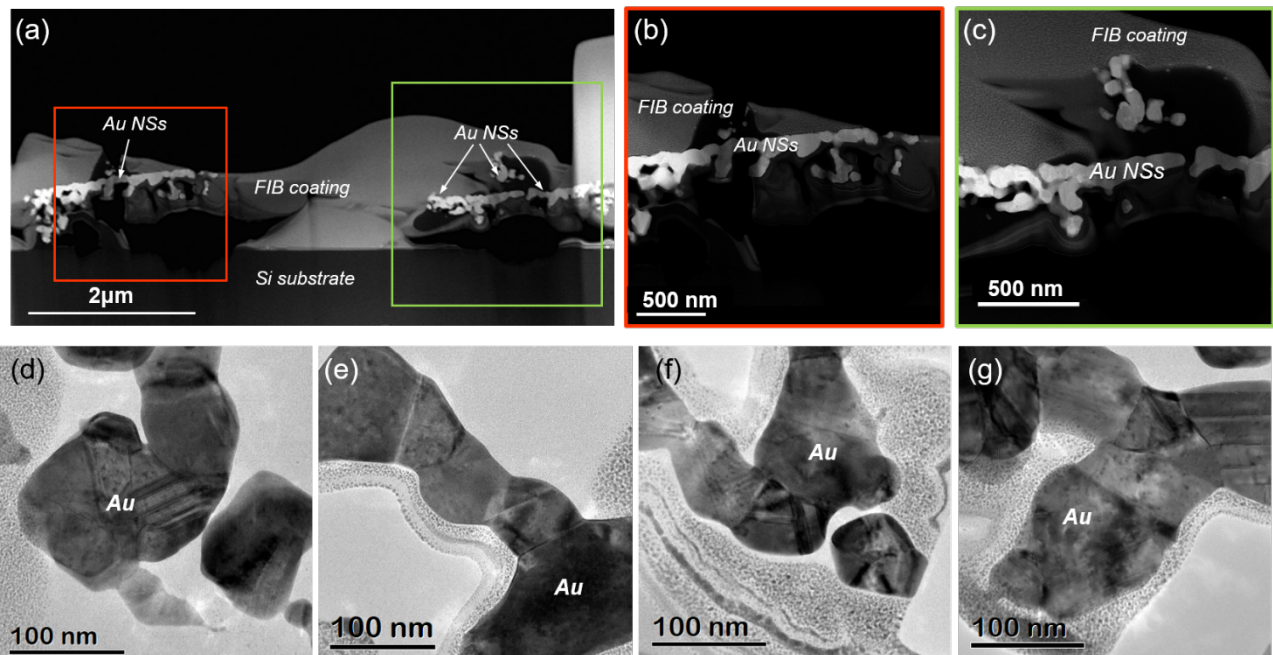


Figure 6.15 (a-c) STEM after FIB cut and (d-g) TEM images of the cross section of different AuNSs made with a $LP = 100 \text{ mW}$ and $ET = 150 \text{ ms}$ and the second immersion in a $10^{-2} \text{ M H AuCl}_4$ solution for 30 min. After the bath, individual AuNPs are not appreciated, in fact (d-g) they have been merged by their facets and exhibit a higher polycrystalline morphology.

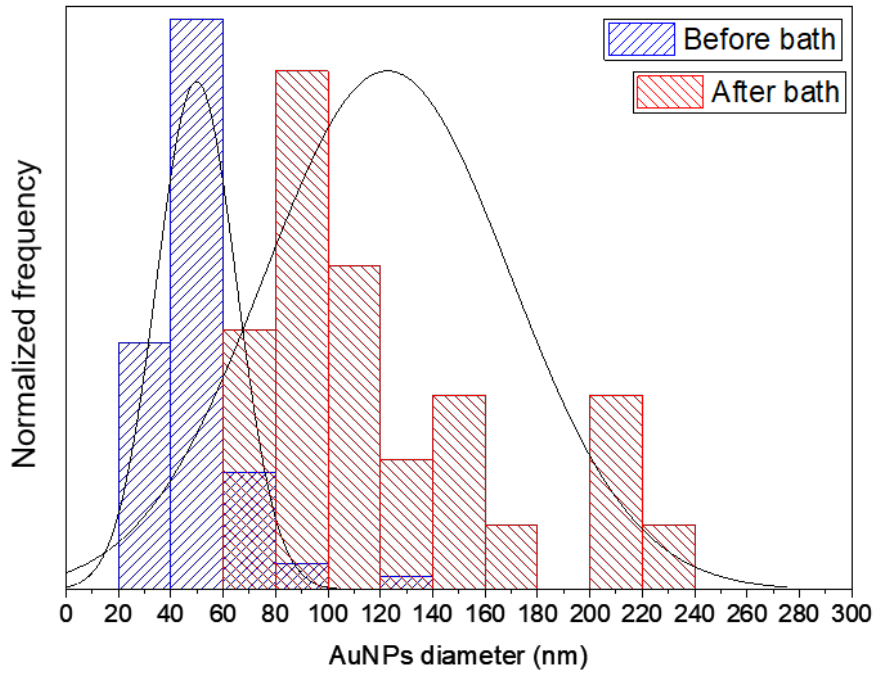


Figure 6.16 AuNPs size distribution after TP-DLW and immersion in deionized water (blue, $N = 75$) and after immersion in a 10^{-2} M HAuCl_4 bath for 30 min (red, $N = 27$). Gaussian distribution before and after the bath evidence the growth of the AuNSs. Quantitative analysis for AuNPs sizes shows that they range from 50 ± 11 nm to 123 ± 35 nm and a significant increase in the AuNSs size after bath is observed.

6.4.3. AuNPs growth kinetics: estimation of the amount of Au

Based on the TEM results presented, an estimation of the AuNPs growth kinetics was done. It was assumed that the HAuCl_4 is completely dissociated and, during the exposure all the ions present in the voxel are reduced to metallic atoms instantaneously.

The maximum theoretical amount of Au that can be reduced depends on the concentration of gold precursor (C) and the volume of the voxel size (V). In our experimental conditions, for a concentration of 10^{-2} M and, assuming a spherical voxel size of 300 – 1000 nm diameter:

$$n_{\text{theoretical}} = C \cdot V = C \cdot \frac{4\pi}{3} r^3 = 2.7 \pm 2.5 \cdot 10^{-18} \text{ mol}$$

The average AuNPs sizes after TP-DLW and after immersion in a HAuCl_4 bath for 30 min were experimentally calculated from TEM images assuming spherical particles. Average diameters calculated were 50 ± 11 nm to 123 ± 35 nm, respectively.

To obtain the amount of Au, it was assumed that AuNPs contain only Au, hence, they possess an atomic weight, $A = 196.97$ g/mol and a density, $\rho = 19.32$ g/cm³.

$$n(\text{mol}) = \frac{m}{M} = \frac{\rho \cdot V}{A} = \frac{4\pi \cdot \rho \cdot r^3}{3 \cdot A}$$

Thus:

$$n_{TP-DLW} = 7.2 \pm 3.9 \cdot 10^{-18} \text{ mol}$$

$$n_{2nd \text{ bath}} = 1.18 \pm 0.83 \cdot 10^{-16} \text{ mol}$$

This value has to be considered as the upper limit for the reduced ions, as the HAuCl₄ dissociation constant along with the probability to induce the proper electronic transitions should be considered. Afterwards, the growth occurs via autocatalytic reaction^{15,16}, until it is stopped by the first washing bath in ultrapure water. From the AuNPs distribution in **Figure 6.16**, it can be estimated the number of Au moles after 10 s growth (i.e. the assumed lag between laser exposure in TP-DLW and removal of the Au³⁺ ions) and after 30 min of a second immersion in a bath containing 10⁻² M HAuCl₄. Values of $(7.2 \pm 3.9) \times 10^{-18}$ mol and $(1.2 \pm 0.8) \times 10^{-16}$ mol were obtained, respectively. The amount of Au obtained after DLW printing is slightly higher value than the theoretical Au amount calculated from the voxel size. Formally, this difference can be ascribed to the autocatalytic growth reaction, largely dominant over the starting AuNSs coalescence. Hence, it can be concluded that in these experimental conditions, AuNPs sizes increase around 30 nm diameter during the first 10 s after the exposure. Diffusion time in the range 10⁻¹ - 10⁰ s/μm are typical for these systems, much shorter than the unavoidable lag between the exposure and the first bath in deionized water. As a consequence, even making this lag as short as possible, possibly by the use of a microfluidic setup, considering the characteristic water diffusion time in the hydrogel matrix, it cannot be shorter than typically 1 s. This establishes a limit to the obtainable smallest AuNPs size with this technique. After the second bath, an increase of up to two orders of magnitude is observed. This evidences the significant contribution of the autocatalytic reaction to the growth of the AuNSs, largely dominant over the starting AuNPs coalescence.

6.4.4. Study of the range of HAuCl_4 concentrations valid for TP-DLW

Different experiments are carried out acting on the amount of the gold precursor in the solution to study the variation of the size of the seeds depending on the concentration of HAuCl_4 .

After the optimization of the parameters for 10^{-2} M HAuCl_4 , as already discussed in the previous section, we decided to compare the results for the same treatment, repeating the same conditions for other concentrations ranging from 10^{-3} to 10^{-1} M.

Different samples could be successfully printed for 10^{-3} M HAuCl_4 , although a very good resolution nanopatterning could not be achieved. This happened especially when printing in the continuous mode (not pulsed, e.g. when printing lines) and the objects require few micron-separated lines. In fact in this case if thermal effects are not also present, the concentration is too low to activate the photoreduction (**Figure 6.17**).

The advantage to use lower concentrations is of course the possibility to obtain very small nanoparticles, as visible in the **Figure 6.18**, where AuNPs with diameters below 30 nm are observed. However, at this concentration, as expected, less AuNPs are produced and not all the objects are well defined and visible during the optical microscope observation. In **Figure 6.18**, for instance, it is possible to see structures that at naked eye are not evident while in **Figure 6.19** in the optical microscope images are present structures with faint traces especially at the border where the solution is less concentrated.

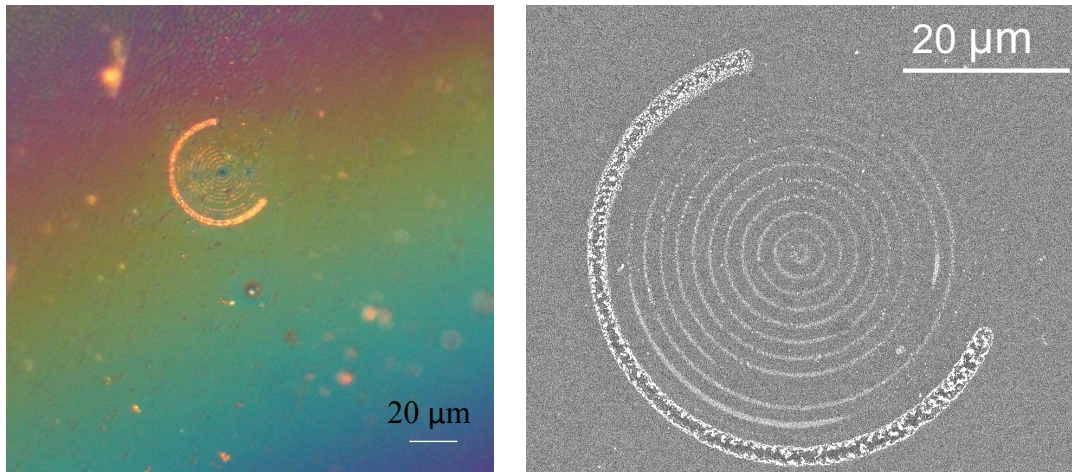


Figure 6.17 *Same circular concentric structure at optical (left) and scanning electron (right) microscope. It is evident that not all the circles are well defined after the printing due to the low and non-uniform concentration ($C \sim 10^{-3} M$)*

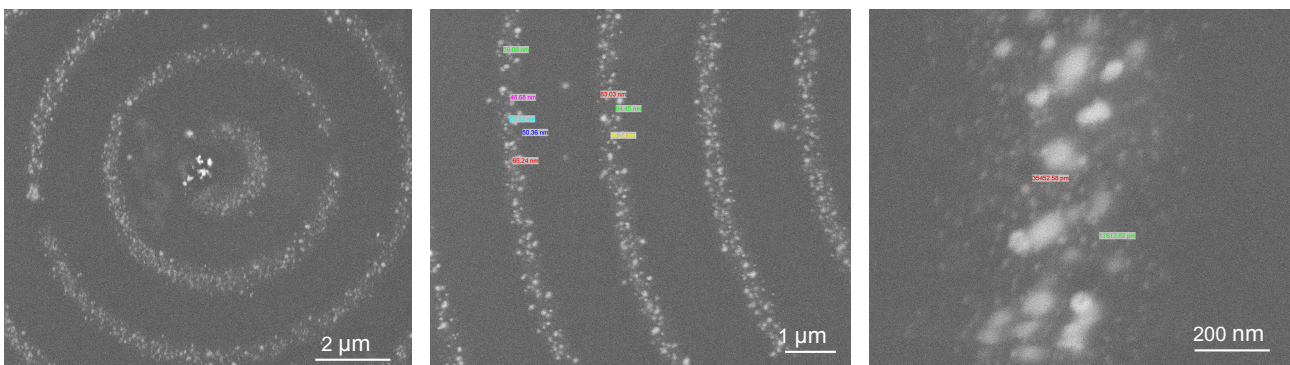


Figure 6.18 *SEM images of a circular concentric structure, not visible with the optical microscope. It is possible to see the very little size of the nanoparticles down to 30 nm, due to the low concentration ($C \sim 10^{-3} M$).*

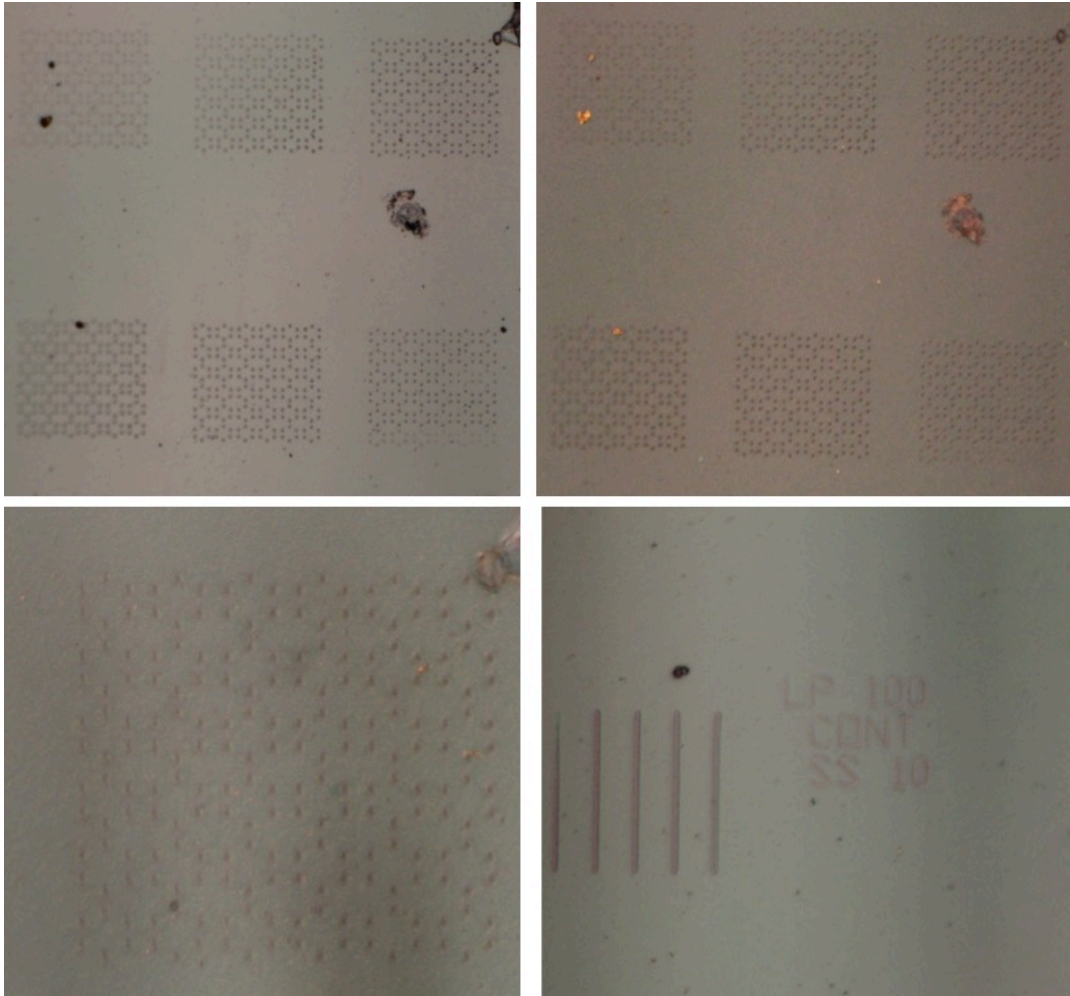


Figure 6.19 *Optical microscope images (the last three between crossed polarizers) of linear and honeycomb nanopatterns. Due to the low concentration ($C \sim 10^{-3} M$) especially at the borders of the honeycomb structure the isolated points are not well defined. The diameter of the single spot is around $3 \mu m$ and the lines are $20 \mu m$ long (printing parameters: $SS = 10 \mu m/s$, $LP = 100 mW$).*

When the experiments were repeated using concentrations of $10^{-1} M$ $H AuCl_4$, the structures formed by TP-DLW are visible with the optical microscope. These structures are inhomogeneous and full of gold precipitates, meaning that the concentration used is too high and we assume the value as the upper limit of the range of suitable concentrations of the gold precursor.

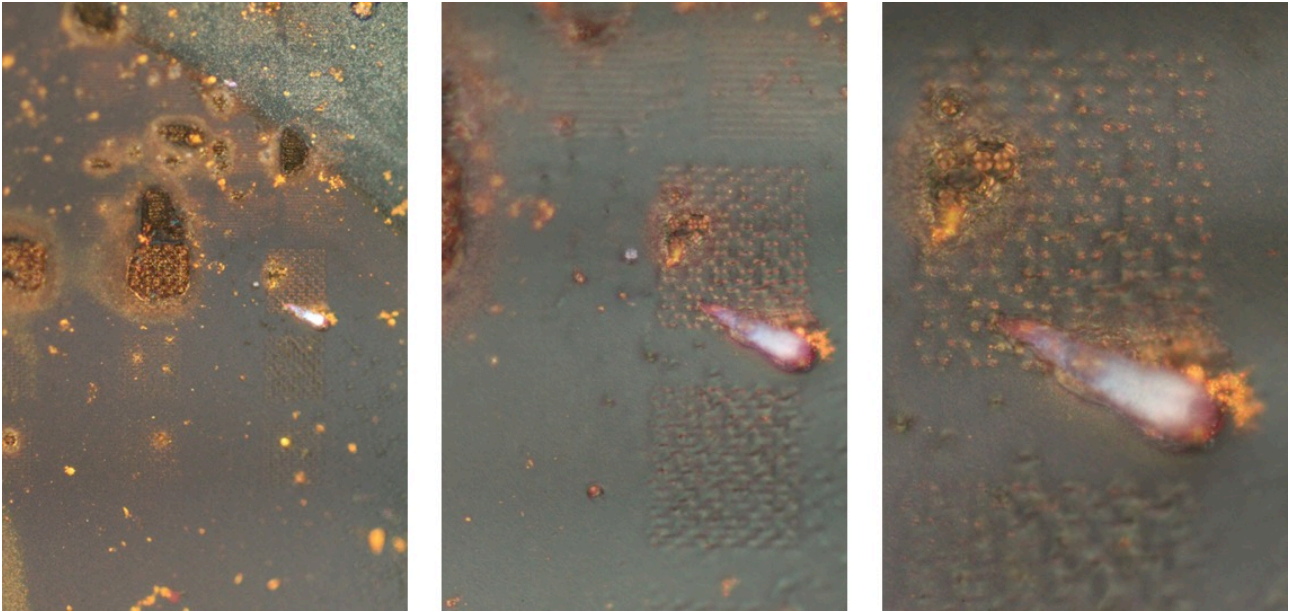


Figure 6.20 *Optical microscope images of the AuNSs using a concentration of 10^{-1} M HAuCl_4 . The structures are inhomogeneous and precipitates and gradients of concentration are also present.*

The situation gets worse with the second bath in the gold solution. The nanopatterns become very thick and blurred, as visible in **Figure 6.20**. For this case, already after ten minutes of bath, changes are visible to the naked eye. The structures look like more filled and defined and the color turns to red because of the gold plasmon.

6.4.5. Study of the range of times for the growth process

Once the optimal HAuCl_4 concentration has been set, 10^{-2} M, it is possible to tune the duration of the second bath in the gold precursor to estimate the variation of the size of the gold nanoparticles depending on the time.

Different tests were done after immersion of the samples in a 10^{-2} M HAuCl_4 for 1, 2 and 3 h. These times were chosen since the effective and visible growth occurs after an hour (**Figure 6.21** and **Figure 6.22**).

After one hour of treatment it is evident that the AuNPs are well spread all over the sample and little in size. When the time increases, the AuNPs tend to aggregate especially in the center of each honeycomb nanopattern (**Figure 6.23** and **Figure 6.24**).

Quantification of the AuNPs formed after different times in the second bath is presented in **Figure 6.24** and **Table 6.1**. They show that the growth kinetics of the AuNPs follow a linear pattern with time, at least in the ranges of times studied, increasing their diameter from 33 to 91 nm for the smaller nanoparticles and up 300 nm for the bigger ones.

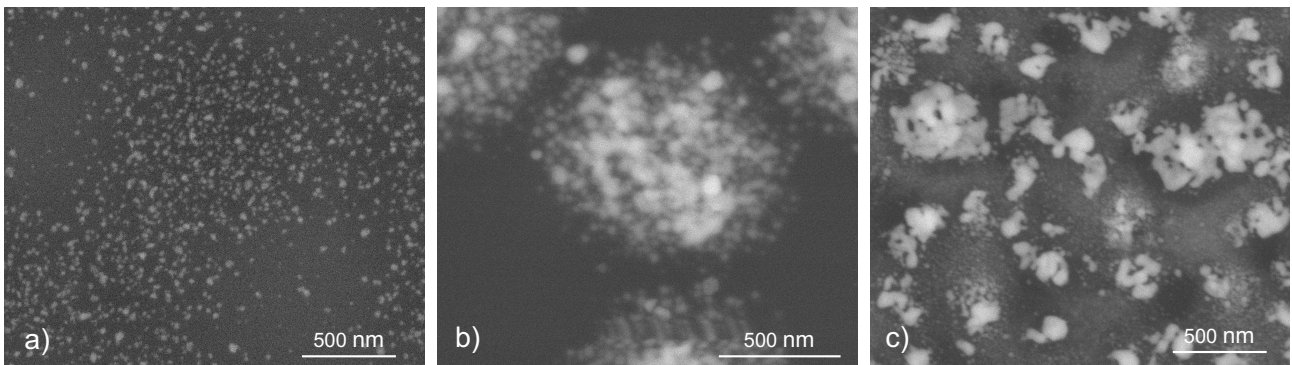


Figure 6.21 SEM images of the gold nanoparticles for the three treatments after that HAuCl_4 concentration has been set at 10^{-2} M: 1 h (a), 2 h (b) and 3 h (c). It is observable that the nanoparticles tend to cluster with time and the smaller ones grow up 90-100 nm while the bigger ones grow up 300 nm.

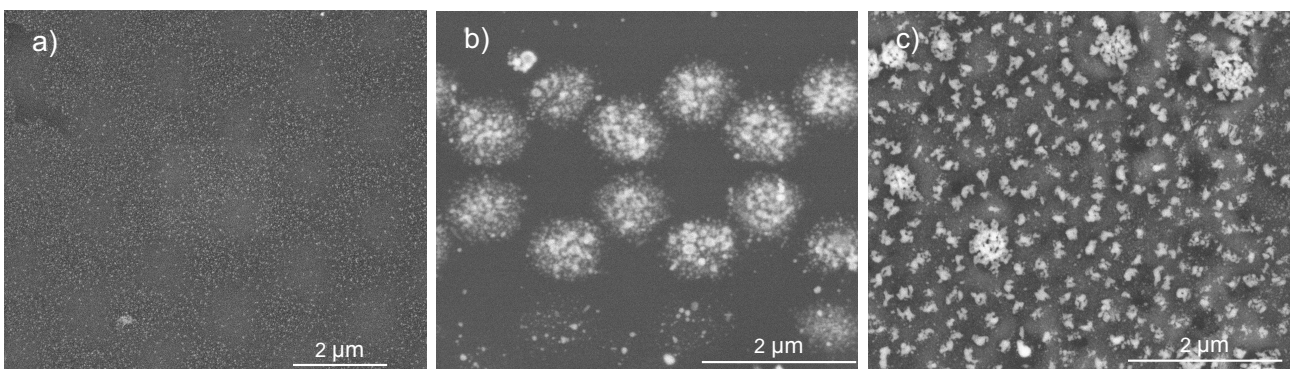


Figure 6.22 Nanopatterns rich in gold nanoparticles for 1 hour (a), 2 hours (b), 3 hours (c) treatment. It is evident that with increasing time, nanoparticles clusterize and diffuse.

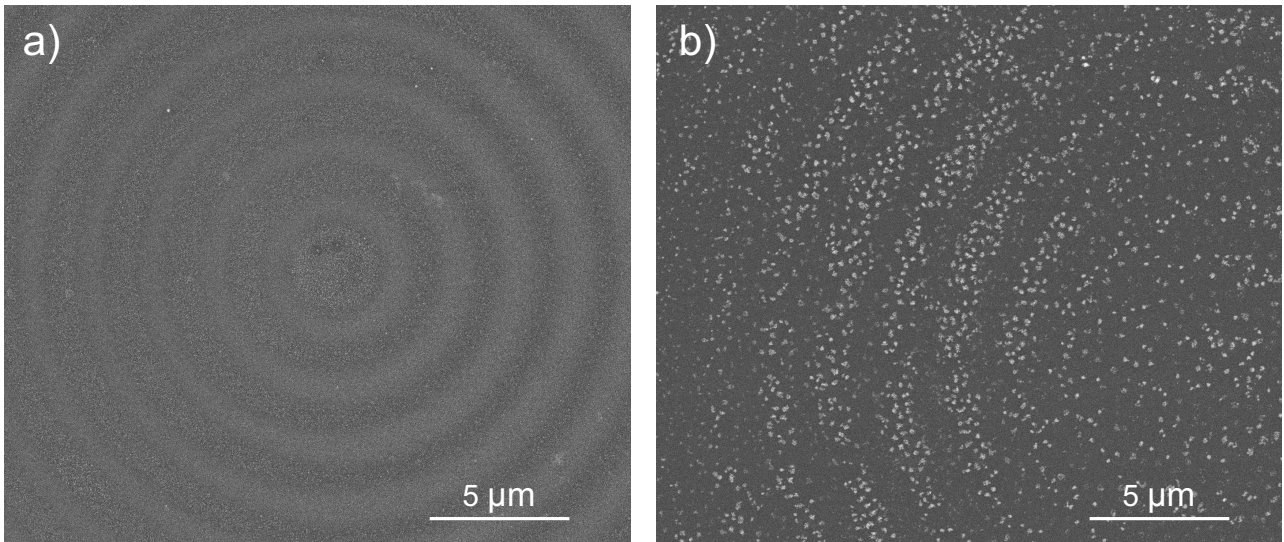


Figure 6.23 Nanopatterns after 1 (a) and 3 (b) hours of treatment.

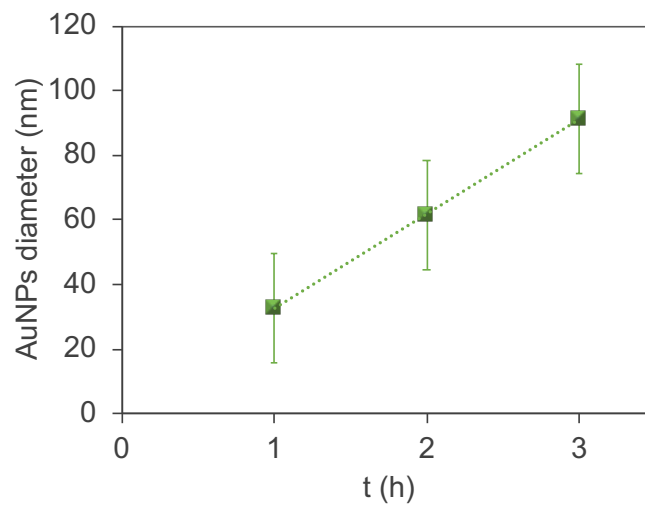


Figure 6.24 Average diameter of the different AuNPs printed as a function of the duration of the bath.

Table 6.1 Average values and standard deviation of the diameter of the gold nanoparticles after one, two and three hours.

<i>t(h)</i>	<i>AuNPs diameter (nm)</i>
1	33 ± 8
2	62 ± 14
3	91 ± 17

6.4.6. IP-S and H_{Au}Cl₄

Other attempts are done combining the two techniques of photopolymerization and photoreduction.

The first one is performed using IP-L 780 and another NanoScribe GmbH photoresist, IP-S, for the part of photopolymerization and the usual gold precursor H_{Au}Cl₄ for the part of photoreduction.

Between the commercial photoresist employed for the TPP, IP-L is preferred (**Figure 6.25**), analogously to what has been tested by Qin Hu et al.^{22,23}.

The TP-DLW system with the NIR light triggering the two processes simultaneously, is used.

A 10⁻² M concentration of gold precursor is enough to promote the non-linear optical process and the photopolymerization of the photosensitive resin.

In fact, when a drop of mixture is loaded directly on the glass substrate which is composed of resist and gold salt, the near-infrared femtosecond laser beam is focused into the mixture allowing the polymerization of the resist and the reduction of the metal salt.

In this way, both polymer and gold nanoparticles are formed simultaneously. Complex 2D and 3D structures are fabricated by scanning the laser in three dimensions (**Figure 6.26**) and this protocol paves the way to future research in this direction.

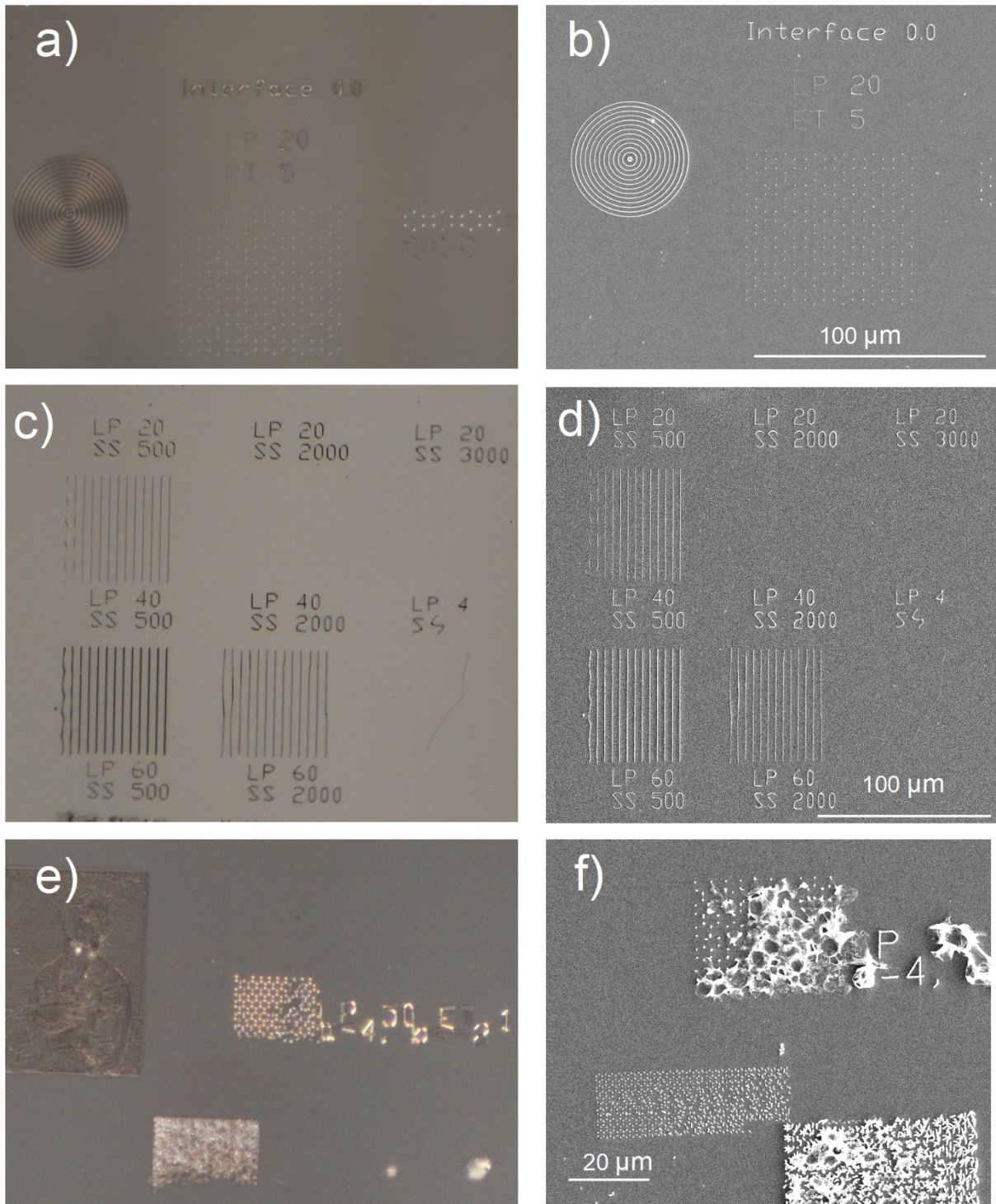


Figure 6.25 Optical (a, c, e) and SEM (b, d, f) images of different nanopatterns (circles, lines and isolated points) of different dimensions, where it is visible the red coloration of gold for optical and bright white for SEM.

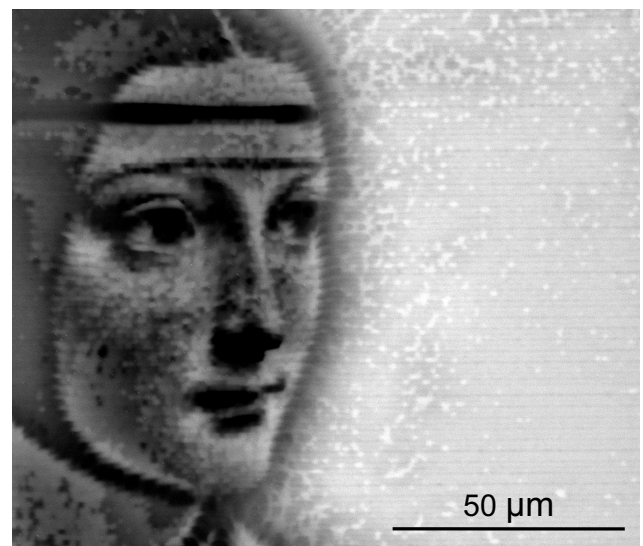
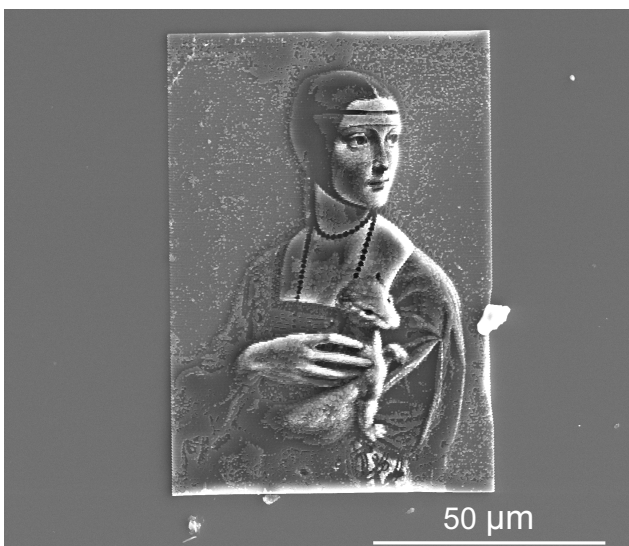


Figure 6.26 *Optical (up) and SEM (down) images of the Leonardo Da Vinci's "Lady with an Ermine" reproduced at the microscale with the simultaneous photopolymerization-photoreduction technique to allow the entrapping of the gold nanoparticles also for embossed pictures ($z \neq 0$). Thanks to G.Lio for modeling the lady²⁴.*

7. Additive Manufacturing of SiO₂ NWs nanocomposites via TP- DLW

In this chapter we talk about the Two-Photon Direct Laser Writing (TP-DLW) used for the nanofabrication of fiber-reinforced polymer nanocomposites by using Silica Nanowires (SiO₂ NWs) as nanofillers. The tailored choice of the materials allows to achieve high resolution of the objects created taking advantage of the matching of the refractive indices of the glassy filler and the polymeric matrix, even with high loads of the filler.

Silica nanofillers are already employed to improve the mechanical and structural properties also to an industrial level, insulation properties and thermal stability producing for example foams in combination with epoxy resins or PMMA.

Three different printing configurations can be done thanks to the use of silicon chips on which the SiO₂ NWs are grown as fabrication substrate. First, they can be effectively used as an adhesive layer when the laser beam is focused at the interface with the silicon substrate. Second, as a sacrificial layer, when the laser beam is focused inside the SiO₂ NWs layer. Third, only the outer frame of the object (shell) is printed, so the SiO₂ NWs act as internal skeleton of the structure (scaffold), in the so-called shell & scaffold printing strategy.

Mechanical characterization is performed to analyze and compare the nano-hardness and elastic modulus of the pristine photoresist with that of our composites to test the capability to 3D-print performing solid objects with high filling volume fractions. This can make the proposed technique well-suited for applications which require higher mechanical performance, as in advanced microfluidics or micro-mechanics extending the range of TP-DLW processable materials to possible application to nanotechnologies and industry.

The physical processes behind this technology, the technology itself and the used materials and equipment are described in **Chapter 4**.

7.1. Fabrication of FRPN via TP-DLW on SiO₂NWs substrate

With the aim to enhance the mechanical properties of the objects created by TP-DLW, the commercial photoresists were combined with structural SiO₂ NWs nano-fillers (**Figure 7.1**). These two materials possess a comparable refractive index ($n \approx 1.5$), thus allowing a coarse matching in their optical properties^[1,2].

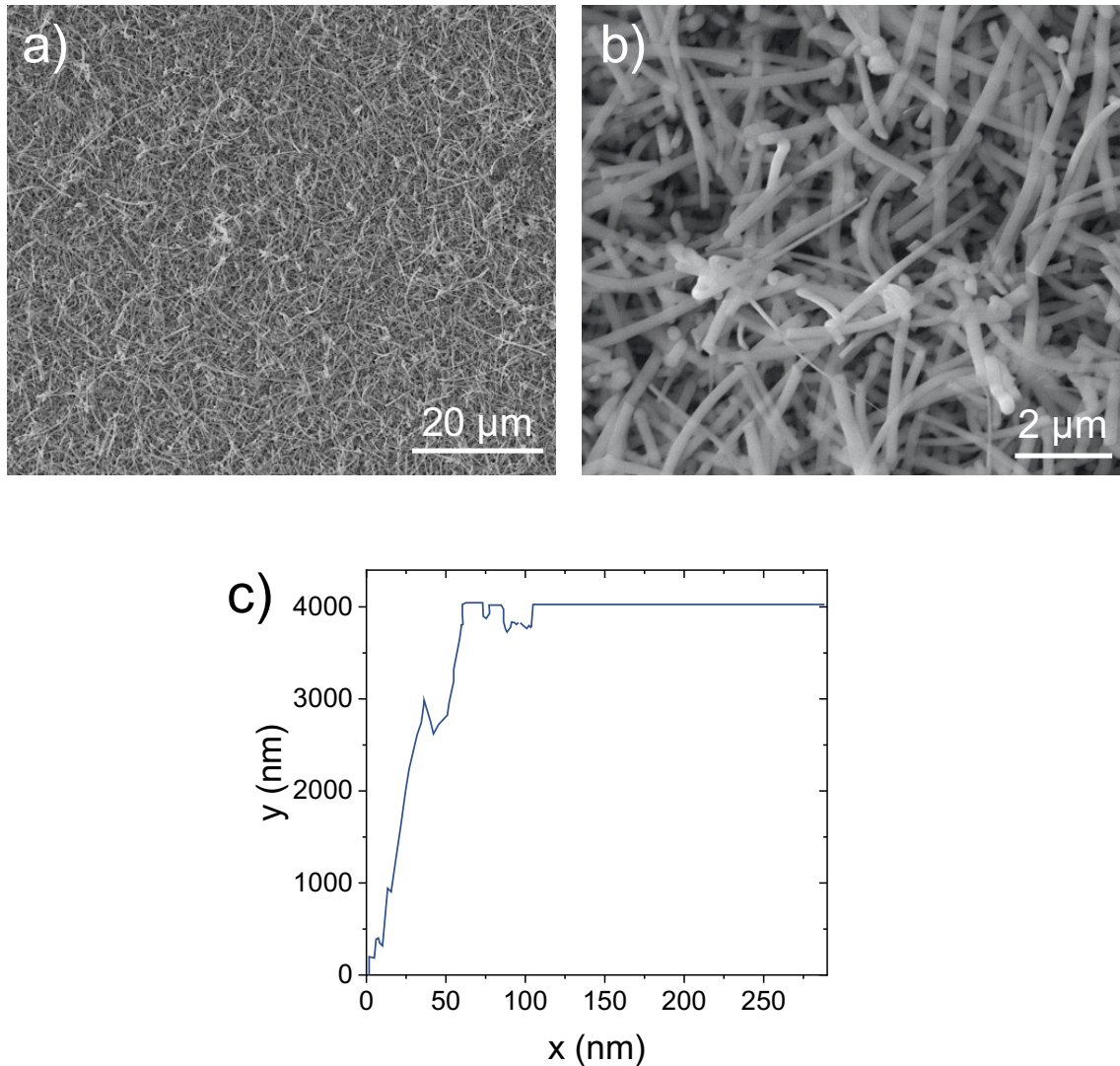


Figure 7.1 a), b) SEM images of SiO₂ NWs grown on Si substrate; in b) it is possible to distinguish the NWs with a homogenous distribution of diameters in the range of 30-300 nm; c) Profilometer measure of the thickness of the SiO₂ NWs layer on the Si substrate. Total thickness was estimated to be of 8 μm since there is a drift of 4 μm.

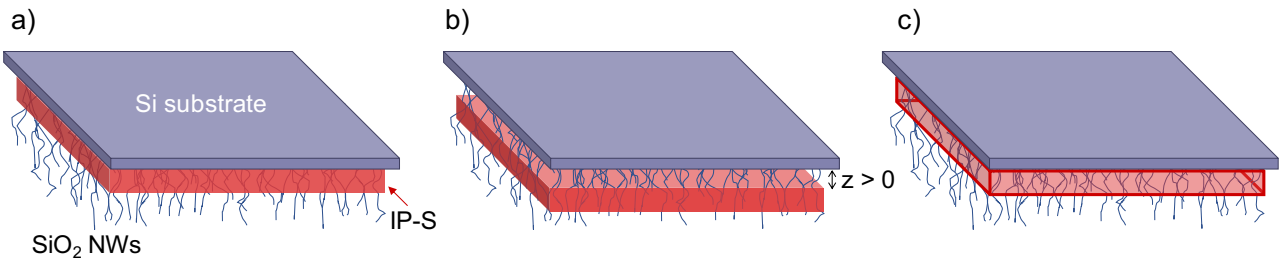


Figure 7.2 Objects were printed via TP-DLW with three different approaches: a) the first layer is printed at the interface with the Si for adhered structures to the substrate; b) the first layer is printed leaving a gap with the Si substrate ($z > 0$); in this case, the object can be detached after the etching of the SiO₂ between the resin and the Si substrate, which acts as a sacrificial layer; c) same case as a) but printing only the outer frame of the structure (shell); in this case, the SiO₂ NWs act as internal scaffold (shell & scaffold approach).

The reduced scattering resulting from the refractive index matching between the SiO₂ NWs and the resist, allowed the polymerization at a depth of about 8 μm (through the layer of NWs, see **Figure 7.1c**), without affecting the voxel typical size. The objects were printed following three different alternatives, as depicted in **Figure 7.2**.

Some of these structures observed at the optical microscope are presented in **Figure 7.3**.

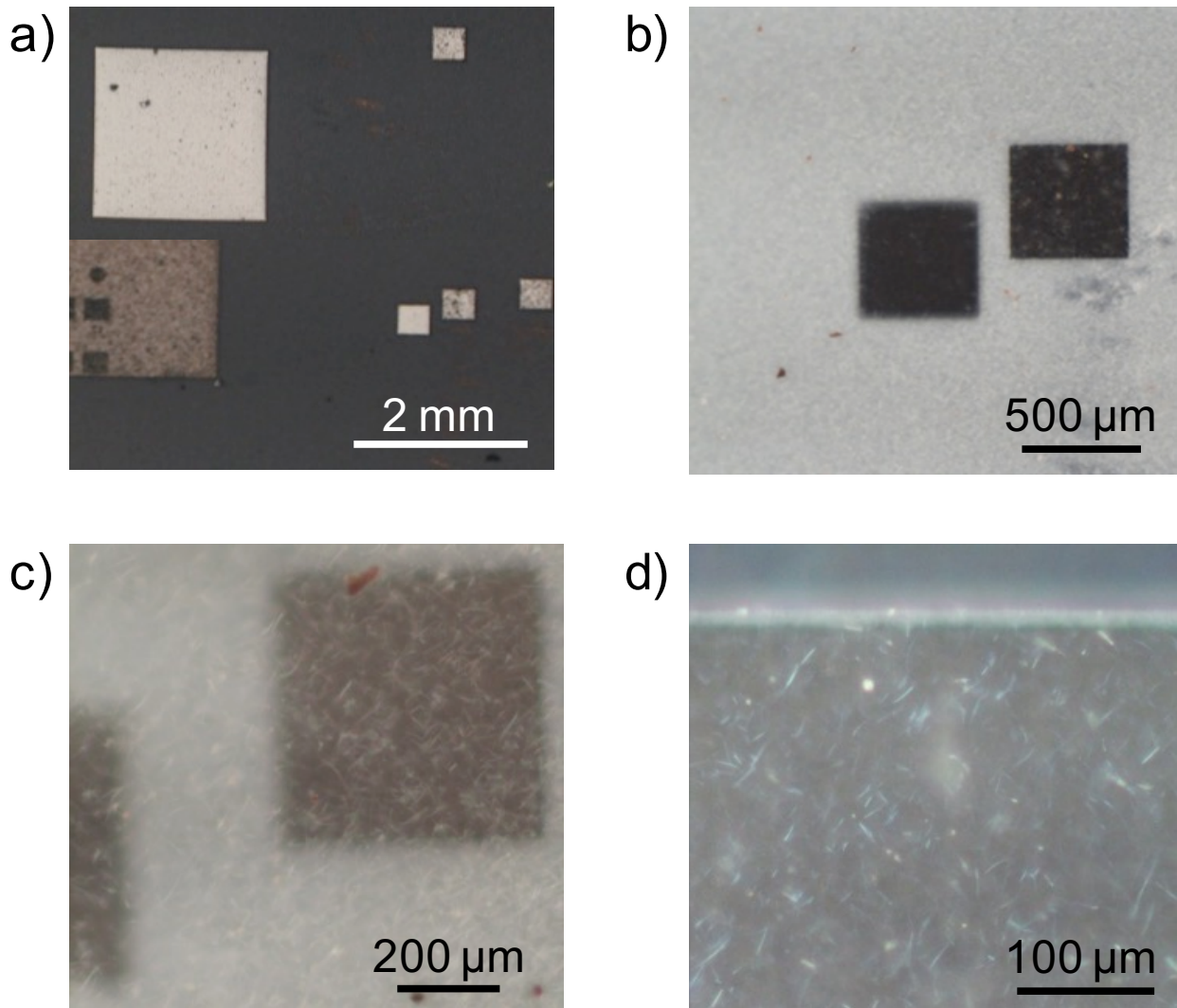


Figure 7.3 *Optical microscope images of the different kinds of printed parallelepiped structures are shown: a) small ($500 \times 500 \times 2.0 \mu\text{m}^3$) and big ($2000 \times 2000 \times 1.5 \mu\text{m}^3$) parallelepipeds printed through the NWs layer and their magnifications are visible under reflected light. Different color underlines the solid and only shell structures: the printed objects appear brighter than the Si background. In the first magnification b) it is possible to notice the different height of the 3D objects printed at two different z-positions, adherent at the interface with the Si wafer (adhesive layer) and anchored to the SiO_2 NWs only. The polymer appears darker than the Si substrate and the SiO_2 NWs. It can be clearly appreciated that the object printed on the left is out of focus. This is the first evidence that the presence of a SiO_2 NWs layer permits printing at different heights as depicted in Figure 3a and Figure 3b. In c) and d) a closer look at one of the samples where it can be clearly observed that the SiO_2 NWs are well-embedded in the polymeric matrix.*

7.1.1. HF etching of FRPN

The objects built directly adhered to the Si substrate (**Figure 7.2a**), were not detached after the washing steps with PGMEA and IPA. In this case, the HF buffer rapidly etches the exposed SiO₂ NWs, whereas the polymeric matrix adhered to the Si substrate protects those embedded. In this case, it was checked that the objects are firmly kept by the SiO₂ NWs layer after different immersion times in the etching solution, proving that they are permanently bonded to the Si substrate. The effect of the HF buffer was studied by profilometry. **Figure 7.4** shows that the printed parallelepiped remains adhered to the Si substrate after 15 min of etching. The dimensions of the object are not substantially altered before and after the etching process with the HF buffer. However, the roughness decreases significantly due to the removal of the SiO₂ NWs exposed to the etching solution. These results are supported by SEM analysis. **Figure 7.5a** shows a parallelepiped after 15 min of etching with the HF buffer. In **Figure 7.5b** it can be appreciated that some SiO₂ NWs remain in the surface, indicating that this time is sufficient to remove the excess of SiO₂ NWs but not to penetrate below the resin to eliminate those embedded. However, after 30 min of etching, the surface of the parallelepiped appears flat and SiO₂ NWs are completely absent (**Figure 7.5c**). Hence, it has been estimated that 15 min is the correct etching time to completely remove the exceeding SiO₂ NWs without altering the FRPN structure.

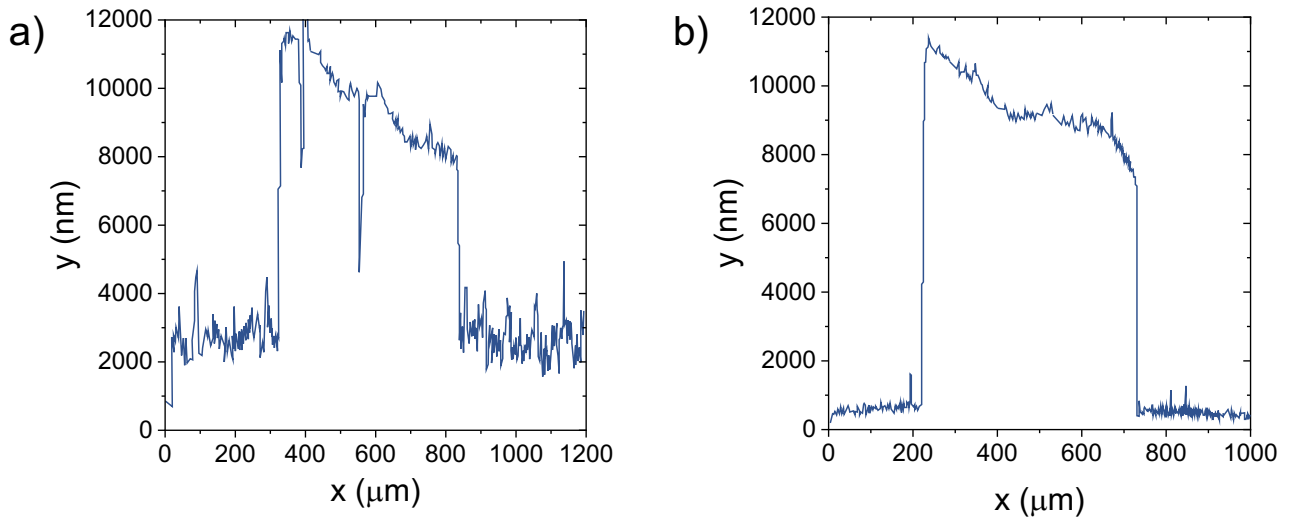


Figure 7.4 Profilometer measurements of an adhered structure at the SiO₂ NWs interface a) before and b) after 15 min immersed in HF buffer. A decrease in the roughness of the surface evidences the successful etching of the SiO₂ NWs

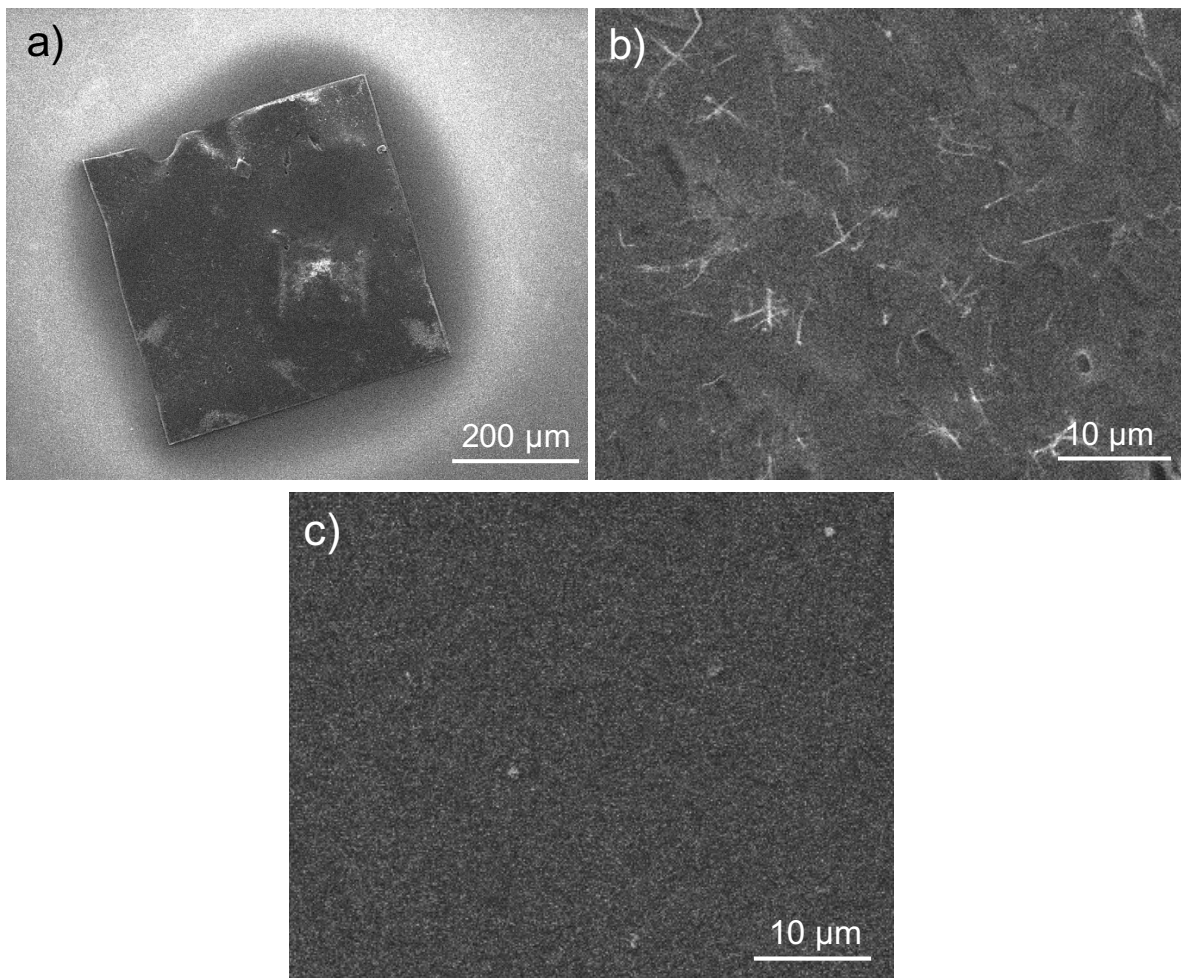


Figure 7.5 SEM micrographs of an adhered structure at the SiO₂ NWs interface after a), b) 15 min and c) 30 min immersed in HF buffer.

Samples printed leaving a 1 μm gap with respect to the Si substrate (see **Figure 7.2b** and **Figure 7.5**): in this case, an etching time of 15 min revealed correct to also dissolve the SiO_2 NWs within the gap by the HF buffer, leaving the created object completely free. In this case, the substrate acts as sacrificial layer that can be removed on demand. It is important to point out that the etching time to eliminate the sacrificial layer could also be tuned by controlling the clearance of the gap and therefore the diffusion kinetics of the HF. The possibility to tune the etching time between the gap and the exposed surface adds a further degree of freedom in the fabrication process in the case of multi-step fabrications.

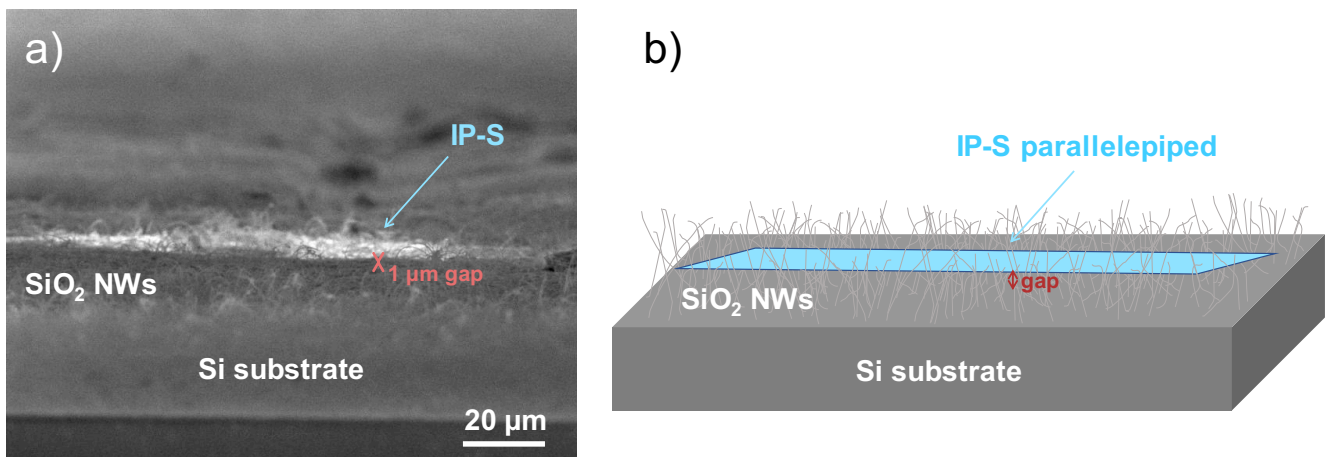


Figure 7.6 a) SEM image of the cross-section of a FRPN showing the gap between the Si substrate and the sample printed with the IP-S resin; b) cartoon depicting a) for clearer interpretation.

7.1.2. Only-shell layer

Hollow structures were also successfully printed according to the shell & scaffold protocol as shown in **Figure 7.2c**. In this case, the object is built as a hollow structure (shell) with the first layer printed at the interface with the Si substrate. **Figure 7.7** shows the profilometry results before and after etching with the HF buffer. As in the case of the solid objects, it can be observed that the structure of the printed shell remains practically unaffected while the high roughness associated to the SiO_2 NWs disappears after 15 min of etching. In this approach, the aim is to etch only the excess of SiO_2 NWs

outside the shell, so the time is expected to be the same as for bulk objects (**Figure 7.2a**). Profilometry results evidence that the SiO₂ NWs are able to provide an internal scaffold with a self-standing structure and proves that the NWs inside the shell remain unaltered. Hence, this strategy can be adopted in TP-DLW when large volumes are needed, reducing significantly the printing times.^[3-7]

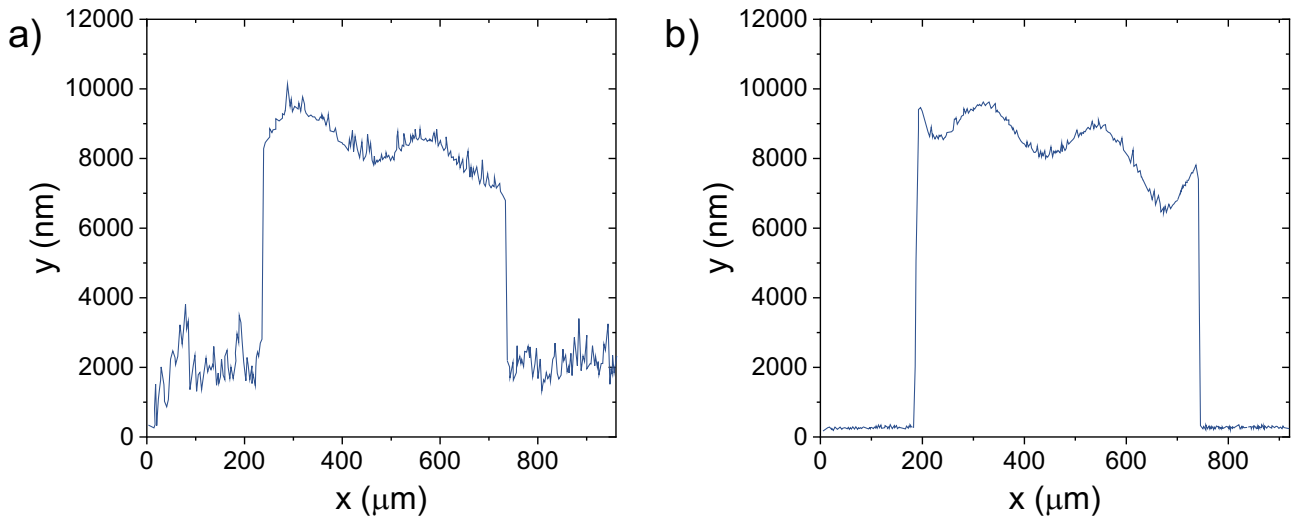


Figure 7.7 Profilometer measurements of an adhered structure at the SiO₂ NWs interface following the shell & scaffold approach a) before and b) after 15 min immersed in HF buffer. The decrease in the surface roughness indicates the successful etching of the exposed SiO₂ NWs.

As it has been proven, the use of SiO₂ NWs grown on chips as fabrication substrate allows the nano-printing of structures in a range of different conditions. The capability to print structures anchored to the nanowires makes unnecessary the condition fulfilment of being exactly at the interface for the correct anchoring of the fabricating object. This would eliminate the necessity of using the sophisticate autofocus system for the interface detection. Instead, it is possible to have an effective range of z heights, determined by the thickness of the nanowires layer, from which the manufacture could start, making the autofocus system redundant.

7.2. Mechanical characterization of the FRPN

Figure 7.8 reports the results of the nanomechanical characterization, as obtained from varying the indentation load P_{\max} between 0.5 and 10 mN. Each data-point in the figure represents the average value with its associated error corresponding to the data obtained from 5 different indentations.

In particular, **Figure 7.8a)** reports the evolution of the Young's modulus (E_{IT}) and of the nano-hardness (H_{IT}) as a function of the indentation load. Results revealed a significant increase in the H_{IT} with the indentation force up to a value of 8 mN. Above this value, it reaches a plateau for higher indentation loads. On the other hand, the E_{IT} remains constant throughout the whole range of indentation loads studied (0.5-10 mN).

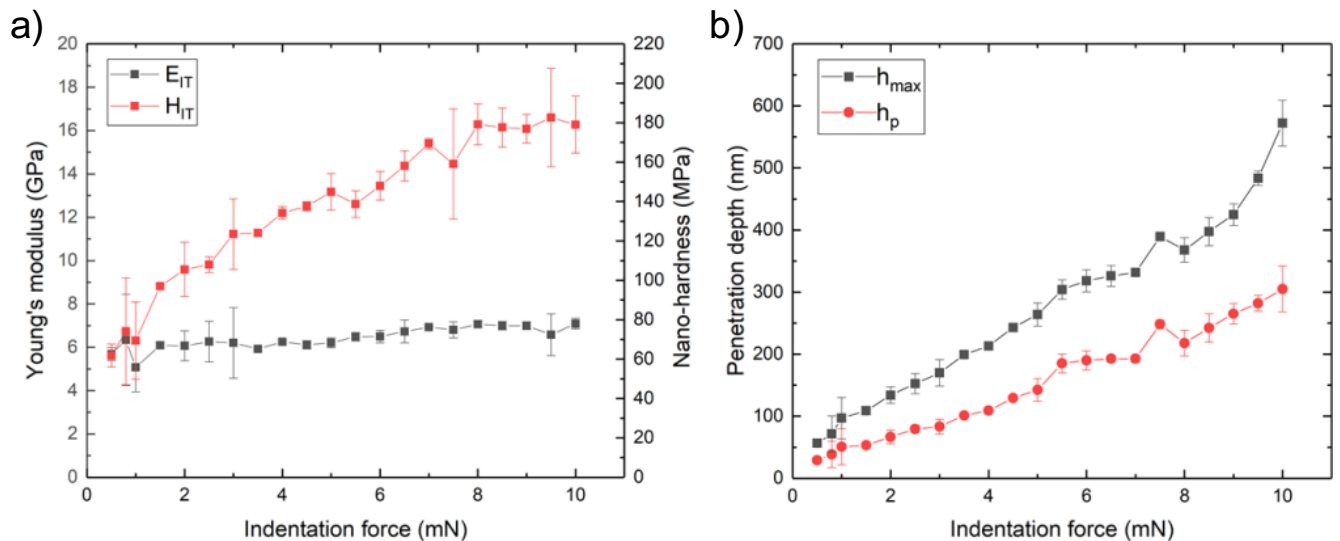


Figure 7.8 a) Young's modulus (E_{IT}) and nano-hardness (H_{IT}) as a function of the indentation load; b) plot of the nano-indentation results for Young's modulus and nano-hardness vs indentation load. Maximum indentation depth (h_{\max}) and residual depth (h_p) as a function of the indentation force.

Nevertheless, as it can be seen in **Figure 7.8b**, the maximum penetration reached (h_{\max}) during the indentation is always below 700 nm, i.e. lower than 10% of the thickness of the nanocomposite. Therefore, it can be concluded that the studied region, either during plastic and elastic deformation, will not be affected by the presence of the Si substrate. More details about these experiments can be found in the Supporting Information.

According to these results, an indentation-load equal to 10 mN was chosen to evaluate the mechanical properties at the nano-scale of the nanocomposite since under these conditions both E_{IT} and H_{IT} are in the plateau region (i.e. maximum values that can be obtained). Then, different nano-hardness measurements were done in a matrix of 10 x 8 of individual indentation points with 100 μm spacing between each indentation, and with a holding time of 10 s. An example of one of these indentations is shown in **Figure 7.9**.

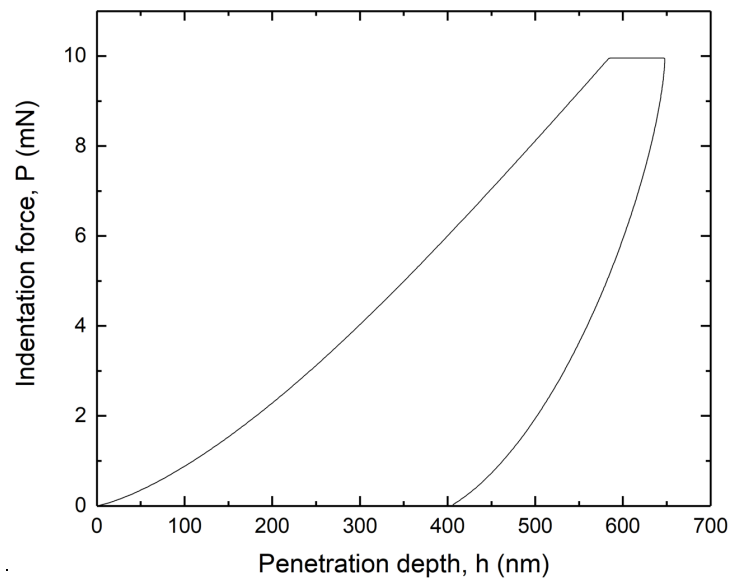


Figure 7.9 Indentation load vs penetration depth curve for the FRPN fabricated in this work.

The indentation tests revealed that the FRPN mechanical properties are characterized by a value of Young's modulus and nano-hardness equal to 8.63 ± 0.78 GPa and 120.06 ± 10.77 MPa respectively. With the purpose to evaluate how the use of SiO_2 NWs substrates allows enhancing the mechanical properties of the obtained material, nano-indentation experiments were carried out also on the bare polymeric matrix. The indentations tests showed a marked reduction of both Young's modulus and nano-hardness. In fact, while the Young's modulus of the polymeric matrix is equal to 1.94 ± 0.10 GPa the nano-hardness reaches a mean value of 33.47 ± 0.35 MPa, as resumed in the **Table 7.1**. These results evidence that FRPN exhibit significantly enhanced mechanical properties comparing to the bare polymer, with an increase of approximately 4 times in the Young's modulus and nano-hardness

values. Therefore, these materials are promising for structural applications in the nanotechnology sector that require higher structural yields, such as in microfluidics.

Table 7.1 *Comparison of Young's modulus and nano-hardness values for bare polymeric resin (IP-S) and the FRPN loaded with SiO₂ NWs printed via TP-DLW in this work.*

	Young's modulus (GPa)	Nano-hardness (MPa)
IP-S	1.94 ± 0.10	33.47 ± 0.35
FRPN	8.63 ± 0.78	120.06 ± 10.77

7.3. SiO₂ NWs and HAuCl₄

Another attempt to use the protocol realized in this work regards the employment of a different substrate instead of typical glass or silicon substrate. The new substrate is constituted of a carpet of SiO₂ NWs grown on silicon layer.

In this way we have the possibility to embody gold nanoparticles, created with the photoreduction, in the tangle of SiO₂ NWs. The idea can pave the way to an alternative method for the creation of gold nano-antennas and nanowires decorated with metal nanoparticles. In fact, as we can see already from optical images in **Figure 7.10 b-e**, nanoparticles and clusters of them are placed along the lines of the nanopatterns and around the isolated points structures.

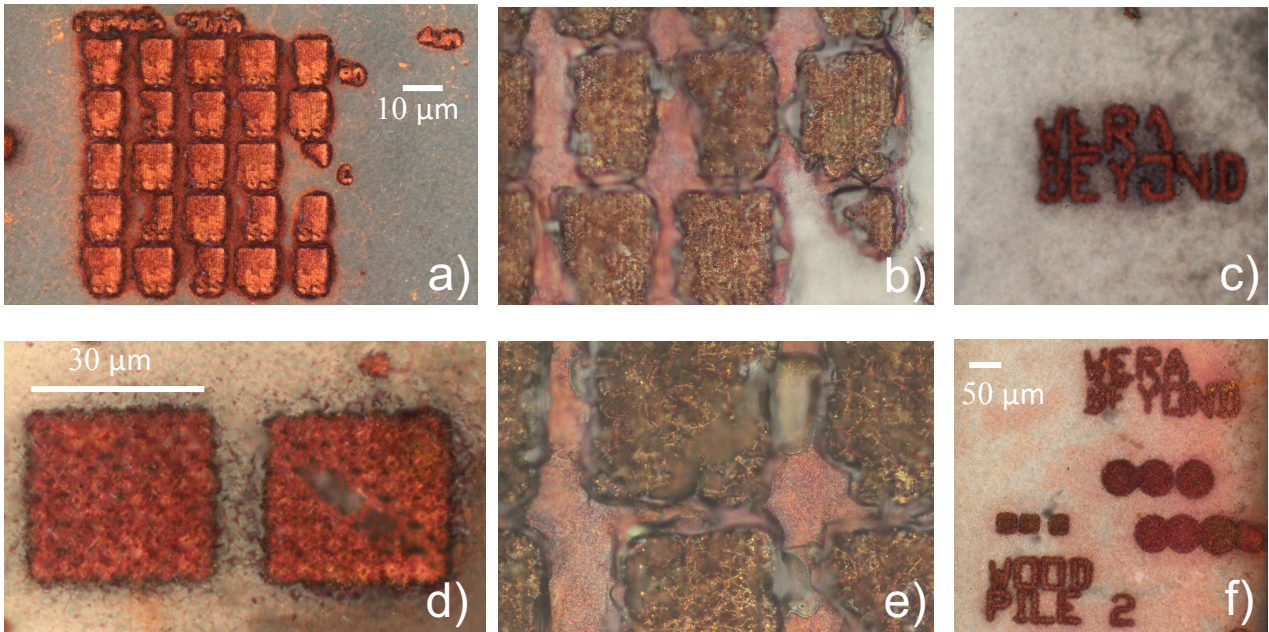


Figure 7.10 *Optical images of lines, isolated points, text and woodpiles nanopatterns realized combining a SiO₂ NWs substrate with a gold precursor. It is possible to print through the nanowires carpet thanks to their refractive index, infact they result transparent to the wavelength of the NIR laser used in TP-DLW system.*

We are still working on the resolution of this system, but many kinds of 2D and 3D patterns can be realized as woodpiles, texts, complex structures like helix and other geometrical shapes.

8. Conclusions and future work

This doctoral thesis has evidenced that SL and TP-DLW are promising AM technologies to produce nanocomposites and metallic nanostructures with high resolution, taking advantage of the one photon and multiphoton absorption physical processes.

In particular, we have demonstrated that a photosensitive resin with different fillers (e.g. AuNPs and SiO₂ NWs) can be combined either with SL or TP-DLW to obtain successfully micro/mesoscale structures with enhanced optical or mechanical properties. Moreover, TP-DLW can also be used to produce different AuNSs, whose size and morphology can be controlled in a wide range with dimensions below the optical diffraction limit. All these materials manufactured have direct implementation in various industrial sectors such as microfluidics, optoelectronics or micro-electromechanical systems. A brief comparison of the materials developed and the AM technologies used in this work is presented in **Table 8.1**.

Table 8.1 *Summary of the work developed in this thesis, showing the different novel materials manufactured and the AM technologies used in each case.*

	AM of metallic nanostructures	AM of polymer-based nanocomposites
SL	-	AuNPs nanocomposites with enhanced optical properties (Chapter 5)
TP-DLW	AuNSs materials with tunable size and morphology (Chapter 6)	SiO ₂ NWs nanocomposites with improved mechanical properties (Chapter 7)

A final analysis evidences that all the protocols and methods proposed have produced groundbreaking and original results.

Namely, it has been possible to fabricate self-standing gold nanocomposites via SL with micrometric resolution ranging from 20 to 200 μm .

An adequate range of KAuCl_4 concentrations which allowed successful SL printing was identified and different post-processing treatments, including UV and temperature, have been studied. It was proved that the thermal reduction of KAuCl_4 gave the best results for these materials. In particular, this treatment produced AuNPs that are homogeneously distributed and well-embedded in the polymeric resin, with a narrow distribution in size and interesting morphologies (*e.g.* nanotriangles and nano-hexagons). This was evidenced by studying both the bulk optical properties via UV-Vis spectroscopy and the microstructure of the material by SEM, and establishing a correlation between these two features. As future work, it would be necessary to study more in detail the physicochemical procedures of the gold precursor dispersion in the resin and the kinetics of UV-curing and thermal synthesis of the AuNPs. For this purpose, it would be interesting to establish a comparison with other metallic precursors and study more in detail the influence of the time in all these steps.

It was also demonstrated that the use of DLW combined with the TPA process (TP-DLW, in analogy with the TPP of photoresists) allows to produce AuNSs with high precision. This was achieved thanks to the use of a highly transparent, thermally reversible hydrogel which is used as matrix to entrap the metal precursor. Given the biological nature of the hydrogel, this technology is also shifted towards a more environmentally-friendly process. Several types of AuNSs were obtained by optimizing different printing variables (laser power, exposure time and scan speed). The growth process of the AuNSs can also be controlled by a second immersion in a gold salt solution that allowed to further increase their size. All these parameters can be modified to tune the morphology and size of the AuNSs, proving that this method can be exploited to get a fine and practically real-time control on the geometry of the different nano-objects, as it was evidenced by high resolution electron microscopy techniques. Hence, this proposed method opens a promising research line in the AM of novel metallic nanostructures. In the future, it will be very interesting to study the photoreduction of other noble metal precursors such as silver, palladium or platinum.

Finally, it has been proven that the use of transparent fillers, as SiO₂ NWs, together with photosensitive resins allows the immediate implementation of TP-DLW in the 3D fabrication of fiber reinforced polymer nanocomposites, as long as the glassy filler and the polymeric matrix have a similar refractive index. Even without an accurate refractive index matching, it was demonstrated the possibility of 3D-printing solid objects with approximately 10 μm thickness through a SiO₂ NWs layer using the commercially available resins for TPP. This permitted the fabrication of nanocomposites having up to 70 wt% SiO₂ NWs with enhanced mechanical properties in comparison with the pristine photoresist. In particular, it was observed a remarkable improvement above one order of magnitude in the nano-hardness and elastic modulus, which makes this approach well-suited for applications in advanced microfluidics and micro-mechanics. Beyond the interest in the enhanced mechanical properties of the developed nanocomposite, it was also demonstrated the efficiency of the SiO₂ NWs as permanent adhesive or sacrificial layer, with well-controlled properties to hold and/or release any fabricated object after TP-DLW. Moreover, SiO₂ NWs can provide a robust internal scaffold in the *shell & scaffold* printing strategy, thus considerably shortening the fabrication time. This evidences the wide versatility of the use of glassy NWs substrates in the development of new materials and strategies for nano-printing in combination with the TP-DLW technique.

9. Bibliography

9.1. Introduction

- [1] C. Mack, *Fundamental Principles of Optical Lithography: The Science of Microfabrication*, **2007**.
- [2] L. F. THOMPSON, **1983**, pp. 1–13.
- [3] O. Rötting, W. Röpke, H. Becker, C. Gärtner, *Microsyst. Technol.* **2002**, 8, 32.
- [4] Y. Lu, S. C. Chen, *Adv. Drug Deliv. Rev.* **2004**, 56, 1621.
- [5] K. Kaneko, H. B. Sun, X. M. Duan, S. Kawata, *Appl. Phys. Lett.* **2003**, 83, 1426.
- [6] D. Bratton, D. Yang, J. Dai, C. K. Ober, *Polym. Adv. Technol.* **2006**, DOI 10.1002/pat.662.
- [7] F. Sanchez, K. Sobolev, *Constr. Build. Mater.* **2010**, DOI 10.1016/j.conbuildmat.2010.03.014.
- [8] D. R. Paul, L. M. Robeson, *Polymer (Guildf)*. **2008**, DOI 10.1016/j.polymer.2008.04.017.
- [9] H. Zhao, Y. Lee, M. Han, B. K. Sharma, X. Chen, J. H. Ahn, J. A. Rogers, *Nano Today* **2020**, 30, 100825.
- [10] M. S. Rill, C. Plet, M. Thiel, I. Staude, G. Von Freymann, S. Linden, M. Wegener, *Nat. Mater.* **2008**, DOI 10.1038/nmat2197.
- [11] M. Malinauskas, L. Jonušauskas, D. Gailevičius, S. Rekštyte, S. Juodkazis, **2018**.
- [12] Q. Liu, Z. Ma, Q. Wu, W. Wang, *Opt. Laser Technol.* **2020**, 130, 106363.
- [13] Q. Shi, J. Zhao, L. Liang, *Prog. Quantum Electron.* **2021**, 100298.
- [14] C. Fenzl, T. Hirsch, O. S. Wolfbeis, *Angew. Chemie - Int. Ed.* **2014**, 53, 3318.
- [15] A. Guglielmelli, P. Rosa, M. Contardi, M. Prato, G. Mangino, S. Miglietta, V. Petrozza, R. Pani, A. Calogero, A. Athanassiou, G. Perotto, L. De Figure 4.9, *Nanomedicine* **2021**, 16, 121.
- [16] G. E. Lio, A. Ferraro, T. Ritacco, D. M. Aceti, A. De Luca, M. Giocondo, R. Caputo, *Adv. Mater.* **2021**, 2008644.

- [17] H. B. Sun, S. Kawata, *Adv. Polym. Sci.* **2004**, DOI 10.1007/b94405.
- [18] C. Sanchez, P. Belleville, M. Popall, L. Nicole, *Chem. Soc. Rev.* **2011**, DOI 10.1039/c0cs00136h.
- [19] S. Shukla, X. Vidal, E. P. Furlani, M. T. Swihart, K. T. Kim, Y. K. Yoon, A. Urbas, P. N. Prasad, *ACS Nano* **2011**, *5*, 1947.
- [20] M. Alsawafta, S. Badilescu, A. Paneri, V. Van Truong, M. Packirisamy, *Polymers (Basel)*. **2011**, *3*, 1833.
- [21] G. M. Burrowg, T. K. Gaylord, *Micromachines* **2011**, *2*, 221.
- [22] A. Baev, P. N. Prasad, H. Ågren, M. Samoć, M. Wegener, *Phys. Rep.* **2015**, DOI 10.1016/j.physrep.2015.07.002.
- [23] V. Hahn, P. Kiefer, T. Frenzel, J. Qu, E. Blasco, C. Barner-Kowollik, M. Wegener, *Adv. Funct. Mater.* **2020**, *30*, DOI 10.1002/adfm.201907795.
- [24] D. Han, G. M. Crouch, Z. Chao, S. K. Fullerton-Shirey, D. B. Go, P. W. Bohn, *Front. Chem.* **2019**, *7*, DOI 10.3389/fchem.2019.00216.
- [25] M. Malinauskas, M. Farsari, A. Piskarskas, S. Juodkazis, *Phys. Rep.* **2013**, DOI 10.1016/j.physrep.2013.07.005.
- [26] L. Jonušauskas, S. Juodkazis, M. Malinauskas, *J. Opt. (United Kingdom)* **2018**, DOI 10.1088/2040-8986/aab3fe.
- [27] Q. Hu, X. Z. Sun, C. D. J. Parmenter, M. W. Fay, E. F. Smith, G. A. Rance, Y. He, F. Zhang, Y. Liu, D. Irvine, C. Tuck, R. Hague, R. Wildman, *Sci. Rep.* **2017**, *7*, 1.
- [28] A. Benali, J.-B. Claude, N. Granchi, S. Checcucci, M. Bouabdellaoui, M. Zazoui, M. Bollani, M. Salvalaglio, J. Wenger, L. Favre, D. Grosso, A. Ronda, I. Berbezier, M. Gurioli, M. Abbarchi, *J. Phys. Photonics* **2020**, *2*, 015002.
- [29] A. Biswas, I. S. Bayer, A. S. Biris, T. Wang, E. Dervishi, F. Faupel, *Adv. Colloid Interface Sci.* **2012**, DOI 10.1016/j.cis.2011.11.001.
- [30] Y. Xia, G. M. Whitesides, *Annu. Rev. Mater. Sci.* **1998**, DOI

10.1146/annurev.matsci.28.1.153.

- [31] W. Kaiser, C. G. B. Garrett, *Phys. Rev. Lett.* **1961**, 7, 229.
- [32] M. Göppert-Mayer, *Ann. der Phys.* **2009**, DOI 10.1002/andp.200910358.
- [33] J. L. Wilbur, A. Kumar, E. Kim, G. M. Whitesides, *Adv. Mater.* **1994**, 6, 600.
- [34] G. A. Ozin, K. Hou, B. V. Lotsch, L. Cademartiri, D. P. Puzzo, F. Scotognella, A. Ghadimi, J. Thomson, *Mater. Today* **2009**, 12, 12.
- [35] X. A. Zhang, I. Te Chen, C. H. Chang, *Nanotechnology* **2019**, DOI 10.1088/1361-6528/ab2282.
- [36] P. Iqbal, J. A. Preece, P. M. Mendes, in *Supramol. Chem.*, **2012**.
- [37] A. Kajbafvala, H. Bahmanpour, M. H. Maneshian, M. Li, *J. Nanomater.* **2013**, 2013, DOI 10.1155/2013/158517.
- [38] M. H. Huang, Y. Wu, H. Feick, N. Tran, E. Weber, P. Yang, *Adv. Mater.* **2001**, 13, 113.
- [39] R. Boukhicha, V. Yam, C. Renard, F. Fossard, D. Bouchier, G. Agnus, T. Maroutian, G. Patriarche, *IOP Conf. Ser. Mater. Sci. Eng.* **2009**, 6, 012015.
- [40] S. Morita, *Microscopy* **2011**, 60, S199.
- [41] Y. Sugimoto, K. Miki, M. Abe, S. Morita, *Phys. Rev. B* **2008**, 78, 205305.
- [42] N. I. Kovtyukhova, T. E. Mallouk, T. S. Mayer, *Adv. Mater.* **2003**, 15, 780.
- [43] S. A. M. Tofail, E. P. Koumoulos, A. Bandyopadhyay, S. Bose, L. O'Donoghue, C. Charitidis, *Mater. Today* **2018**, 21, 22.
- [44] J. Jones, P. Coates, *Www.Hybridmanutech.Com* **2015**, 1.
- [45] O. Ivanova, C. Williams, T. Campbell, *Rapid Prototyp. J.* **2013**, 19, 353.
- [46] S. C. Ligon, R. Liska, J. Stampfl, M. Gurr, R. Mülhaupt, *Chem. Rev.* **2017**, 117, 10212.
- [47] S. Kawata, H. B. Sun, T. Tanaka, K. Takada, *Nature* **2001**, 412, 697.
- [48] G. Rius Suñé, *TDX (Tesis Dr. en Xarxa)* **2008**.
- [49] H. Ning, J. H. Pikul, R. Zhang, X. Li, S. Xu, J. Wang, J. A. Rogers, W. P. King, P. V. Braun, *Proc. Natl. Acad. Sci. U. S. A.* **2015**, 112, 6573.

- [50] S. M. F. Kabir, K. Mathur, A. F. M. Seyam, *Compos. Struct.* **2020**, 232, DOI 10.1016/j.compstruct.2019.111476.
- [51] G. Taormina, C. Sciancalepore, F. Bondioli, M. Messori, *Polymers (Basel)*. **2018**, 10, DOI 10.3390/polym10020212.
- [52] J. Z. Manapat, Q. Chen, P. Ye, R. C. Advincula, *Macromol. Mater. Eng.* **2017**, 302, 1.
- [53] A. Selimis, V. Mironov, M. Farsari, *Microelectron. Eng.* **2015**, 132, 83.
- [54] F. Kotz, A. S. Quick, P. Risch, T. Martin, T. Hoose, M. Thiel, D. Helmer, B. E. Rapp, *Adv. Mater.* **2021**, 33, DOI 10.1002/adma.202006341.
- [55] B. H. Cumpston, S. P. Ananthavel, S. Barlow, D. L. Dyer, J. E. Ehrlich, L. L. Erskine, A. A. Heikal, S. M. Kuebler, I. Y. S. Lee, D. McCord-Maughon, J. Qin, H. Röckel, M. Rumi, X. L. Wu, S. R. Marder, J. W. Perry, *Nature* **1999**, DOI 10.1038/17989.
- [56] T. Ritacco, L. Ricciardi, M. La Deda, M. Giocondo, *J. Eur. Opt. Soc.* **2016**, DOI 10.2971/jeos.2016.16008.
- [57] M. Göppert-Mayer, M. Göppert-Mayer, *Ann. Phys.* **1931**.
- [58] M. Röhrig, M. Thiel, M. Worgull, H. Hölscher, *Small* **2012**, DOI 10.1002/sml.201200308.
- [59] K. Sugioka, Y. Cheng, *Appl. Phys. Rev.* **2014**, 1, 041303.
- [60] J. Serbin, A. Egbert, A. Ostendorf, B. N. Chichkov, R. Houbertz, G. Domann, J. Schulz, C. Cronauer, L. Fröhlich, M. Popall, *Opt. Lett.* **2003**, DOI 10.1364/ol.28.000301.
- [61] H. B. Sun, S. Kawata, in *J. Light. Technol.*, **2003**.
- [62] M. Sakamoto, M. Fujistuka, T. Majima, *J. Photochem. Photobiol. C Photochem. Rev.* **2009**, DOI 10.1016/j.jphotochemrev.2008.11.002.
- [63] S. Maruo, O. Nakamura, S. Kawata, *Opt. Lett.* **1997**, 22, 132.
- [64] R. W. Boyd, in *Nonlinear Opt. (Second Ed. (Ed.: R.W. Boyd)*, Academic Press, San Diego, **2003**, pp. 1–65.
- [65] C. B. Schaffer, A. Brodeur, E. Mazur, *Meas. Sci. Technol.* **2001**, 12, 1784.
- [66] P. K. Scott C. Jones, Peter Braunlich, R. Thomas Casper, Xiao-An Shen, **n.d.**, DOI

10.1117/12.7977089.

- [67] M.-F. Yu, B. S. Files, S. Arepalli, R. S. Ruoff, *Phys. Rev. Lett.* **2000**, *84*, 5552.
- [68] K. Jensen, W. Mickelson, A. Kis, A. Zettl, *Phys. Rev. B* **2007**, *76*, 195436.
- [69] N. Sinha, J. T.-W. Yeow, *IEEE Trans. Nanobioscience* **2005**, *4*, 180.
- [70] S. F. A. Acquah, B. E. Leonhardt, M. S. Nowotarski, J. M. Magi, K. A. Chambliss, T. E. S. Venzel, S. D. Delekar, L. A. Al-Hariri, in *Carbon Nanotub. - Curr. Prog. Their Polym. Compos.*, InTech, **2016**.
- [71] B. Podsiadły, P. Matuszewski, A. Skalski, M. Słoma, *Appl. Sci.* **2021**, *11*, 1272.
- [72] W. Ye, W. Wu, X. Hu, G. Lin, J. Guo, H. Qu, J. Zhao, *Compos. Sci. Technol.* **2019**, *182*, 107671.
- [73] A. S. De León, S. I. Molina, *Polymers (Basel)*. **2020**, *12*, 1103.
- [74] K. Matras-Postolek, K. Chojnacka-Gorka, M. Bredol, K. Guguła, *J. Lumin.* **2018**, *203*, 655.
- [75] S. Satoh, K. Susa, I. Matsuyama, *J. Non. Cryst. Solids* **1992**, *146*, 121.
- [76] H. Jiang, X. Pan, N. Li, Z. Zhang, J. Zhu, X. Zhu, *React. Funct. Polym.* **2017**, *111*, 1.
- [77] W. Z. Yuan, R. Hu, J. W. Y. Lam, N. Xie, C. K. W. Jim, B. Z. Tang, *Chem. - A Eur. J.* **2012**, *18*, 2847.
- [78] Q. Guo, R. Ghadiri, T. Weigel, A. Aumann, E. L. Gurevich, C. Esen, O. Medenbach, W. Cheng, B. Chichkov, A. Ostendorf, *Polymers (Basel)*. **2014**, *6*, 2037.
- [79] N. B. Crane, J. Wilkes, E. Sachs, S. M. Allen, *Rapid Prototyp. J.* **2006**, *12*, 266.
- [80] D. Giuntini, E. Torresani, K. T. Chan, M. Blankenburg, L. Saviot, B. Bor, B. Domènech, M. Shachar, M. Müller, E. A. Olevsky, J. E. Garay, G. A. Schneider, *Nanoscale Adv.* **2019**, *1*, 3139.
- [81] J. Li, J. Kong, Q. Zhu, H. Li, *AIChE J.* **2017**, *63*, 459.
- [82] W. Chen, H. Wang, H. Tang, C. Yang, Y. Li, *Anal. Chem.* **2019**, *91*, 14188.
- [83] H. Ma, J.-F. Chen, H.-F. Wang, P.-J. Hu, W. Ma, Y.-T. Long, *Nat. Commun.* **2020**, *11*, 2307.
- [84] X. Zhu, C. H. Ahn, *IEEE Sens. J.* **2006**, *6*, 1280.
- [85] X. Zhu, L. Shi, M. S. Schmidt, A. Boisen, O. Hansen, J. Zi, S. Xiao, N. A. Mortensen, *Nano*

Lett. **2013**, *13*, 4690.

[86] I. Izquierdo-Lorenzo, S. Jradi, P.-M. Adam, *RSC Adv.* **2014**, *4*, 4128.

[87] T. Ritacco, P. Pagliusi, M. Giocondo, *Colloids Surfaces A Physicochem. Eng. Asp.* **2021**, *610*, 125927.

[88] J. Comyn, in *Polym. Permeability*, Springer Netherlands, Dordrecht, **1985**, pp. 1–10.

[89] A. Fick, *Ann. der Phys. und Chemie* **1855**, *170*, 59.

[90] K. Sugioka, Y. Cheng, *Appl. Phys. Rev.* **2014**, *1*, DOI 10.1063/1.4904320.

[91] R. K. Jayne, T. J. Stark, J. B. Reeves, D. J. Bishop, A. E. White, *Adv. Mater. Technol.* **2018**, *3*, 1700293.

[92] T. Frenzel, M. Kadic, M. Wegener, *Science (80-.)*. **2017**, *358*, 1072.

9.2. Additive Manufacturing of AuNPs composites via SL

- [1] W. Di Cianni, M. de la Mata, F. J. Delgado, G. Desiderio, S. I. Molina, A. S. de León, M. Giocondo, *Int. J. Mol. Sci.* **2021**, *22*, 7465.
- [2] N. Sarfraz, I. Khan, *Chem. – An Asian J.* **2021**, *16*, 720.
- [3] G. Palermo, T. Ritacco, D. M. Aceti, L. Pezzi, M. Giocondo, A. De Luca, *Crystals* **2017**, DOI 10.3390/cryst7010014.
- [4] S. Bruzzone, M. Malvaldi, G. P. Arrighini, C. Guidotti, *J. Phys. Chem. B* **2004**, *108*, 10853.
- [5] S. J. Oldenburg, *Rice Univ., Houston, TX, USA. F. URL* **2000**, 98 pp.
- [6] K. Slyusarenko, B. Abécassis, P. Davidson, D. Constantin, *Nanoscale* **2014**, *6*, 13527.
- [7] “Mie Theory Calculator,” can be found under [https://nanocompositix.com/pages/mie-theory-calculator#target %0D%0A](https://nanocompositix.com/pages/mie-theory-calculator#target%0D%0A), **n.d.**
- [8] S. Mohan Bhagyaraj, O. S. Oluwafemi, in *Synth. Inorg. Nanomater.*, Elsevier, **2018**, pp. 1–18.
- [9] Q. Wan, R. C. Masters, D. Lidzey, K. J. Abrams, M. Dapor, R. A. Plenderleith, S. Rimmer, F. Claeysens, C. Rodenburg, *Ultramicroscopy* **2016**, *171*, 126.
- [10] A. S. de León, M. de la Mata, S. I. Molina, *Colloids Surfaces A Physicochem. Eng. Asp.* **2021**, *624*, 126766.
- [11] Cytodiagnostics, “Gold Nanoparticle Properties Background,” can be found under <https://www.cytodiagnostics.com/pages/gold-nanoparticle-properties>, **n.d.**
- [12] A. S. De León, S. I. Molina, *Polymers (Basel)*. **2020**, *12*, 1103.
- [13] J.-P. Gatellier, J.-R. Disnar, *Org. Geochem.* **1990**, *16*, 631.
- [14] S. Porel, S. Singh, T. P. Radhakrishnan, *Chem. Commun.* **2005**, 2387.
- [15] N. T. K. Thanh, N. Maclean, S. Mahiddine, *Chem. Rev.* **2014**, *114*, 7610.
- [16] S. Cherevko, A. A. Topalov, A. R. Zeradjanin, I. Katsounaros, K. J. J. Mayrhofer, *RSC Adv.* **2013**, *3*, 16516.

9.3. TP-DLW of metallic structures on opaque substrates

- [1] I. Izquierdo-Lorenzo, S. Jradi, P. M. Adam, *RSC Adv.* **2014**, DOI 10.1039/c3ra46220j.
- [2] Y. Y. Cao, N. Takeyasu, T. Tanaka, X. M. Duan, S. Kawata, *Small* **2009**, DOI 10.1002/smll.200801179.
- [3] Y. Y. Cao, X. Z. Dong, N. Takeyasu, T. Tanaka, Z. S. Zhao, X. M. Duan, S. Kawata, *Appl. Phys. A Mater. Sci. Process.* **2009**, DOI 10.1007/s00339-009-5270-7.
- [4] G. Palermo, T. Ritacco, D. M. Aceti, L. Pezzi, M. Giocondo, A. De Luca, *Crystals* **2017**, DOI 10.3390/cryst7010014.
- [5] T. Ritacco, L. Ricciardi, M. La Deda, M. Giocondo, *J. Eur. Opt. Soc.* **2016**, DOI 10.2971/jeos.2016.16008.
- [6] V. Hahn, P. Kiefer, T. Frenzel, J. Qu, E. Blasco, C. Barner-Kowollik, M. Wegener, *Adv. Funct. Mater.* **2020**, *30*, DOI 10.1002/adfm.201907795.
- [7] S. Tabrizi, Y. Cao, H. Lin, B. Jia, *Sci. China Physics, Mech. Astron.* **2017**, *60*, 034201.
- [8] E. Blasco, J. Müller, P. Müller, V. Trouillet, M. Schön, T. Scherer, C. Barner-Kowollik, M. Wegener, *Adv. Mater.* **2016**, *28*, 3592.
- [9] J. Comyn, in *Polym. Permeability*, Springer Netherlands, Dordrecht, **1985**, pp. 1–10.
- [10] Y. Oyanagi, M. Matsumoto, *J. Colloid Sci.* **1962**, *17*, 426.
- [11] A. Fick, *London, Edinburgh, Dublin Philos. Mag. J. Sci.* **1855**, *10*, 30.
- [12] W. Di Cianni, M. de la Mata, F. J. Delgado, G. Desiderio, S. I. Molina, A. S. de León, M. Giocondo, *Int. J. Mol. Sci.* **2021**, *22*, 7465.
- [13] K. Kurihara, J. H. Fendler, J. Kizling, P. Stenius, *J. Am. Chem. Soc.* **1983**, *105*, 2574.
- [14] M. Sakamoto, M. Fujistuka, T. Majima, *J. Photochem. Photobiol. C Photochem. Rev.* **2009**, DOI 10.1016/j.jphotochemrev.2008.11.002.
- [15] N. T. K. Thanh, N. Maclean, S. Mahiddine, *Chem. Rev.* **2014**, *114*, 7610.
- [16] E. G. Agunloye, **2018**.
- [17] P. Kiefer, V. Hahn, M. Nardi, L. Yang, E. Blasco, C. Barner-Kowollik, M. Wegener, *Adv.*

Opt. Mater. **2020**, *8*, 2000895.

- [18] K. Kaneko, H. B. Sun, X. M. Duan, S. Kawata, *Appl. Phys. Lett.* **2003**, *83*, 1426.
- [19] C. L. Lay, C. S. L. Koh, Y. H. Lee, G. C. Phan-Quang, H. Y. F. Sim, S. X. Leong, X. Han, I. Y. Phang, X. Y. Ling, *ACS Appl. Mater. Interfaces* **2020**, *12*, 10061.
- [20] J. Polte, *CrystEngComm* **2015**, *17*, 6809.
- [21] C. H. Turner, Y. Lei, Y. Bao, *Nanoscale* **2016**, *8*, 9354.
- [22] Q. Hu, X. Z. Sun, C. D. J. Parmenter, M. W. Fay, E. F. Smith, G. A. Rance, Y. He, F. Zhang, Y. Liu, D. Irvine, C. Tuck, R. Hague, R. Wildman, *Sci. Rep.* **2017**, *7*, 1.
- [23] S. Shukla, X. Vidal, E. P. Furlani, M. T. Swihart, K. T. Kim, Y. K. Yoon, A. Urbas, P. N. Prasad, *ACS Nano* **2011**, *5*, 1947.
- [24] G. E. Lio, A. Ferraro, T. Ritacco, D. M. Aceti, A. De Luca, M. Giocondo, R. Caputo, *Adv. Mater.* **2021**, 2008644.

9.4. Additive Manufacturing of SiO₂ NWs nanocomposites via TP-DLW

- [1] F. Kotz, A. S. Quick, P. Risch, T. Martin, T. Hoose, M. Thiel, D. Helmer, B. E. Rapp, *Adv. Mater.* **2021**, 33, DOI 10.1002/adma.202006341.
- [2] J. Z. Manapat, Q. Chen, P. Ye, R. C. Advincula, *Macromol. Mater. Eng.* **2017**, 302, 1.
- [3] A. Trautmann, B. Götzendorfer, T. Walther, R. Hellmann, *Opt. Express* **2018**, 26, 29659.
- [4] T. Tanaka, H.-B. Sun, S. Kawata, *Appl. Phys. Lett.* **2002**, 80, 312.
- [5] M. Talib, J. A. Covington, A. Bolarinwa, **2014**, pp. 129–135.
- [6] T. Gissibl, S. Thiele, A. Herkommer, H. Giessen, *Nat. Photonics* **2016**, 10, 554.
- [7] V. Hahn, P. Kiefer, T. Frenzel, J. Qu, E. Blasco, C. Barner-Kowollik, M. Wegener, *Adv. Funct. Mater.* **2020**, 30, DOI 10.1002/adfm.201907795.

Figures

Figure 2.1 <i>Examples of applications of the fabrication of metal-containing nanomaterials: a TMPTA-Au nano-composite periodic structure for metamaterials^[27]; a flexible photonic device based on dielectric antennas made with SiGe islands embedded in a PDMS slice^[28].</i>	9
Figure 2.2 <i>Top down (TD) and Bottom Up (BU) approaches for Additive Manufacturing.</i>	10
Figure 2.3 <i>Binary photomasks employed for photolithography: light passes through the mask and polymerizes with negative or positive tone; self-assembly technique for nanofabrication for static and dynamic cases and their connection with co-assembly, hierarchical and directed self-assembly (Ozin, 2009); microcontact printing with elastomeric (poly-dimethyl-siloxane, PDMS) stamps; after inking the stamp with the material solution, the deposition occurs by direct contact of the stamp with the surface of the substrate (Fernandes, 2013^[34]).</i>	11
Figure 2.4 <i>Silica nanowires grown on a Si(111) substrate, synthesized by UHV-CVD (ultra-high vacuum chemical vapor deposition) with a silane pressure of 6.67 Pa (Boukchicha, 2012); VLS growth of ZnO nanowire networks from the patterned Au islands (Huang, 2001)^[38,39]</i>	13
Figure 2.5 <i>Atom-based letters created by vertical atom manipulation using STM and AFM. (a) Result of surface modification by STM, which reads 'PEACE 91 HCRL' (Hosoki S, Hosaka S, and Hasegawa T (1992) Surface modification of MoS₂ using an STM. Appl. Surf. Sci. 60-61: 643–647) and (b) complex atomic patterning by Si atoms embedded on an Sn/Si surface using AFM vertical atom-interchange manipulation (Sugimoto Y, Pou P, Custance O, Jelinek P, Abe M, Pérez R, and Morita S (2008) Complex patterning by vertical interchange atom manipulation using atomic force microscopy. Science 322:413–417) (Morita, 2011) ^[40,41]</i>	13
Figure 2.6 <i>Scheme showing the surface sol-gel (SSG) synthesis of SiO₂ nanotubes (route 1) and SiO₂ coated nanowires (route 2) (Kovtyukhova, 2003)^[42]</i>	14
Figure 2.7 <i>A scheme of the seven families of Additive Manufacturing technologies according to the American Society for Testing and Materials^[44].</i>	17

Figure 2.8 *DeScribe user interface where an object is ready for printing. This is an example of a software to import 3D structure designs (left); Rhinoceros user interface to project a 3D object (right).*18

Figure 2.9 *Examples of common objects realized exploiting the marriage between nanofabrication and additive manufacturing. (S.C. Ligon et al, 2017, Chem Rev; S. Kawata, 2001, Nature)^[46,47]*20

Figure 2.10 *Comparison of the different AM techniques as a function of the voxel size and the production time. In detail speed (total peak printing rate) plotted on the vertical axis is given in units of voxels per second on the left scale while in bits per second on the right scale. The gray diagonals correspond to lines of constant volume printing rate. The inverse of the voxel size is associated with the resolution. Figure and caption are adapted from: Hahn, V., Kiefer, P., Frenzel, T., Qu, J., Blasco, E., Barner-Kowollik, C., Wegener, M., “Rapid Assembly of Small Materials Building Blocks (Voxels) into Large Functional 3D Metamaterials”. Adv. Funct. Mater. 2020, 1907795. doi.org/10.1002/adfm.201907795 ^[23].*21

Figure 2.11 *Single Photon (left) vs Two Photon Polymerization (right) representations in terms of polymerized area*27

Figure 2.12 *SP and TP absorption process where one (left) or two photons (right) are absorbed and allow the transition to the higher level of energy.*.....29

Figure 4.1 *Equipment for the different treatments: the Formlabs FCure UV-chamber for the UV-curing (left) and the muffle oven Nabertherm for the thermal treatments (right).*.....38

Figure 4.2 *UV-Vis Macro-cuvettes containing different concentrations of KAuCl₄ before the UV-curing treatment of 60 minutes.*.....39

Figure 4.3 *Illustrative examples of droplet and sandwich sample*40

Figure 4.4 *Scheme of a typical SL printing process. The laser acts on a photosensitive resin precursor placed in a tank taking advantage of a mirror and lens system (left). Image of the Form I+ SL printer used in the manufacturing of the gold nanocomposites (right).*.....41

- Figure 4.5 *A sketch of the apparatus of the first test with a glass substrate, a drop of PVA+ H₂AuCl₄ solution and the Laser beam. A NIR femtosecond laser $\lambda = 780$ nm with the objective working in oil immersion is used.42*
- Figure 4.6 *A sketch of the apparatus of the second test with a silicon substrate, a drop of PVA+ H₂AuCl₄ solution is infiltrated for capillarity in the cell of 10 μ m of thickness given by two stripes of mylar and the Laser beam. NIR femtosecond laser $\lambda = 780$ nm with the objective working in oil immersion is used.43*
- Figure 4.7 *Scheme depicting the nanofabrication of AuNSs via TP-DLW process: (a) a hydrogel layer is deposited on the top of a silicon substrate; (b) immersion of the hydrogel film in a H₂AuCl₄ solution for 30 minutes to allow Au³⁺ diffusion into the hydrogel matrix; (c) photoreduction of Au³⁺ into Au⁰ via TP-DLW using a NIR laser taking advantage of the TPA process; (d) a washing step with deionized water stops the created AuNPs growth; a second washing step with warm water removes the hydrogel film, leaving the AuNSs attached to the silicon substrate.....44*
- Figure 4.8 *Scheme depicting the nucleation and the growth of the AuNSs created. The first step is (a) the creation via TP-DLW of the AuNSs on the silicon substrate; during the lag between the exposure and the first washing step with deionized water to remove the hydrogel, the autocatalytic growth of the nanoparticles goes on; (b) during the lag between the exposure and the washing steps the growth of the nanoparticles goes on then, in order to tune the size of the AuNSs, a second immersion in a 10⁻² M H₂AuCl₄ solution is done allowing the growth of the AuNSs through the migration of the chloroauric ions towards the nanostructures and the reduction of Au³⁺ into Au⁰; (c) a subsequent bath in deionized water stops the growth; (d) the AuNPs have grown in a controlled way only where the AuNSs are lodged.....45*
- Figure 4.9 *Set-up of the TP-DLW system. a) The Si chip, carrying the SiO₂NW carpet soaked with the IP-S photo-resin, is fixed on a glass coverslip and placed in the sample-holder of the inverted microscope with the SiO₂NWs facing the focusing lens; b) a 500x500x20 μ m parallelepiped is*

designed through a CAD file c) with a P.C. connected to the TPA system: d) the polymerization is performed inside the voxel and through the carpet of SiO₂NWs, e) leveraging the TPA process.46

Figure 4.10 Three different kind of structures are realized with the process protocol that grants considerable advantages in all the types: a) adhesive layer, for adherent structures; b) sacrificial layer, for detaching structures; c) only shell, for structures sustained by the Si O₂NWs scaffold....47

Figure 4.11 Typical nano indentation curve force (P) vs indentation depth (h) together with significant indentation parameters used to calculate the indentation nano harness (H_{IT}) and Young's modulus (E_{IT}).....50

Figure 5.1 UV-Vis macro-cuvette containing the SL resin and the gold precursor KAuCl₄. Black arrow points at the region where the KAuCl₄ is not fully dissolved in the resin. Sonication for at least 30 min is needed to ensure a homogeneous mixture.54

Figure 5.2 Macro-cuvettes containing the full range of concentrations studied (0.01 wt%, 0.1 wt%, 0.5 wt%, 1 wt% and 2 wt% KAuCl₄) a) before and b) after UV-curing for 30 min. Samples with KAuCl₄ concentrations below 0.5% wt are properly cured, while 1 wt% and 2 wt% KAuCl₄ are not completely polymerized, in particular in the center of the cuvette.56

Figure 5.3 Macro-cuvettes containing the full range of concentrations studied (0.01 wt%, 0.1 wt%, 0.5 wt%, 1 wt% and 2 wt% KAuCl₄) a) before and b) after UV-curing for 60 min. In these conditions, samples with 1 wt% KAuCl₄ were successfully cured. Although all the samples are solid after curing, some irregularities are observed due to the contraction of the resin during the photopolymerization.56

Figure 5.4 Cross-sections of samples containing a) 0.1 wt%; b) 0.5 wt% and c) 1 wt% KAuCl₄ after the thermal treatment in the muffle oven in the cuvettes. In a) and b) some pink shades can be observed while in c) regions of red color are evident.57

Figure 5.5 Sandwich samples containing 0.1 wt% KAuCl₄ (top row), 0.5 wt% KAuCl₄ (middle row) and 1 wt% KAuCl₄ (bottom row) before any UV or thermal treatment.59

Figure 5.6 Sandwich samples containing 0.1 wt% KAuCl_4 (top row), 0.5 wt% KAuCl_4 (middle row) and 1 wt% KAuCl_4 (bottom row) after the four different UV and thermal treatments proposed.59

Figure 5.7 UV-Vis spectra of sandwich samples after the different UV and thermal treatments for nanocomposites containing a) 0.1 wt%, b) 0.5 wt% and c) 1 wt% KAuCl_462

Figure 5.8 Wavelength values corresponding to the maximum absorbance in the visible range (λ_{max}) of the sandwich samples as a function of KAuCl_4 . Values are extracted from the UV-Vis spectra after [UV + T].63

Figure 5.9 Droplet samples with a) 0.5 wt%, 1 wt% and 2 wt% KAuCl_4 after 1 h of UV-curing; b) 0.5 wt% and 1 wt% KAuCl_4 after [UV + (UV + T)] and c) 0.5 wt% KAuCl_4 after [UV + T].64

Figure 5.10 Sample containing 1 wt% KAuCl_4 after [UV + T] treatment. Change of color is shown when the light orientation and angle varies. Sample looks red when white light is reflected and turns into blue or violet when light is transmitted.65

Figure 5.11 Samples after the second treatment in [UV+(UV+T)] (left) and [UV + T] (right). The coloration is noticeably different.66

Figure 5.12 SEM micrographs of nanocomposites with 0.5 wt% KAuCl_4 after [UV + (UV + T)] (left) and after [UV + T] (right). CBSE detector show high contrast images where brighter regions correspond to elements with higher atomic number (i.e. Au).67

Figure 5.13 a) Digital picture and b) SEM micrograph of a monolayer with 0.1 wt% KAuCl_4 and 0.2 mm thickness printed by SL without any further treatment (green sample); c) SEM micrograph of a monolayer with 0.3 wt% KAuCl_4 and 0.2 mm thickness printed by SL without any further treatment (green sample). Inset in c) shows some KAuCl_4 cubic crystals.69

Figure 5.14 a) Digital picture and b), c) SEM micrographs of a monolayer with 0.1 wt% KAuCl_4 and 0.2 mm thickness printed by SL after [UV + (UV + T)].70

Figure 5.15 a) Digital picture and b), c) SEM micrographs of a monolayer with 0.1 wt% KAuCl_4 and 0.2 mm thickness printed by SL after [UV + T]. Inset in c) shows some AuNPs in the shape of nanotriangles and nano-hexagons.70

Figure 5.16 *Box plot of the average AuNPs diameter for monolayers with 0.1 wt% KAuCl₄ and 0.2 mm thickness printed by SL after [UV + (UV + T)] and [UV + T].*71

Figure 5.17 *SEM micrographs of a 0.2 mm thickness monolayer printed by SL after [UV + T] with a) 0.05 wt% KAuCl₄; b) 0.1 wt% KAuCl₄; c) 0.3 wt% KAuCl₄; and d) 0.5 wt% KAuCl₄.*72

Figure 5.18 *Quantification of the AuNPs diameter in a 0.2 mm thickness monolayer printed by SL after [UV + T] with KAuCl₄ ranging from 0.05 to 0.5 wt%.*74

Figure 5.19 *Influence of the KAuCl₄ concentration in the AuNPs mean diameter for 0.2 mm thickness monolayers printed by SL after [UV + T]. The mean diameter follows a linear trend with the concentration of the gold precursor.*75

Figure 5.20 *Digital pictures of samples printed by SL with 0.1 wt% KAuCl₄ and 0.02mm, 0.2 mm and 1 mm thickness before (left) and after (right) the thermal treatment of [UV + T]. The samples are arranged in increasing order of thickness, from left to right, in all pictures.*76

Figure 5.21 *SEM micrographs of a) a monolayer with a 0.2 mm thickness and b) 3D object with 1 mm thickness containing 0.1 wt% KAuCl₄ printed by SL after [UV + T]; c) influence of the thickness of the sample in the AuNPs mean diameter.*77

Figure 5.22 *3D-printed parallelepiped with dimensions 20 x 20 x 10 mm with 0.1 wt% KAuCl₄ using a layer height of 0.2 mm a) right after printing (green sample); b) after [UV + T] under reflected white light; c) after [UV + T] under transmitted white light; d) after [UV + T] on top of a text to illustrate its degree of transparency.*78

Figure 5.23 *UV-Vis spectra of a 3D-printed parallelepiped with dimensions 20 x 20 x 10 mm with 0.1 wt% KAuCl₄ before (green sample, grey curve) and after [UV + T] (pink curve).*79

Figure 5.24 *Cartoon and SEM images of a 3D-printed parallelepiped with dimensions 20 x 20 x 10 mm with 0.1 wt% KAuCl₄ using a layer height of 0.2 mm after [UV + T]. Low magnification SEM image on top (light blue frame) demonstrates that AuNPs are selectively located at the edges of the printed layers in the XZ plane (dashed, green frames). High magnification SEM images below correspond to the detail of these regions where the AuNPs can be found.*80

Figure 5.25 *Nanocomposites containing 0.1 wt% $KAuCl_4$ after UV-curing for 60 min at room temperature. Sample in the left was prepared months before the picture was taken and exhibits an orange color, caused by the presence of Au^{3+} (yellow) and AuNPs (red). Sample in the right is a fresh sample which exhibits only the characteristic color of the Au^{3+} species.*81

Figure 6.1 *Optical microscope images are shown as example of the kind of patterns we can realize with the traditional protocol, using IP-L photoresist and the 63x objective in the oil immersion configuration, LP = 65 mW, SS = 12000 $\mu\text{m/s}$.*85

Figure 6.2 *Optical microscope images of nanopatterns printed on glass with LP=10-20 mW, SS = 10 $\mu\text{m/s}$, d=2 μm . The (b) image is a magnification of isolated points shape structure of (a). (c) Linear structures (l = 20 μm).*87

Figure 6.3 *Optical microscope images of nanopatterns. On the right a magnification of the isolated points structures.*88

Figure 6.4 *(a) An optical microscope image of nanopatterns. (b), (c), (d) SEM images of the structures, linear and isolated points respectively, and a magnification of the isolated points structures. We need to use two drops of solution ((50+50) μL to obtain visible structures.*89

Figure 6.5 *Structures are printed but only in some areas, where the drop is dryer and the process can be carried out. After the deionized water bath some structures are washed away.*90

Figure 6.6 *Before and after the deionized water bath, in a time in less than 24 h.*90

Figure 6.7 *(a) An optical microscope image where is shown that the sample does not result totally clean also at naked eye (b), despite the bath in deionized water.*90

Figure 6.8 *SEM micrographs showing AuNSs fabricated via TP-DLW using an ET = 100 ms and a LP of a) 40 mW; b) 60 mW; c) 100 mW; d) Quantification and e) box plot of the radius of the different AuNSs printed. Box plots were made in all cases from at least 180 independent measurements ($N > 180$) as shown in (d).*94

Figure 6.9 *SEM micrographs showing AuNSs fabricated via TP-DLW using an ET = 150 ms and (a) LP = 40 mW; (b) LP = 100 mW. Box plots comparing the radius of the different AuNSs printed with*

different ET at (c) LP = 40 mW and (d) LP = 100 mW. Box plots were made in all cases from at least 180 independent measurements ($N > 180$).95

Figure 6.10 SEM micrographs showing AuNSs fabricated via DLW using a SS = 200 $\mu\text{m/s}$ and a LP of (a) 40 mW; (b) 60 mW; (c) 100 mW; (d) Average line width of the different AuNSs printed as a function of the LP.96

Figure 6.11 SEM images of the nanopatterns (a) before and (b) after AuNSs growth by immersion in a 10^{-2} M HAuCl₄ bath for 30 min; (c) Distribution of the AuNSs size before growth (blue, $N = 29$) and after growth (red, $N = 26$).97

Figure 6.12 Scheme of the sample preparation for TEM analysis via FIB cut. The sample was study along the Si (substrate) [110] zone axis. A layer of Pt is deposited on the top of the sample with ion beam to protect the structures from the destructive cutting procedure.98

Figure 6.13 (a), (b), (c) HAADF and (d), (e) HRTEM images of the cross section of different AuNSs made with a LP = 100 mW and ET = 150 ms after TP-DLW. The first step of the growth before the second HAuCl₄ bath, the autocatalytic one, can be observed in these images. HAADF images provide Z-contrast indicating that areas with heavier elements are those containing AuNPs. (b) and (d) show that some of the AuNSs are physically deposited onto the Si substrate surface, likely due to a stochastic heterogeneous nucleation event. Arrows in (d) indicate merging regions: TP-DLW is able to create larger structures by the coalescence of smaller individual AuNPs, leading to polycrystalline, highly faceted AuNSs. Different shapes of individual AuNPs (decahedral, pentagonal bipyramid) are shown in (c) and (e).100

Figure 6.14 HAADF image and EDX maps of AuNSs made with a LP = 100 mW and ET = 150 ms. Au, Si, Pt and O signals are displayed in yellow, magenta, orange and cyan, respectively. AuNSs consist of solely AuNPs, which are able to self-assemble into larger micron-sized clusters, without oxidized species, precursor residues or other impurities. EDX also shows a thin SiO_x native layer at the substrate surface (~ 2 nm thick).101

Figure 6.15 (a-c) STEM after FIB cut and (d-g) TEM images of the cross section of different AuNSs made with a LP = 100 mW and ET = 150 ms and the second immersion in a 10^{-2} M H₂AuCl₄ solution for 30 min. After the bath, individual AuNPs are not appreciated, in fact (d-g) they have been merged by their facets and exhibit a higher polycrystalline morphology..... 101

Figure 6.16 AuNPs size distribution after TP-DLW and immersion in deionized water (blue, N = 75) and after immersion in a 10^{-2} M H₂AuCl₄ bath for 30 min (red, N = 27). Gaussian distribution before and after the bath evidence the growth of the AuNSs. Quantitative analysis for AuNPs sizes shows that they range from 50 ± 11 nm to 123 ± 35 nm and a significant increase in the AuNSs size after bath is observed..... 102

Figure 6.17 Same circular concentric structure at optical (left) and scanning electron (right) microscope. It is evident that not all the circles are well defined after the printing due to the low and non-uniform concentration ($C \sim 10^{-3}$ M) 105

Figure 6.18 SEM images of a circular concentric structure, not visible with the optical microscope. It is possible to see the very little size of the nanoparticles down to 30 nm, due to the low concentration ($C \sim 10^{-3}$ M)..... 105

Figure 6.19 Optical microscope images (the last three between crossed polarizers) of linear and honeycomb nanopatterns. Due to the low concentration ($C \sim 10^{-3}$ M) especially at the borders of the honeycomb structure the isolated points are not well defined. The diameter of the single spot is around 3 μ m and the lines are 20 μ m long (printing parameters: SS = 10 μ m/s, LP=100 mW)..... 106

Figure 6.20 Optical microscope images of the AuNSs using a concentration of 10^{-1} M H₂AuCl₄. The structures are inhomogeneous and precipitates and gradients of concentration are also present. 107

Figure 6.21 SEM images of the gold nanoparticles for the three treatments after that H₂AuCl₄ concentration has been set at 10^{-2} M: 1 h (a), 2 h (b) and 3 h (c). It is observable that the nanoparticles tend to cluster with time and the smaller ones grow up 90-100 nm while the bigger ones grow up 300 nm. 108

Figure 6.22 *Nanopatterns rich in gold nanoparticles for 1 hour (a), 2 hours (b), 3 hours (c) treatment. It is evident that with increasing time, nanoparticles clusterize and diffuse.* 108

Figure 6.23 *Nanopatterns after 1 (a) and 3 (b) hours of treatment.* 109

Figure 6.24 *Average diameter of the different AuNPs printed as a function of the duration of the bath.*
..... 109

Figure 6.25 *Optical (a, c, e) and SEM (b, d, f) images of different nanopatterns (circles, lines and isolated points) of different dimensions, where it is visible the red coloration of gold for optical and bright white for SEM.* 111

Figure 6.26 *Optical (up) and SEM (down) images of the Leonardo Da Vinci's "Lady with an Ermine" reproduced at the microscale with the simultaneous photopolymerization-photoreduction technique to allow the entrapping of the gold nanoparticles also for embossed pictures ($z \neq 0$). Thanks to G.Lio for modeling the lady²⁴.* 112

Figure 7.1 *a), b) SEM images of SiO₂ NWs grown on Si substrate; in b) it is possible to distinguish the NWs with a homogenous distribution of diameters in the range of 30-300 nm; c) Profilometer measure of the thickness of the SiO₂ NWs layer on the Si substrate. Total thickness was estimated to be of 8 μm since there is a drift of 4 μm .* 114

Figure 7.2 *Objects were printed via TP-DLW with three different approaches: a) the first layer is printed at the interface with the Si for adhered structures to the substrate; b) the first layer is printed leaving a gap with the Si substrate ($z > 0$); in this case, the object can be detached after the etching of the SiO₂ between the resin and the Si substrate, which acts as a sacrificial layer; c) same case as a) but printing only the outer frame of the structure (shell); in this case, the SiO₂ NWs act as internal scaffold (shell & scaffold approach).* 115

Figure 7.3 *Optical microscope images of the different kinds of printed parallelepiped structures are shown: a) small (500 x 500 x 2.0 μm^3) and big (2000 x 2000 x 1.5 μm^3) parallelepipeds printed through the NWs layer and their magnifications are visible under reflected light. Different color underlines the solid and only shell structures: the printed objects appear brighter than the Si*

background. In the first magnification b) it is possible to notice the different height of the 3D objects printed at two different z-positions, adherent at the interface with the Si wafer (adhesive layer) and anchored to the SiO₂ NWs only. The polymer appears darker than the Si substrate and the SiO₂ NWs. It can be clearly appreciated that the object printed on the left is out of focus. This is the first evidence that the presence of a SiO₂ NWs layer permits printing at different heights as depicted in Figure 3a and Figure 3b. In c) and d) a closer look at one of the samples where it can be clearly observed that the SiO₂ NWs are well-embedded in the polymeric matrix. 116

Figure 7.4 *Profilometer measurements of an adhered structure at the SiO₂ NWs interface a) before and b) after 15 min immersed in HF buffer. A decrease in the roughness of the surface evidences the successful etching of the SiO₂ NWs* 118

Figure 7.5 *SEM micrographs of an adhered structure at the SiO₂ NWs interface after a), b) 15 min and c) 30 min immersed in HF buffer.....* 118

Figure 7.6 *a) SEM image of the cross-section of a FRPN showing the gap between the Si substrate and the sample printed with the IP-S resin; b) cartoon depicting a) for clearer interpretation.* 119

Figure 7.7 *Profilometer measurements of an adhered structure at the SiO₂ NWs interface following the shell & scaffold approach a) before and b) after 15 min immersed in HF buffer. The decrease in the surface roughness indicates the successful etching of the exposed SiO₂ NWs.....* 120

Figure 7.8 *a) Young's modulus (E_{IT}) and nano-hardness (H_{IT}) as a function of the indentation load; b) plot of the nano-indentation results for Young's modulus and nano-hardness vs indentation load. Maximum indentation depth (h_{max}) and residual depth (h_p) as a function of the indentation force.* 121

Figure 7.9 *Indentation load vs penetration depth curve for the FRPN fabricated in this work.* 122

Figure 7.10 *Optical images of lines, isolated points, text and woodpiles nanopatterns realized combining a SiO₂ NWs substrate with a gold precursor. It is possible to print through the nanowires carpet thanks to their refractive index, infact they result transparent to the wavelength of the NIR laser used in TP-DLW system.* 124

Tables

Table 4.1 <i>Different treatments done to the droplet and sandwich samples. The first treatment was made to cure of the resin precursor while the second treatment was made to reduce the gold precursor into AuNPs.</i>	39
Table 6.1 <i>Average values and standard deviation of the diameter of the gold nanoparticles after one, two and three hours.</i>	109
Table 7.1 <i>Comparison of Young's modulus and nano-hardness values for bare polymeric resin (IP-S) and the FRPN loaded with SiO₂ NWs printed via TP-DLW in this work.</i>	123
Table 8.1 <i>Summary of the work developed in this thesis, showing the different novel materials manufactured and the AM technologies used in each case.</i>	125